Modeling, Analysis, and Design of High-Frequency High-Density Low-profile Power Transformers

by

Ning Dai

Dissertation submitted to the faculty of the
Virginia Polytechnic Institute and State University
in partial fulfillment of the requirements for the degree of
Doctor of Philosophy
in Electrical Engineering

APPROVED:

Fred C. Lee, Chairman

Milan M. Jovanović

Dan Y. Chen

Ioannis Besieris

Douglas J. Nelson

1996

Blacksburg, Virginia

Modeling, Analysis, and Design of High-Frequency High-Density Low-Profile Power Transformers

by

Ning Dai

Fred C. Lee, Chairman

The Bradley Department of Electrical Engineering

ABSTRACT

This work presents modeling and analysis techniques for low-profile transformers in power electronics. Based on the modeling and analysis, the design methodologies and design tools are provided.

High frequency low-profile transformer 1-D winding loss, core loss and temperature rise models are derived in terms of the transformer geometry parameters. A 2-D FEA (Finite Element Analysis) is used to visualize the high frequency electromagnetic field and current density distribution, and to quantify high frequency power dissipation and energy storage in transformer by taking the skin effect, proximity effect, and edge effect into account. The characteristics of winding arrangements (interleaved or sandwiched, balanced or unbalanced) with different types of wire (solid wire, Litz wire, and printed wire) are accurately predicted.

An algorithm is developed to design a low-profile transformer that has a maximum power density and meets a given set of specifications. The maximum achievable power density for a given power level and output voltage is computed based on only one fundamental constraint: temperature rise. A nonlinear optimization programming tool is developed based on the algorithm. Consequently, the maximum achievable power density and the required number of turns are determined, along with the optimum operating frequency and core geometry.

Acknowledgements

I would like to express my deepest and most sincere gratitude for my advisor, Dr. Fred C. Lee for his support and guidance in this research. His vision, outlook and encouragement has lead to this type of research in new areas. I would also like to thank Dr. Dan Chen for his help and enthusiasm in applying his knowledge in this area. I must thank Dr. Douglas J. Nelson for many discussions and comments and notes that have set the foundations for this work. I am also grateful to Dr. Milan M. Jovanovic for conducting so many discussions about this topic. I would like to thank Dr. Ioannis Besieris for his help and suggestions. I must thank all the members of the excellent VPEC group, especially Dr. Ashraf W. Lotfi and Mr. Gleen Skutt with whom endless discussions have further enlighten my knowledge and opened the door to many issues and topics. Particularly, I would like to Dr. Pawel Gradzki, Dr. Guichao Hua, Dr. Votech Tebize, Mr. Wei Chen, Mr. Richard Zhang, Mr. Michael Zhang for endless exchanges of thoughts and experiences. Finally, this dissertation is dedicated to my parents. This work was supported by the Virginia Center for Innovative Technology, Delta Power Electronics, Lambda Electronics, Virginia Power Technologies.

Table of Contents

Chapter 1

Introduction

1.1 Background and Motivation

The advent of solid state electronics has prompted the miniaturization of virtually all electronic equipment. Switch-mode power supplies have also followed suit. An important component in this miniaturization is magnetic devices.

In some applications, the magnetic devices are required to possess not only small volumes but also low profiles. The height of magnetic components is restricted to a small value (0.4 in or less), because the power supply that contains the transformer and inductor has to fit into a thin slot, or because the power supply has to be directly mounted on a

function card, as is the case in aircraft and computer systems. Therefore, a high-frequency, high-density, low-profile transformer is required in response to these application and packaging requirements.

In transformers, the high-frequency eddy current effect (skin effect and proximity effect) that raises the copper loss and core loss complicates the design of compact transformers. Since the high-frequency phenomena involved in magnetic devices are quite complex both in the windings and in the core, it takes a lot of effort to model high frequency winding loss and develop an optimization procedure for standard transformers [A11, A12, ... , A26, B6, B7, ... , B14]. These models and optimization design tools have been widely used to design standard transformers.

However, as a new generation of transformers, low-profile transformers are quite different from standard transformers. A classical transformer is typically designed by using a standard ferrite core; magnet wire is used to implement the cylindrical winding layer, and the transformer is cooled by convective heat transfer. A low-profile transformer is typically packaged into a small "brick" type converter, where the entire circuit is encapsulated or sealed-off from the external environment. In such a case, the physical constraints on size make most standard cores impractical, and custom or altered cores must be used. The magnet wire or copper foil is used to implement spiral or planar winding layer [C2, C3, C4, C6, C7, C9, C13]. In addition, the low-profile transformer must be cooled by conduction to the case of the converter first, and then by convection

from the heat sink via natural or forced-air cooling. Therefore, the high-frequency model that predicts transformer eddy current loss and energy storage [A11, A12, A13, ..., A26] and transformer optimization tools [B6, B7, B8, B9, B10, B11, B12, B13, B14] that have been developed for standard transformers are often not suitable for low-profile transformers. **New models and design tools** are needed for high-frequency, high-density, low-profile transformers.

1.1.1 High-Frequency Winding Loss Modeling

The high-frequency model that predicts transformer eddy current loss and energy storage has been discussed in the literature over the last two decades [A11-A26]. Both skin and proximity effects determine the total field distribution, and hence the power loss and energy storage. These effects have been modeled by numerous researchers by converting the winding structure, whether it be wire or foil, into layers of continuous sheets of conducting material with modified conductivity to account for porous regions being filled with conductors, as shown in Fig. 1.1. In the equivalent-foil model of a transformer, where the magnetic field lines in the winding space are parallel to the center leg of the core, the solution for the magnetic field intensity inside a layer is a function of only one dimension, the radius, and this solution can be derived as if the cylindrical equivalent-foil winding layer shown in Fig. 1.2 extended endlessly in the z-direction. The power dissipation and energy storage are proportional to the dc-field intensity ratio and

maximum dc-field intensity. The one-dimensional method has become the most widely used analytical method for calculating high-frequency resistance and leakage inductance with acceptable accuracy [A11, A12, A13, A14, ..., A26]. The principal assumptions of all these methods are:

1. The magnetic field intensity is constant at each conductor layer (as shown in Fig. 1.3).

2. The current density is constant along the surface of each layer (as shown in Fig. 1.3).

3. Edge effects are completely ignored.

However, in a low-profile transformer, the magnetic field intensity is not a constant at each conductor layer, and the current density is not constant along the surface of each layer either. Both of them are functions of radius r, as shown in Fig. 1.4. It means that the field intensity at conductor surface is not a phasor. As a result, the high-frequency winding loss model that was developed for conventional transformers cannot be applied for low-profile transformers. So, no low-profile transformer winding loss model exists (even for the one-dimensional model). Thus a **new 1-D winding loss model** for low-profile winding loss calculation **needs to be derived**.

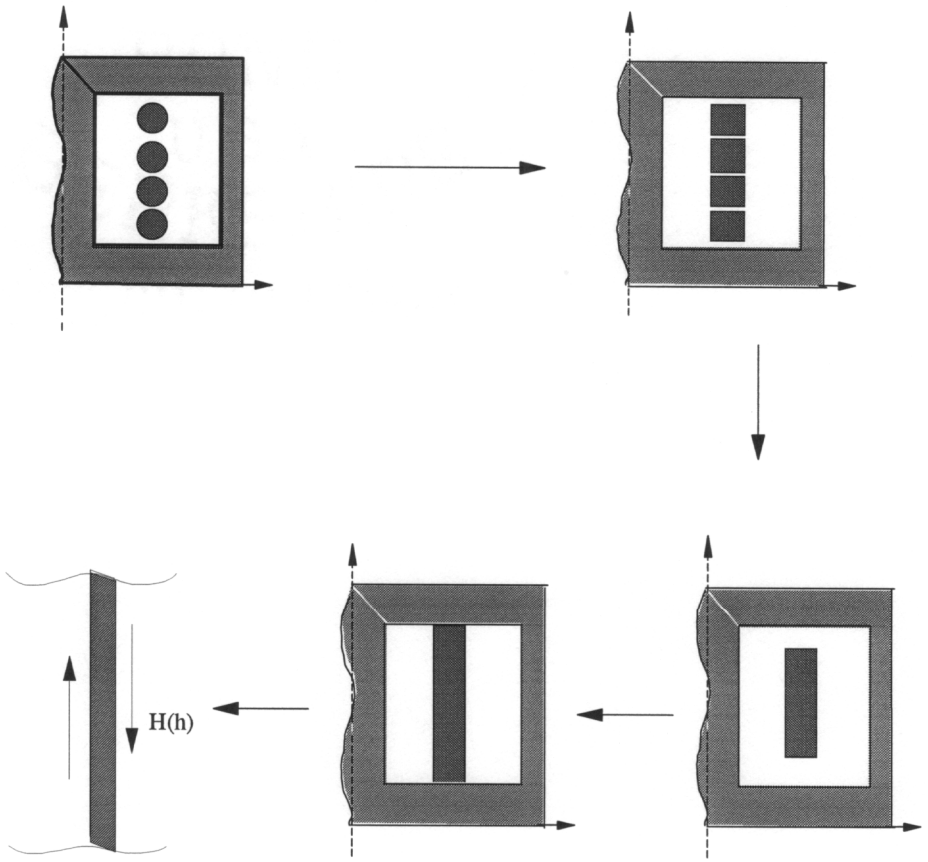

Fig. 1.1 Steps in transforming a layer of round wires into an equivalent-foil layer for 1-D analysis. The η is porosity factor used to account for the effective conductivity of the foil layer which is lower than the conductivity σ of the conductors.

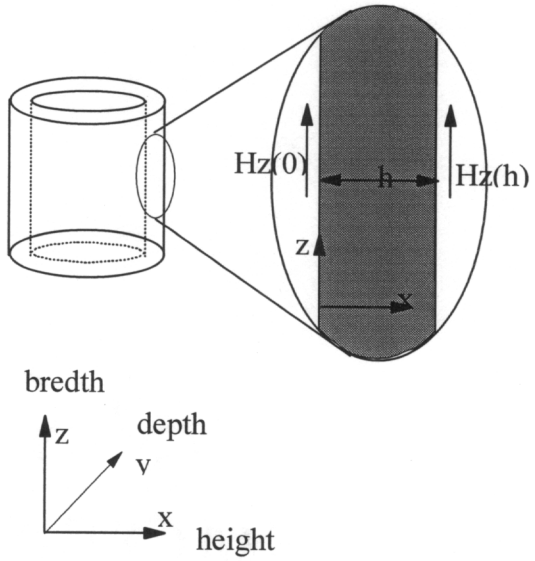

$$P_d = \frac{b_{win} \cdot l_T}{\sigma} \int_0^h \frac{k}{\sinh(kh)} \left[H_z(h)\cosh(kx) - H_z(0)\cosh(h-x) \right]^2 dx$$

$$= b_{win} \cdot l_T \cdot \frac{(H_z(h))^2}{\eta\sigma h} \left[(1+\alpha^2) \frac{\Delta(\sinh(2\Delta)+\sin(2\Delta))}{\cosh(2\Delta)-\cos(2\Delta)} - 4\alpha \frac{\Delta(\sinh\Delta\cos\Delta+\cosh\Delta\sin\Delta}{\cosh(2\Delta)-\cos(2\Delta)} \right]$$

$$\text{where } \alpha = \frac{Hz(h)}{Hz(0)}, \text{ and } k \approx \sqrt{j\omega\mu_o\eta\sigma}$$

Hz(0) and Hz(h) are phasors: magnitude changes with time.

Fig. 1.2 Equivalent-foil approximation of transformer winding layer. To obtain the field solution, this cylindrical structure is analyzed as an infinite conductor sheet. Hz(0) and Hz(h) are field intensities at the boundaries of the conductor. α is the ratio of magnetic field intensity at conductor surface. Pd represents power dissipation or energy storage in transformer winding layer. The power dissipation and energy storage are proportional to α and the magnitude of Hz(h).

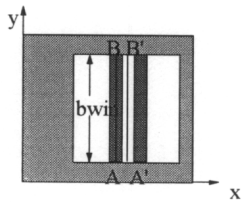

(a)

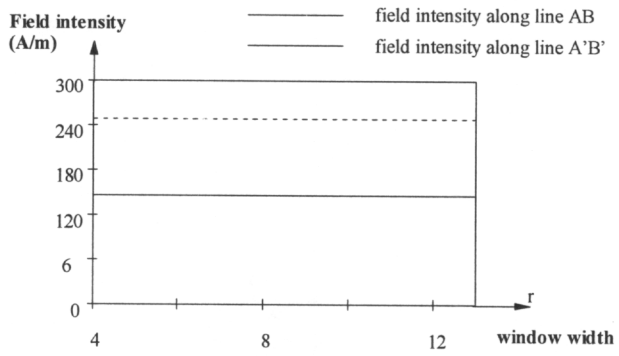

(b)

(c)

Fig. 1.3 (a) A two winding layer conventional transformer; (b) field intensity versus window height in a conventional transformer; (c) current density distribution in transformer winding layer. The field intensity is constant at each conductor layer. The equal current density lines are parallel to conductor surface.

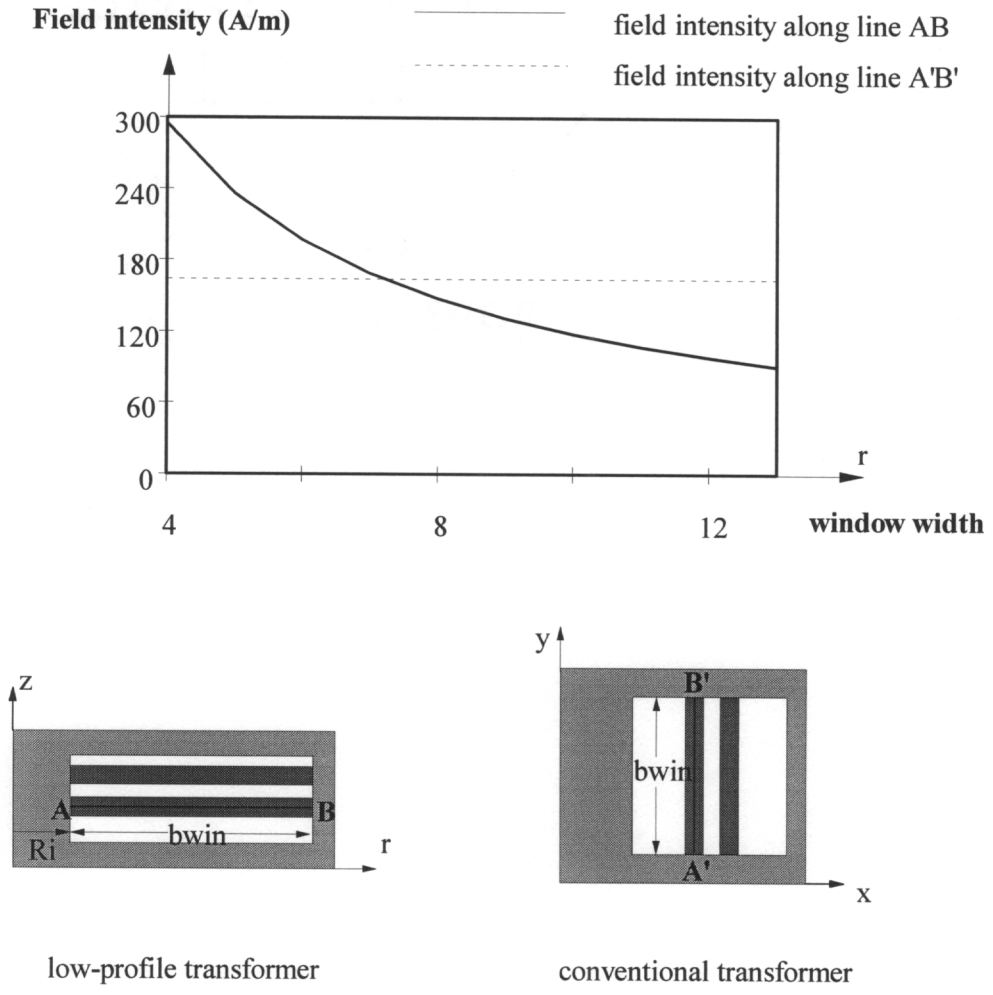

Fig. 1.4 Comparison of the field intensity in a low-profile transformer and a conventional transformer. In a conventional transformer, the field intensity is a constant at each conductor layer. In a low-profile transformer, the field intensity drops with window width.

In the one-dimensional winding loss model, any kind of wire will be transformed into an equivalent-foil type of conductor, and transformer power dissipation and energy storage are merely the functions of dc-field intensity ratio and maximum dc-field intensity. Therefore, the 1-D model cannot distinguish between different wire types: solid wire and printed-wire. And also, this model cannot reveal differences between the performances of different winding arrangements: interleaved (P-S-P-S) or sandwiched (P-S-S-P and S-P-P-S) winding structures. As shown in Fig. 1.5, the three winding arrangements will have the same magnetic field intensity at the conductor surfaces, and the same value of α. As a result, they have the same values of power dissipation and energy storage in the transformer, and hence the same ac-resistance and leakage inductance. However, a FEA technique displays totally different magnetic field and current distributions for these winding arrangements, and exhibits the different values of ac-resistance and leakage inductance. Figure 1.6 shows 1-D field distribution and 2-D field distribution of the P-S-P-S winding arrangement. The difference between them is obvious. Figure 1.7 shows the ac-resistance and leakage inductance of the three winding arrangements at different frequencies. Obviously, the one-dimensional method is not accurate enough to predict the high-frequency magnetic field and current distribution in transformers with different winding arrangements and wire types.

The newly developed method is of the two-dimensional type and accounts for skin effect, proximity effect, and edge effect in the transformer winding [A27]. However, it assumes that

1. Transformer core has an infinite permeability.

2. Conductors have rectangular cross sections.

3. Conductors are placed so that their edges are parallel to the ferrite boundaries.

4. Field intensities along the conductor edges are constant.

Because of the assumption of the constant field intensity along the conductor edges, this 2-D method cannot be extended to low-profile transformer winding loss calculation. Besides, this method cannot handle complex winding structures.

Because of the complexity of low-profile transformer geometry, it is difficult to develop an exact closed-form solution for calculating high-frequency power dissipation and energy storage. As a practical alternative, a numerical method can be used, which can handle different kinds of geometry and non-linearity problems [A6, A7, A8, A9, A10, A27, A28, A29, A30]. It gives a clear picture of regions of high leakage fields and strong current crowding, and this information is quite useful in designing the windings for minimal losses. By using the FEA, investigators have pointed out the additional winding loss due to air gap of the transformer and displayed the field and current distribution [A1,

Different Winding Arrangements Have the Same 1-D Solution

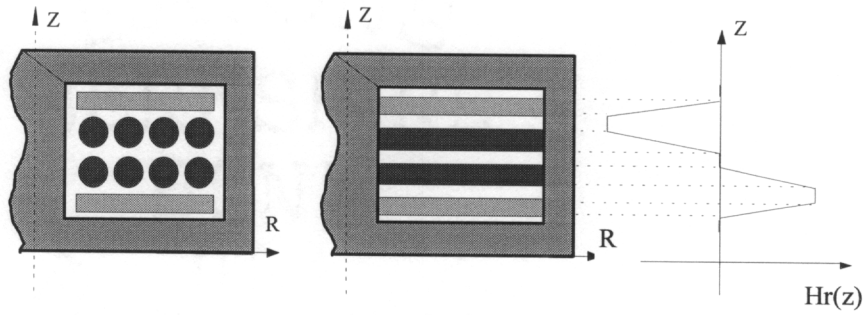

(a) S-P-P-S

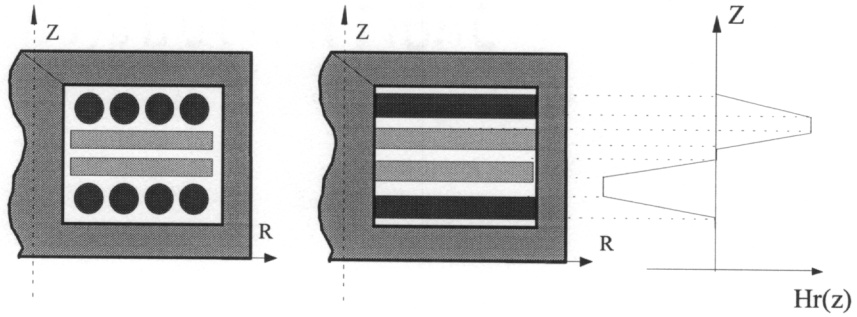

(b) P-S-S-P

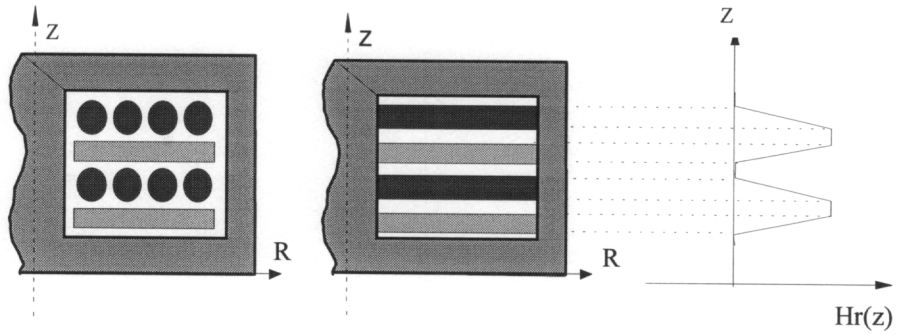

(c) S-P-S-P

Fig. 1.5 Illustration of 1-D method gives the same field intensity at conductor surfaces and the same value of α for the three different winding arrangements. "P" represents primary winding layer. "S" represents secondary winding layer.

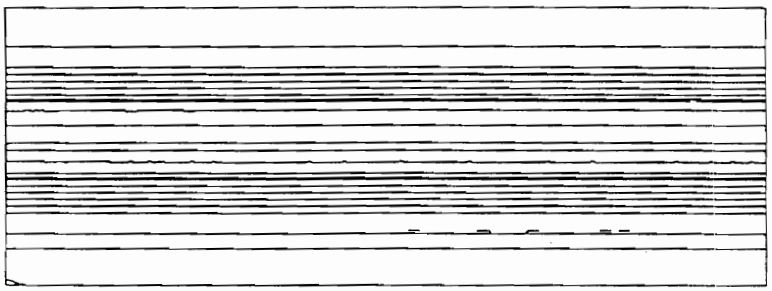

(a) 1-D field distribution.

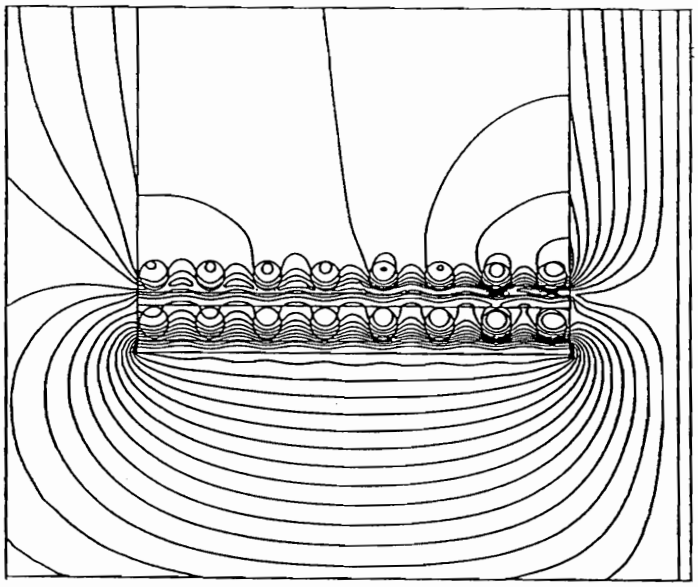

(b) 2-D field distribution.

Fig. 1.6 Field distributions with 1-D model and 2-D Finite Element analysis for winding arrangement of S-P-S-P.

Resistance of Transformer Windings at Different Frequencies Obtained by Using FEA and 1-D Method

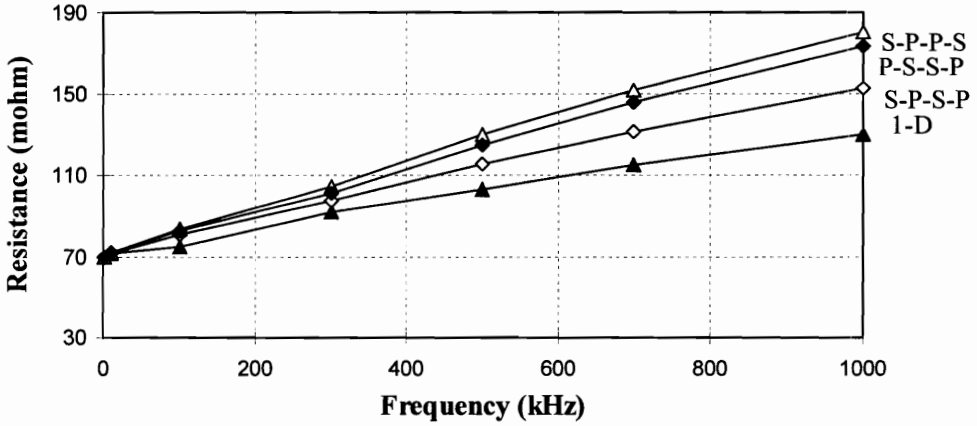

Leakage Inductance of Transformer at Different Frequencies Obtained by Using FEA and 1-D Method

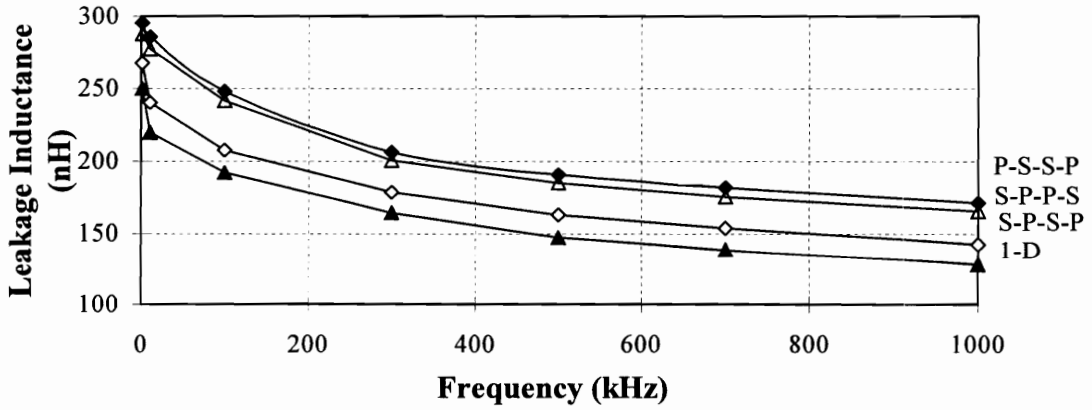

Fig. 1.7 The plot of ac-resistance and leakage inductance of S-P-P-S, P-S-S-P, and S-P-S-P winding arrangements with solid wire primary when frequency ranges from dc to 1 MHz. The 1-D method fails to show the differences among these three winding arrangements, and consequently predicts a lower resistance. The FEA method shows the different results.

A2]. W. M. Chen and A. Nysveen [A3, A6] investigated the fringe field in inductors, and compared the winding loss of the inductors with distributed air gap or with one lumped air gap. They pointed out the benefits of using the distributed air gap in inductors, that is, low fringe field and low eddy current loss. Odendal [A31] pointed out a way to combine numerical and analytical methods to predict the copper foil winding loss. In his paper, the one-dimensional method is used to predict eddy current loss at high frequency, and the FEA is used to calculate the additional loss caused by fringing field due to air gap. There are, however, **no clear picture** of high-frequency magnetic field and current distribution in low-profile transformers, and **no exact solution** specifying ac-resistance and leakage inductance for different winding arrangements and winding constructions.

1.1.2 Low-Profile Transformer Optimization

The issue of transformer optimization in power electronics was first addressed in 1980. Transformer weight or loss has been minimized by using a mathematical nonlinear program: the Augmented Lagrange Penalty Function Technique (ALAG) [B8, B9, B18, B19]. In these methods, the window aspect ratio and center-post aspect ratio (as shown in Fig. 1.8) are assumed to be constant. The assumption is true for transformers built with commercially available standard cores. However, low-profile transformer core is custom-designed according to certain design requirements. The aspect ratio changes from one core to another. Therefore, this method is difficult to extend to low-profile transformer

optimization. McLyman proposed to use area products to design transformers and pointed out the relations between the area product and the transformer volume for EE-core and pot-core transformers [B21]. This relation has been extensively used to optimize high-frequency transformers [B10, B11, B12, B13, B14, B16]. However, these methods are confined to standard transformers with commercially available cores.

For low-profile transformer design, A. Goldberg [B2] analyzed the relationship between footprint and copper loss in 1-10-MHz transformers. He pointed out that the copper loss is minimized in a planar spiral primary winding when the resistances of all turns are equal so that the outermost winding turns are wider than the innermost turns in order to compensate for the longer length of turn. However, it is expensive to make a transformer with such a winding pattern. K. Ngo [B1, B3] pointed out that height reduction may degrade transformer power density (assuming that efficiency is kept constant while the height is reduced). However, both authors use dc-resistance to predict the winding loss by limiting the winding thickness to the skin depth. Therefore, these design approaches are inadequate for a new generation of transformers.

In order to design a low-profile transformer that has a maximum power density and meets both the electrical and thermal specifications, and to clarify the trade-offs between the core loss and winding loss, and between the profile and footprint, a **new design tool** that can be used for low-profile transformer optimization needs to be found.

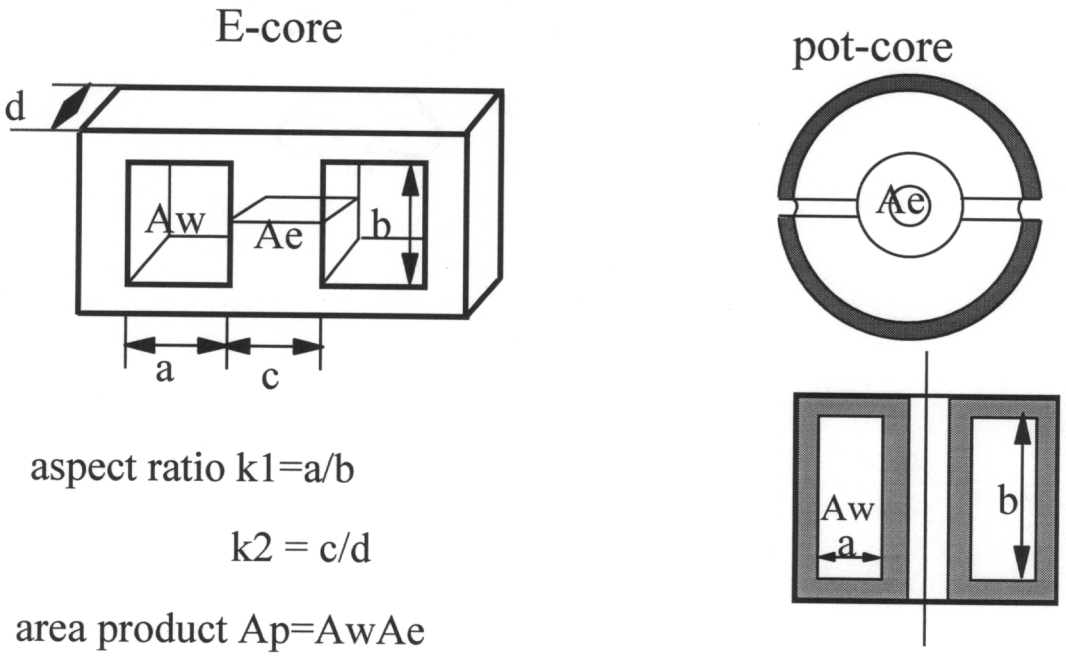

Fig. 1.8 Definition of aspect ratio and area product of E-core and pot-core. Window aspect ratio *k1* is defined as transformer core window width *a* over window height *b*, and center-post aspect ratio *k2* is defined as center-leg width *c* over center-leg thickness *d*. *Ap* represents area product. *Aw* is the window area of core. *Ae* is the cross sectional area of core.

1.2 Objectives

The objective of this work is to expose and resolve design issues pertaining to the high-frequency, high-density, low-profile transformer, and to provide design methodologies.

1.2.1 Loss Characterization of High Frequency Effects in Low-Profile Transformer Windings

To expose the high frequency electromagnetic field behavior in low-profile transformers, a simplified one-dimensional field analysis is used to derive equations for calculating the frequency dependent ac-resistance and leakage inductance based on the layout and dimensions of its windings. The core loss is considered to be piece-wise uniformly distributed in each section and calculated by using empirical method that is proportional to the flux density and operating frequency. A purely conductive thermal model is used for temperature rise calculation, since a low-profile transformer is usually placed directly on a heat sink in a compact low-profile dc-dc converter. These closed form expressions provide a quick way to estimate the transformer winding loss, core loss, and temperature rise.

The FEA is used to **visualize** high frequency magnetic field and current distribution, and to **quantify** high frequency power dissipation and energy storage by taking high-frequency skin effect, proximity effect, and edge effect into account. The regions of high leakage fields and strong current crowding are clearly displayed. **The characteristics of winding arrangements (interleaved or sandwiched, balanced or unbalanced) with different wire types (solid wire, Litz wire, and printed wire) are accurately predicted**. This analysis reveals the mechanism of optimizing the winding structure for minimal loss.

1.2.2 Design Optimization of High-Density, Low-Profile Transformers

A new algorithm has been developed to design a low-profile transformer that has a maximum power density and meets a given set of specifications. The maximum achievable power density for a given power level and output voltage is computed **based on only one fundamental constraint i.e. temperature rise**. Consequently, the maximum achievable power density and the required number of turns are determined along with the optimum operating frequency and core geometry. **The algorithm is realized by using a nonlinear optimization technique and is coded into a program.** It reveals the relations between the transformer power density and design parameters, trade-offs between the winding loss and core loss, and trade-offs between footprint and profile.

Two design procedures are involved in the optimization process. They are the general design and fine tuning. The outcome of the design procedure I will generate a family of curves where every point on the design curve represents a minimum volume design for a given transformer height and operating frequency. Based on these curves, it is very easy to identify the maximum achievable power density. In design procedure I, a one-dimensional method is used for winding loss analysis. As mentioned in Chapter 2, the one-dimensional method neglects the transformer edge effect and termination losses, and it has at least 10% error in transformer winding loss calculation. In order to obtain a more accurate design, procedure II (fine tuning) is applied. In this procedure, the FEA method is used to calculate winding loss for the transformer designed by procedure I. The correcting factor Kp (defined in 5.17) is found. In the optimization routine, the 1-D winding loss will be increased K_p times to compensate for the effect that has been ignored.

The proposed design procedures are implemented as MATLAB optimization program, and its applicability is illustrated through several examples. The calculation results are experimentally verified.

Chapter 2

One-Dimensional High-Frequency Low-Profile Transformer Winding Loss Model

In this chapter, low-profile transformer winding loss is derived. A simplified field analysis, one-dimensional analysis, is used to derive equations for calculating the frequency-dependent ac-resistance and leakage inductance based on the layout and dimensions of the transformer's windings. The predicted ac-resistances and leakage inductances are plotted versus frequency, along with short-circuit inductances and resistances, to illustrate the accuracy and the limitations of the calculations. Discrepancies

are accounted for the edge effect of transformer winding, lead inductances, winding capacitances, and magnetizing inductance neglected in the field analysis.

In order to calculate power dissipation in the transformer winding, the field distribution inside the winding space should be known. Then, both the resistive and inductive components of the leakage inductance can be calculated. To permit solving for this field distribution as if it were a one-dimensional problem, the edge effect in the transformer winding is neglected, and the magnetic field in the winding spacing is assumed to be parallel to the conductor surface.

Based on the work of several authors reviewed by Urling [A20], transformer winding loss at high frequencies is calculated by the layer-by-layer approach. Only sinusoidal-current excitation is analyzed, but, in practice, such sinusoidal results can be applied to nonsinusoidal waveforms through Fourier analysis, as was done by Venkatraman and Vandelac [A13, A16].

2.1 Low-Profile Magnetic Field Solution

To obtain a physical model with parallel field lines, the actual winding layers of a transformer are approximated, as shown in Fig. 2.1, by equivalent-foil windings which span the entire breadth b_{win} of the core window. To compensate for the increase in the

cross-sectional area of the conducting layer that occurs in the last step of the transformation, an effective conductivity $\eta\sigma_{cu}$ is used in the field equation. This effective conductivity is lower than the conductivity σ_{cu} of the conductors, usually copper, by a factor called the layer porosity η, defined as

$$\eta = \frac{N_c b_{cu}}{b_{win}}, \tag{2.1}$$

where N_c is the number of conductor cross sections in the winding layer, b_{cu} is the equivalent conductor width per turn, and b_{win} is the window width. For a layer of round wire with conductor diameter d_{cu}, the equivalent foil height is

$$h_{cu} = \frac{d_{cu}\cdot\sqrt{\pi}}{2} = 0.8862 \cdot d_{cu}. \tag{2.2}$$

In the equivalent foil model of a transformer, a low-frequency magnetic-field-intensity profile, a plot of Hr versus z, is illustrated in Fig. 2.2. The shape of the field intensity profile is produced when the instantaneous current density is uniform inside each winding layer, which occurs when the frequency of the exciting current is low enough, so that the skin depth δ, defined in (2.11), is much larger than the thickness h_{cu} of the conductors. At high frequencies, where the skin depth is not significantly larger than the thickness of the conducting layers in the equivalent foil winding model, the profiles of current density and magnetic field intensity inside each layer change shapes with excitation frequency. As shown in Fig. 2.3, in each of the spaces between conducting

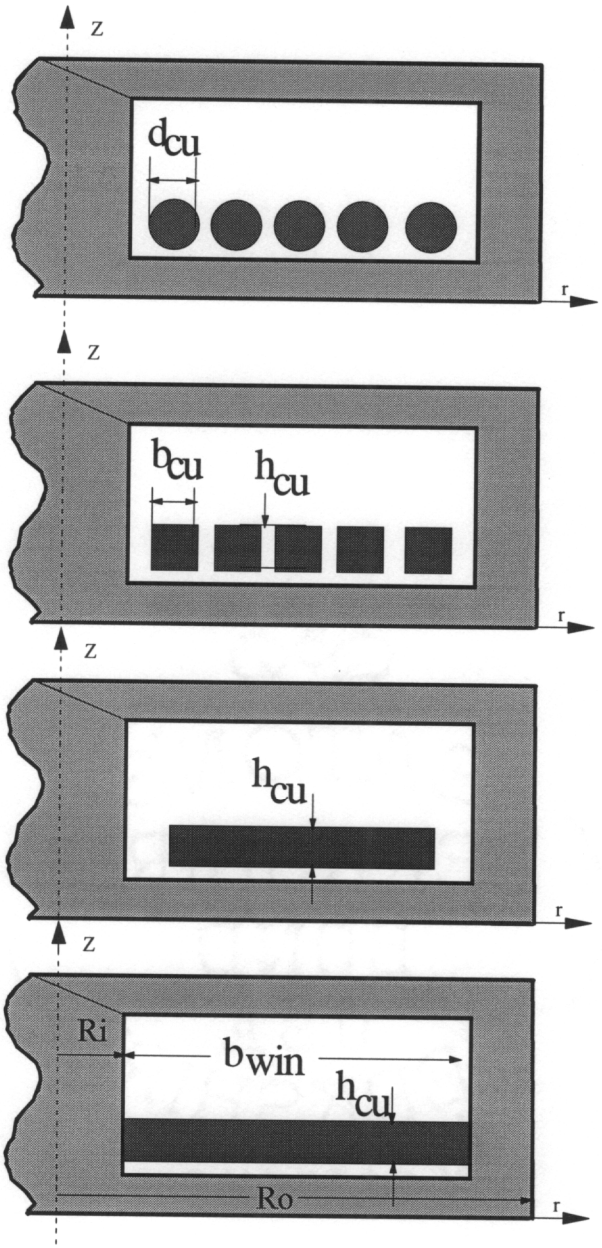

Fig. 2.1 Steps in transforming a layer of round wires into an equivalent foil layer for analysis. (a) round wires are replaced by square conductors with the same cross-sectional area of copper; (b) the squares are brought together to form a single foil layer; (c) then the foil layer is "stretched" in the R-direction to fill the entire window breadth W_w, without changing the height h_{cu} of layer or its position in the z direction.

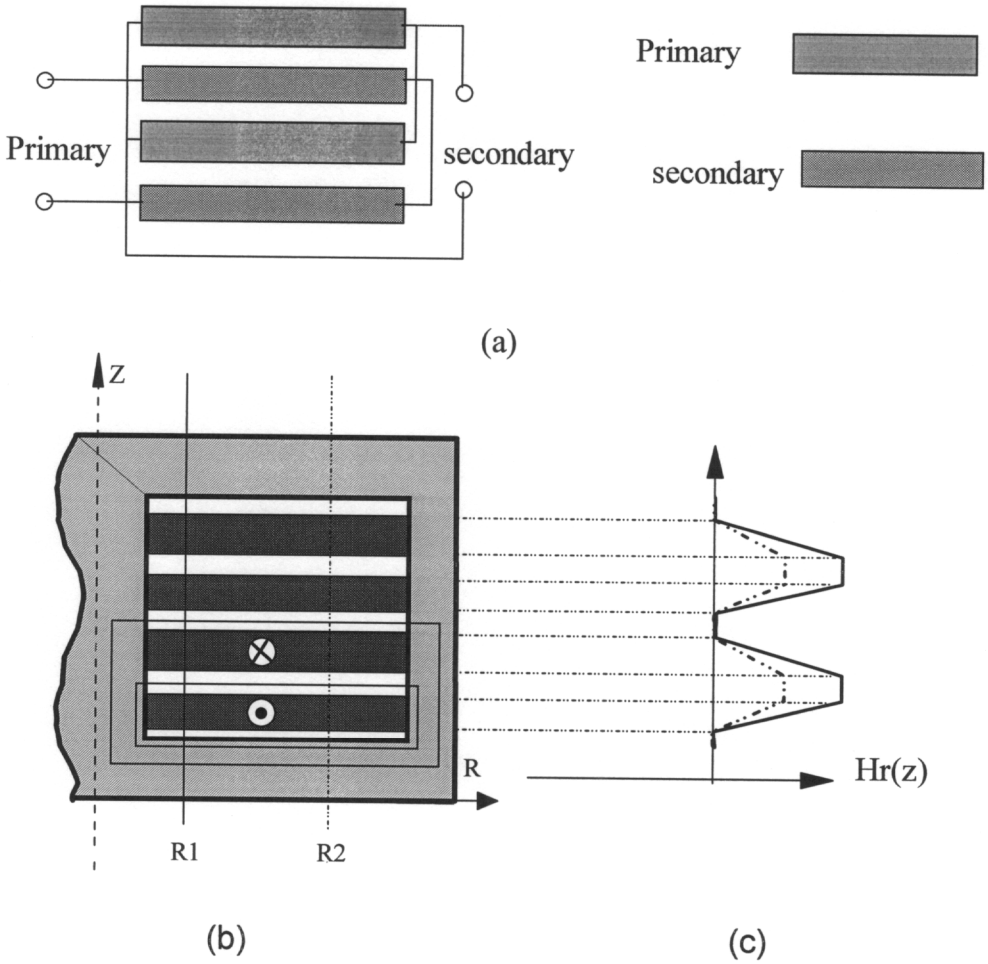

Fig. 2.2 (a) winding arrangement; (b) cross-sectional view of the right half of a transformer, showing the instantaneous current directions in the equivalent foil layers during one half-cycle of excitation. Ampere's law is applied to integration paths such as the two loops shown, to obtain (c) the instantaneous low frequency magnetic field intensity profile corresponding to the current directions in (b). The magnitude of this profile varies sinusoidally with time, but its relative proportions do not change.

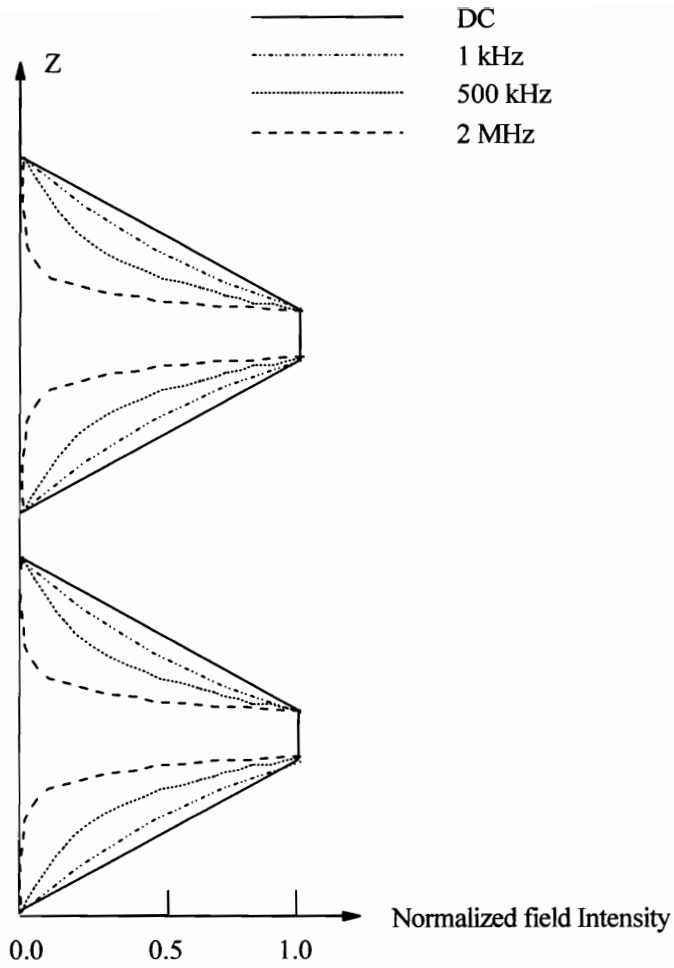

Fig. 2.3 Profiles of magnetic field intensity at different frequencies for the winding arrangement shown in Fig. 2.2. Although the magnetic field intensity inside the conducting layer changes with frequency, it keeps constant at conducting layer surface.

layers, however, the instantaneous field intensity depends only on 1) the turns in the individual winding layers of the transformer and 2) the net instantaneous current flowing at the terminals of the transformer, not on the frequency-dependent distribution of current in the conducting layers. Although the magnetic field intensity inside the conducting layer changes with frequency, it keeps constant at conducting layer surface. Therefore, for net winding currents that are sinusoidal and of constant amplitude, the low frequency magnetic field intensity profile can be used to obtain the frequency-independent boundary conditions needed to calculate the frequency-dependent profiles of magnetic field intensity and current density inside the conducting layers.

To obtain an expression for the field intensities in the interlayer spaces, the integral form of Ampere's law is applied to loops such as those shown in Fig. 2.2 (b). Phasor $\bar{H}_r^n$ of the r-directed magnetic field intensity in n^{th} interlayer space, is given by

$$\bar{H}_r^n = \frac{\sum_{p=1}^{n} N_c I_c}{\ln\left(\frac{R_o}{R_i}\right)} \frac{1}{r} = \frac{\sum_{p=1}^{n} N_c I_c}{\ln\left(1+\frac{b_{win}}{R_i}\right)} \frac{1}{r}, \qquad (2.3)$$

where the reluctance of the magnetic material has been neglected, and symbol *Nc* is chosen to represent the number of turns in the p^{th} layer, while *Ic* represents the net sinusoidal current flowing in each turn of the p^{th} layer (as shown in Fig. 2.4).

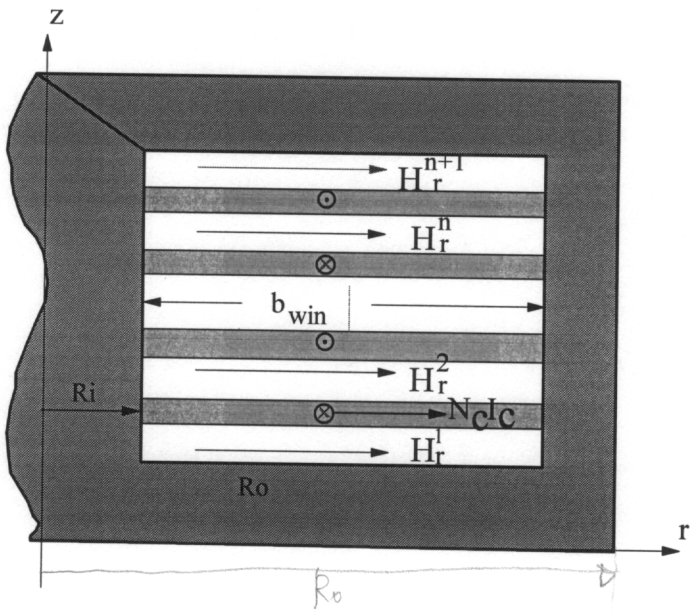

Fig. 2.4 Equivalent foil winding layer for field intensity analysis.

An equation that describes the magnetic field intensity distribution is derived from Maxwell's equations. The starting point is the differential form of Ampere's law,

$$\nabla \times \hat{H} = \hat{J} + \frac{\partial \hat{D}}{\partial t}, \tag{2.4}$$

where $\hat{H}$ is the magnetic field intensity, $\hat{J}$ is the current density, and $\hat{D}$ is the electrical flux density. In this dissertation, the symbol "^" on the top of a variable represents a vector. A vector is a function of space and time.

Taking the curl of (2.4), and substituting the vector identity $\nabla \times \nabla \times \hat{H} = \nabla(\nabla \bullet \hat{H}) - \nabla^2 \hat{H}$, we can obtain the equation

$$\nabla(\nabla \bullet \hat{H}) - \nabla^2 \hat{H} = \nabla \times \hat{J} + \frac{\partial(\nabla \times \hat{D})}{\partial t}. \tag{2.5}$$

Then the constitutive relations $\hat{B} = \mu \hat{H}$, $\hat{J} = \eta \sigma_{cu} \hat{E}$, and $\hat{D} = \varepsilon \hat{E}$; Gauss's law for magnetism, $\nabla \cdot \hat{B} = 0$; and Faraday's law, $\nabla \times \hat{E} = -\frac{\partial \hat{B}}{\partial t}$, are applied to obtain the result

$$\nabla^2 \hat{H} = \mu \eta \sigma_{cu} \frac{\partial \hat{H}}{\partial t} + \mu \varepsilon \frac{\partial^2 \hat{H}}{\partial t^2}. \tag{2.6}$$

If the magnetic field $\hat{H}$ is varying sinusoidally in time, it can be represented by a vector phasor $\vec{H}$, where the symbol "_" on the top of a variable represents a phasor, and the magnitude $|\vec{H}|$ of the vector phasor is chosen to be the rms value of the field intensity.

$$H(x,y,z,t) = \sqrt{2}\,\mathrm{Re}\left[\underline{H}(x,y,z)e^{jwt}\right]. \tag{2.7}$$

Substituting (2.7) into (2.6), and noticing that differentiating a sinusoidally-varying vector with respect to time is equivalent to multiplying its vector phasor by $j\omega$ leads to obtaining the three-dimensional diffusion equation, which contains the complex wave number k:

$$\nabla^2\bar{H} = k^2\bar{H}, \tag{2.8}$$

$$k = \sqrt{j\omega\mu\eta\sigma_{cu} - \omega^2\mu\varepsilon}\,. \tag{2.9}$$

In a copper conductor, where $\sigma_{cu} = 5.8\times10^7$ S / m at 25 ^{0}C, $\mu_o = 4\pi\times10^{-7}$ H / m, and $\varepsilon_0 = 8.85\times10^{-12}$ F / m, the k is

$$\underline{k} \approx \sqrt{j\omega\mu_0\sigma_{cu}} = \sqrt{\frac{\omega\mu_o\sigma_{cu}\eta}{2}}(1+j) = \frac{1}{\delta}(1+j). \tag{2.10}$$

This approximation is valid for all frequencies less than 10^{12} hertz, above which the conductivity of copper becomes frequency dependent. The complex wave number k is seen to be closely related to the skin depth δ, defined as

$$\delta = \sqrt{\frac{2}{\omega\mu_o\eta\sigma_{cu}}}\,. \tag{2.11}$$

The resultant vector phasor $\bar{H}$ represents the sum of three orthogonal vector phasors, one for each spatial component of vector $\hat{H}$:

$$\vec{H}(r,\theta,z) = \vec{H}_r\hat{a}_r + \vec{H}_\theta\hat{a}_\theta + \vec{H}_z\hat{a}_z . \qquad (2.12)$$

For the infinite conducting sheet problems illustrated in Fig. 2.5, the magnetic field intensity vector phasor $\vec{H}(r,\theta,z)$ has only an r-component, which is a function of only z. Thus, the three-dimensional diffusion equation becomes the one-dimensional diffusion equation:

$$\frac{\partial^2 H_r(z)}{\partial z^2} = k^2 H_r(z). \qquad (2.13)$$

The general solution of (2.13) has the form of

$$H_r(z) = \underline{H}_1 e^{kz} + \underline{H}_2 e^{-kz}, \qquad (2.14)$$

where $\vec{H}_1$ and $\vec{H}_2$ are phasors determined by applying the boundary conditions of magnetic field intensity at the surface of the conducting sheet, $\vec{H}_r(0)$ and $\vec{H}_r(h_{cu})$ in Fig. 2.3. The resulting expressions for $\vec{H}_1$ and $\vec{H}_2$ are substituted into (2.14), and the definition of $\sinh(x) = \frac{e^x - e^{-x}}{2}$ is applied, to give

$$H_r(z) = \frac{1}{\sinh(kh_{cu})}\left[\vec{H}_r(z = h_{cu})\sinh(kz) + \vec{H}_r(z = 0)\sinh(k(h_{cu} - z))\right]. \qquad (2.15)$$

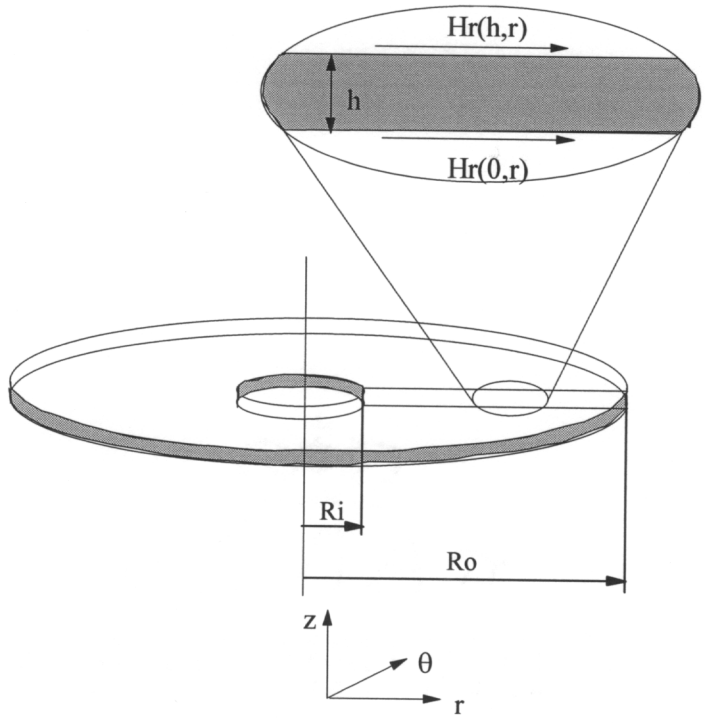

Fig. 2.5 Equivalent foil approximation of a transformer winding layer. To obtain the field solution, the winding layer is analyzed as an infinite conducting sheet with a similar cross section, but extending to infinity in the r-direction.

For the convenience later in the derivation, the boundary condition ratio is defined as

$$\alpha + j\beta = \frac{\bar{H}_r(\chi = 0)}{\bar{H}_r(\chi = h_{cu})}. \tag{2.16}$$

To prevent a zero appearing in the denominator when only one boundary condition is zero, and to bound $|\alpha + j\beta|$ to the interval [0,1], a new variable χ (chi) is used to indicate position along the z-axis in Fig. 2.3. The following definition places $\chi = 0$ at the surface which has the smaller of the two boundary magnetic fields, and $\chi = h_{cu}$ at the surface with the larger field.

$$\begin{aligned} &\chi = z, && \text{if} \quad |\bar{H}_r(z = h_{cu})| \geq |\bar{H}_r(z = 0)| \\ &\chi = h_{cu} - z, && \text{if} \quad |\bar{H}_r(z = h_{cu})| \geq |\bar{H}_r(z = 0)|. \end{aligned} \tag{2.17}$$

An alternate form of (2.17) can then be written in terms of χ and boundary condition ratio $(\alpha + j\beta)$,

$$H_r(\chi) = \frac{\sum_{p=1}^{n} N_{tp} I_{tp}}{\sinh(kh_{cu}) \cdot \ln(1 + \frac{b_{win}}{R_i})} \cdot \frac{1}{r}\left[\sinh(k\chi) + (\alpha + j\beta)\sinh(k(h_{cu} - \chi)\right]. \tag{2.18}$$

If both boundary conditions of magnetic field intensity are equal to zero, (2.18) is undefined; but it is clear from (2.18) that the magnetic field intensity is zero everywhere

inside the conducting sheet. This implies that no magnetic energy is stored in the conducting sheet, and equations derived later will show that there is no power dissipation in it either.

Figure 2.6 shows the plot of magnetic field intensity in the transformer winding. It demonstrates that the field intensity along the conductor surface in a low-profile transformer drops as the window width increases, whereas the field intensity is constant along the conductor surface in a conventional transformer.

2.2 Power Dissipation and AC-Resistance of Low-Profile Winding

From the field solution given by (2.18) for the spatial variation of the magnetic field intensity phasor Hr(z) in an infinite conducting sheet, a similar expression can be derived for the corresponding current density phasor $J_\theta(z)$. Applying the constitutive relations $\hat{J} = \eta\alpha\hat{E}$ and $\hat{D} = \varepsilon\hat{E}$ to (2.4), converting to vector phasor for sinusoidal steady-state, and making the good-conductor approximation as in (2.11) yields the equation

$$\nabla \times \vec{H} = \eta\sigma_{cu}\vec{E} + j\omega\varepsilon\vec{E} \approx \eta\sigma_{cu}\vec{E} = \vec{J}. \qquad (2.19)$$

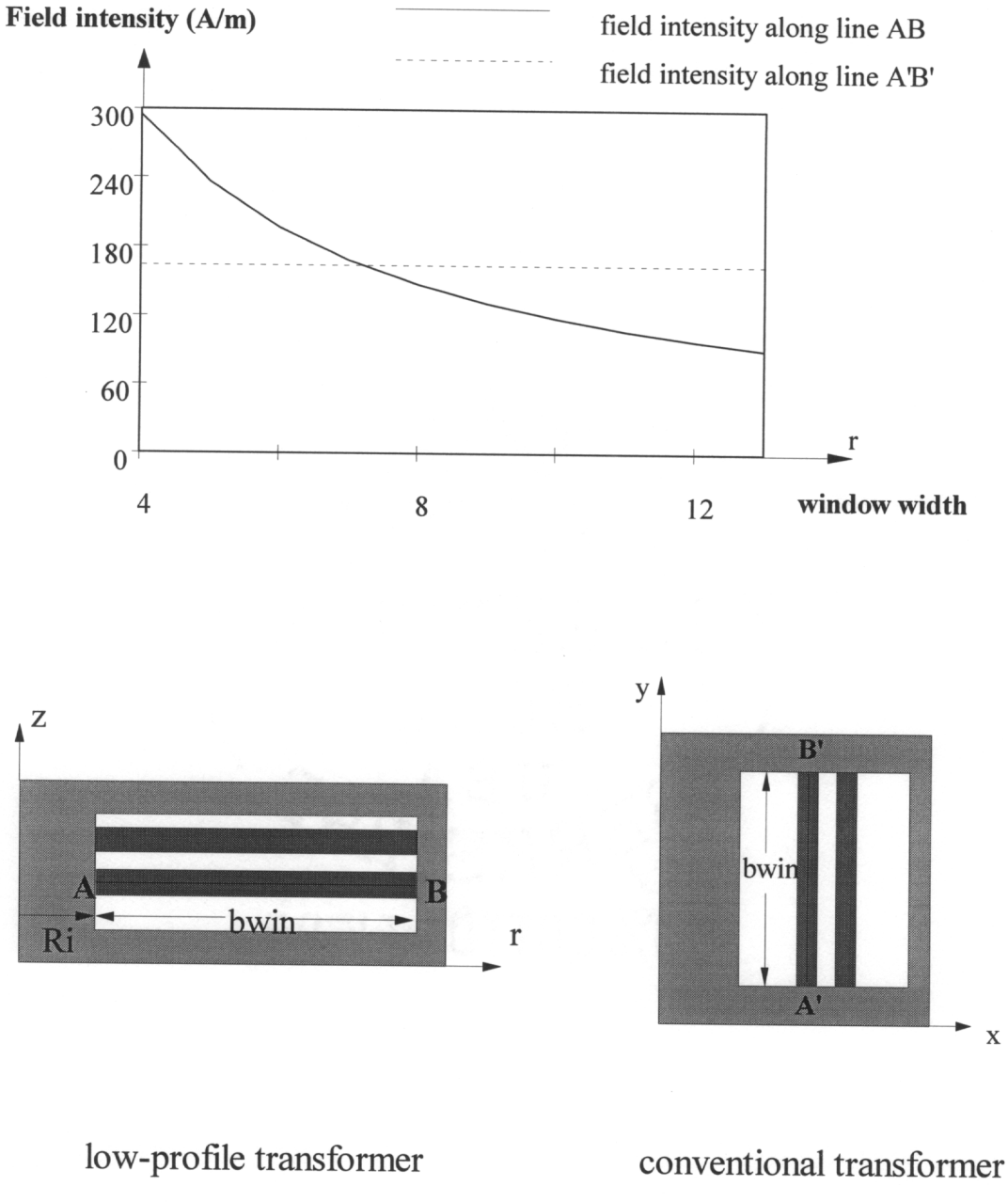

Fig. 2.6 Comparison of the field intensity in a low-profile transformer and a conventional transformer.

For the condition illustrated in Fig. 2.4, where $\vec{J}$ is θ-directed, $\vec{H}$ is r-directed, and both are functions of only z, the following equation is obtained from (2.19) by expanding the curl of H in cylindrical coordinates and eliminating all the terms that are equal to zero. Therefore,

$$J_\theta(z) = \frac{-\partial \vec{H}_r(z)}{\partial z}. \tag{2.20}$$

Substituting (2.15) into (2.20) and taking the partial derivative gives

$$\begin{aligned} J_\theta(z) &= \frac{-k}{\sinh(kh_{cu})}\left[\vec{H}_r(z = h_{cu})\cosh(kz) - \vec{H}_r(z = 0)\cosh(k(h_{cu} - z))\right] \\ &= \frac{-k \cdot \vec{H}_r(\chi = h_{cu})}{\sinh(kh_{cu})}\left[\cosh(k\chi) - (\alpha + j\beta)\cosh(k(h_{cu} - \chi))\right] \\ &= \frac{-k \cdot \sum_{p=1}^{n} N_{tp} I_{tp}}{\sinh(kh_{cu}) \cdot \ln(1 + \frac{b_{win}}{R_i})} \cdot \frac{1}{r}\left[\cosh(k\chi) - (\alpha + j\beta)\cosh(k(h_{cu} - \chi))\right]. \end{aligned} \tag{2.21}$$

The fundamental equation for the power dissipated per unit volume at a point in space is

$$p_d(t) = \frac{|J(t)|^2}{\sigma}. \tag{2.22}$$

The time-averaged power dissipation in any layer of the transformer windings is obtained by integrating this expression over both the time for one cycle of excitation and

the volume occupied by the layer. The integral over the excitation period T gives $\langle p_d \rangle$, the time average magnetic energy density at a point. The angle brackets denote a time average.

$$\langle p_d \rangle = \frac{1}{\sigma T} \int_T \left[\sqrt{2} \left| \bar{J}_\theta \right| \cos(\omega t) \right]^2 dt = \frac{1}{\sigma} \left| \bar{J}_\theta \right|^2 . \tag{2.23}$$

The quantity $\left| \bar{J}_\theta \right|^2$ is obtained as the product of the phasor $\bar{J}_\theta$, given by (2.21), and its complex conjugate $\bar{J}_\theta{}^*$.

$$\langle p_d \rangle = \frac{1}{\sigma} \bar{J}_\theta(\chi) \bar{J}_\theta{}^*(\chi) . \tag{2.24}$$

Integrating (2.24) over the volume occupied by an equivalent foil layer gives the time-averaged energy $\langle P_d \rangle$ stored in the magnetic field inside the layer. Considering the layer shown in Fig. 2.4 to be a piece of an infinite conducting sheet, this volume integral is

$$\langle P_d \rangle = \int_{R_i}^{R_o} \int_0^{2\theta} \int_0^{h_{cu}} \langle p_d \rangle \, r dr d\theta dz$$

$$= \int_0^{2\theta} d\theta \cdot \int_{R_i}^{R_o} \left[\frac{\sum_{p=1} N_{tp} I_{tp}}{\ln\left(\frac{R_o}{R_i}\right)} \right]^2 \frac{1}{r^2} dr$$

$$\cdot \int_{o}^{h_{cu}} \frac{1}{\eta\sigma}\left[\frac{-k}{\sinh(kh_{cu})}\left[\cosh(k\chi)-(\alpha+j\beta)\cosh(k(h_{cu}-\chi))\right]\right]^2 d\chi$$

$$= 2\pi \cdot \frac{\left(\sum_{p=1}^{n} N_{tp} I_{tp}\right)^2}{\eta\sigma h_{cu} \cdot \ln(\frac{R_o}{R_i})}\left[(1+\alpha^2+\beta^2)G_1(\Delta)-4\alpha G_2(\Delta)\right]$$

$$= \frac{l_T}{(R_i+\frac{b_{win}}{2})\cdot \ln(1+\frac{b_{win}}{R_i})} \cdot \langle Q_i \rangle ,$$

(2.25)

where

$$\langle Q_i \rangle = \frac{\left(\sum_{p=1}^{n} N_{tp} I_{tp}\right)^2}{\eta\sigma h_{cu}}\left[(1+\alpha^2+\beta^2)G_1(\Delta)-4\alpha G_2(\Delta)\right],$$

$$G_1(\Delta) = \Delta \frac{\sinh(2\Delta)+\sin(2\Delta)}{\cosh(2\Delta)-\cos(2\Delta)},$$

$$G_2(\Delta) = \Delta \frac{\sinh\Delta\cdot\cos\Delta+\cosh\Delta\cdot\sin\Delta}{\cosh(2\Delta)-\cos(2\Delta)}.$$

The variable *bwin* is the winding width, l_T is the length-of-turn, and the variable Δ is defined as h_{cu}/δ, the height of the winding layer normalized to skin depth.

The total power dissipation for all *N* winding layers is

$$P_D = \sum_{n=1}^{N} \frac{l_{T_n}\left(\sum_{p=1}^{n} N_{tp} I_{tp}(\chi = h_{cu})\right)^2}{\eta_n \sigma h_{cu_n}(R_i + \frac{b_{win}}{2}) \cdot \ln(1 + \frac{b_{win}}{R_i})}\left[(1+\alpha_n{}^2 + \beta_n{}^2)G_1(\Delta_n) - 4\alpha_n G_2(\Delta_n)\right]$$

$$= \sum_{n=1}^{N} \frac{l_{T_n}}{(R_i + \frac{b_{win}}{2}) \cdot \ln(1 + \frac{b_{win}}{R_i})} \cdot \langle Q_n \rangle \cdot$$

(2.26)

The basic relationship between the ac-resistance and the total time-averaged power $\langle P_D \rangle$ dissipated in the windings is

$$R_{ac} = \frac{P_D}{I_p{}^2} = \frac{\sum_{n=1}^{N} \frac{l_{T_n}}{(R_i + \frac{b_{win}}{2}) \cdot \ln(1 + \frac{b_{win}}{R_i})} \cdot \langle Q_n \rangle}{I_p{}^2}, \qquad (2.27)$$

where *Ip* is the rms current in transformer windings.

Figure 2.7 compares the ac-resistance of a low-profile transformer with that of an equivalent conventional transformer with the same conductor thickness and winding width. When the winding width is small, the conventional transformer has a higher ac-resistance than that of a low-profile transformer, because of a more uniform current distribution in the low-profile transformer. However, when the winding width increases to a certain value, the low-profile transformer has a higher ac resistance than that of the

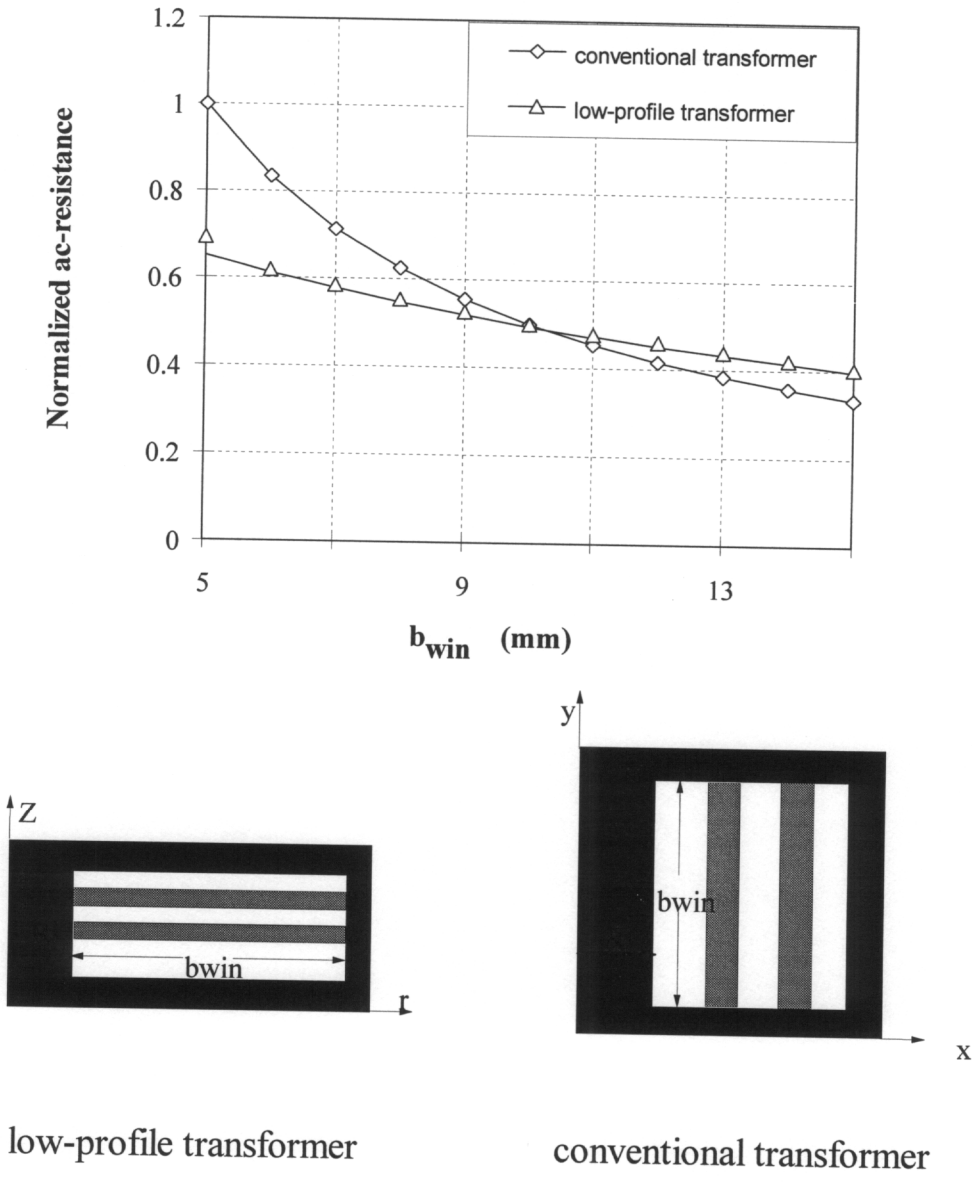

Fig. 2.7 Comparison of the ac-resistance of the low-profile transformer and the conventional transformer. The low-profile transformer and the conventional transformer have the same winding thickness and window width.

conventional transformer. Because the current takes the shortest path in a low-profile winding, the increase of the winding width doesn't help to reduce low-profile winding resistance.

2.3 *Leakage Inductance Calculation for Low-Profile Transformer*

The magnetic energy stored in any winding layer of a transformer can now be derived from the magnetic field intensity inside an infinite conducting sheet, given by (2.18). In general, the instantaneous energy $w_c(t)$ stored in a magnetic field per unit volume at a point in space is

$$w_c(t) = \frac{\mu}{2}\left|\hat{H}(t)\right|^2 . \tag{2.28}$$

The time-averaged energy stored in the magnetic field in any layer of the transformer windings is obtained by integrating this expression over both the time for one cycle of excitation and the volume occupied by the layer. The time-averaged magnetic energy density at a point is

$$\langle w_c \rangle = \frac{1}{T}\int_T \frac{\mu_o}{2}\left[\sqrt{2}\left|\bar{H}_r\right|\cos(\omega t)\right]^2 dt = \frac{\mu_o}{2}\left|\bar{H}_r\right|^2 = \frac{\mu_o}{2}\bar{H}_r(\chi)\bar{H}_r^{*}(\chi). \tag{2.29}$$

Integrating (2.29) over the volume occupied by an equivalent foil layer gives the time-averaged energy $\langle W_c \rangle$ stored in the magnetic field inside the layer. The volume integral is

$$\langle W_c \rangle = \int_{R_i}^{R_o} \int_0^{2\pi} \int_0^{h_{cu}} \langle w_m \rangle \, r dr d\theta dz$$

$$= 2\pi \cdot \frac{\mu_o h_{cu} \left(\sum_{p=1}^{n} N_{tp} I_{tp} (\chi = h_{cu}) \right)^2}{4 \cdot \ln(\frac{R_o}{R_i})} \left[(1 + \alpha^2 + \beta^2) G_3(\Delta) - 4\alpha G_4(\Delta) \right]$$

$$= \frac{l_T}{(R_i + \frac{b_{win}}{2}) \cdot \ln(1 + \frac{b_{win}}{R_i})} \cdot \langle Q_H \rangle ,$$

(2.30)

where

$$\langle Q_H \rangle = \frac{\mu_o h_{cu} \left(\sum_{p=1}^{n} N_{tp} I_{tp} (\chi = h_{cu}) \right)^2}{4} \left[(1 + \alpha^2 + \beta^2) G_3(\Delta) - 4\alpha G_4(\Delta) \right],$$

$$G_3(\Delta) = \frac{\sinh(2\Delta) - \sin(2\Delta)}{\Delta(\cosh(2\Delta) - \cos(2\Delta))},$$

$$G_4(\Delta) = \frac{\sinh\Delta \cdot \cos\Delta - \cosh\Delta \cdot \sin\Delta}{\Delta(\cosh(2\Delta) - \cos(2\Delta))}.$$

Therefore, for all N winding layers, the time-averaged energy $\langle W_{CN} \rangle$ stored in the winding layers is calculated by summing the results of (2.30):

$$\langle W_{CN} \rangle = \sum_{n=1}^{N} \frac{l_{T_n}}{(R_i + \frac{b_{win}}{2}) \cdot \ln(1 + \frac{b_{win}}{R_i})} \cdot \langle Q_H \rangle_n \quad . \tag{2.31}$$

The time-averaged magnetic energy $\langle W_s \rangle$ stored in an interlayer space is the volume of space times the energy density given by (2.29), where $\bar{H}_r$ in the interlayer space is obtained from (2.3). If h_{s_n} is the thickness of the n^{th} interlayer space, and $\langle W_{SN} \rangle$ is the sum of the energies for all (N-1) interlayer spaces, then

$$\langle W_{SN} \rangle = \sum_{n=1}^{N-1} \frac{l_{T_n} h_{Sn}}{(R_i + \frac{b_{win}}{2}) \cdot \ln(1 + \frac{b_{win}}{R_i})} \left[\frac{\mu_o}{2} \left(\sum_{p=1}^{n} N_{tp} I_{tp} \right)^2 \right]. \tag{2.32}$$

The total time-averaged energy $\langle W_T \rangle$ stored in the winding space of the transformer has two components, the time average energy $\langle W_{CN} \rangle$ stored in the winding layers, and the time-averaged energy $\langle W_{SN} \rangle$ stored in the interlayer spaces.

$$\langle W_T \rangle = \langle W_{CN} \rangle + \langle W_{SN} \rangle . \tag{2.33}$$

The leakage inductance L_{lk} is computed from the total time-averaged energy $\langle W_T \rangle$ stored in the winding space of the transformer,

$$L_{lk} = \frac{2\langle W_T \rangle}{I_p^2}. \tag{2.34}$$

Figure 2.8 compares the leakage inductance of a low-profile transformer with that of an equivalent conventional transformer with the same conductor thickness and winding width. The conventional transformer has a higher leakage inductance than that of the low-profile transformer, because of the higher field intensity in the transformer window area.

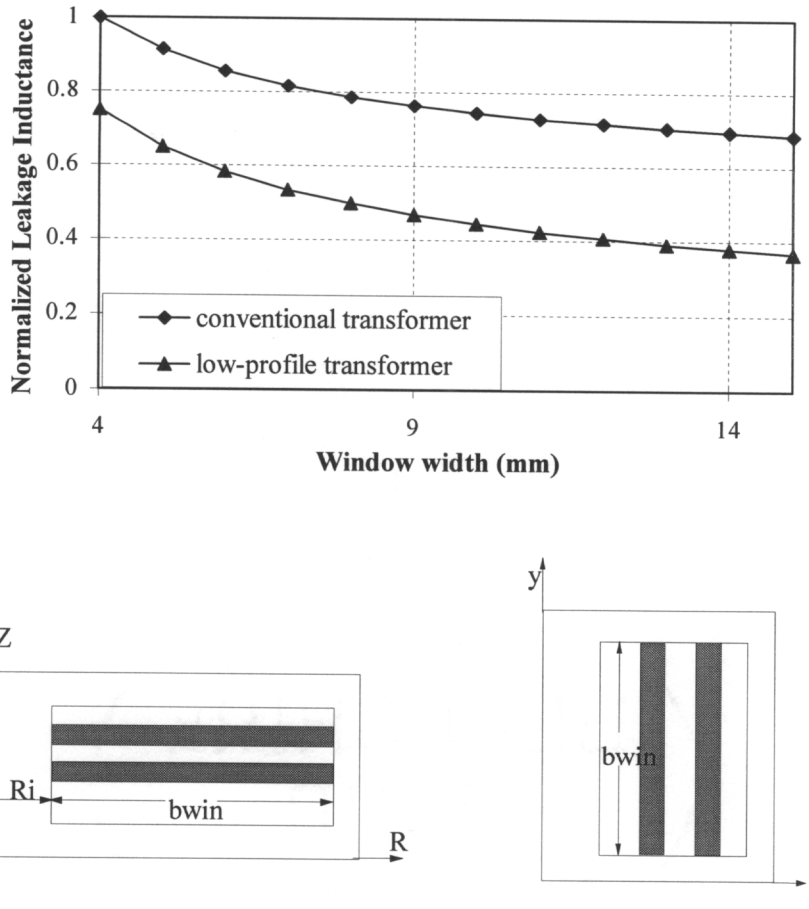

Fig. 2.8 Comparison of the leakage inductance of the low-profile transformer and the conventional transformer. The low-profile transformer and the conventional transformer have the same winding thickness and window width.

2.4 *Experimental Verification*

To check the theoretical results, calculated values of ac-resistance and leakage inductance are compared with the measured values of short-circuit resistance and inductance. Measured data were obtained in short circuit tests performed on several transformers over the frequency range of 1 kHz to 10 MHz using HP 4129A impedance analyzer. Great care was taken to minimize the inductance of the leads by keeping them as short as possible and minimizing loop areas.

Winding diagrams for test transformers are shown in Fig. 2.9. Transformer (a) is a four layer 18:9 transformer with the winding arrangement of P-S-P-S. Each layer is a 9-turn spiral winding, constructed of 24# AWG solid wire, two primary layers are connected in series to construct 18 primary turns, and two secondary layers are connected in parallel to construct 9 secondary turns. Transformer (b) is a four layer 18:9 transformer with the winding arrangement of S-P-P-S. It has the same winding construction as transformer (a). Both transformers use RM10 core. The predicted and measured results for each transformer are shown in Fig. 2.10. The curve of predicted data were calculated by computer using equations (2.27) and (2.34), the dimensions of the windings measured during construction of the transformer are given in caption of Fig. 2.8, and a conductivity $\sigma_{cu} = 5.8 \times 10^7$ S/m for copper wire and copper foil at $25^{o}C$.

Over most of the frequency range shown in figure 2.10, the prediction of ac-resistance and leakage inductance values agrees well with the measured values, although the predicted values are consistently a little lower than the measured values. The difference between the measured and predicted results changes with the winding arrangement and frequency. The finite element analysis reveals that the largest component of this mismatch can be attributed to the significant space, visible in Fig. 2.1, between the end of the winding layers and the core material. This edge effect causes the magnetic field intensity in the vicinity of the conductors to be greater than calculated for the equivalent foil layers, which results in greater magnetic energy storage and larger leakage inductance. Other contributors to the measured short circuit ac-resistance and leakage inductance that are neglected in calculations are terminations.

The dramatic increase in the measured short circuit inductance in Fig. 2.10 as the frequency drops toward 1 kHz is caused by magnetizing inductance, neglected in the calculations. This disagreement between the calculated leakage inductance and the measured short circuit inductance can be understood by considering a T-equivalent circuit.

During a short-circuit test, the two winding transformer can be modeled by the T-equivalent circuit in Fig. 2.11. The T-equivalent circuit is supplemented by the addition of C_w to represent the effective winding capacitance measured at primary with secondary on open circuit. The elements drawn with dashed lines represent effects that are

neglected in the field analysis of section 2.1; therefore, the calculated leakage inductance and ac-resistance are expected to predict short-circuit impedance accurately only in the frequency range where the dashed-line elements have negligible effect on the impedance of the T-equivalent circuit. In this frequency range, the winding capacitance *Cw* is sufficiently small, and the magnetizing inductance *Lm* and core-loss resistance *Rm* are sufficiently large to appear as open circuit. When this is the case, the short circuit test inductance *Llk* is virtually the same as the leakage inductance $L_{lk} = L_s' + L_p$, and the short circuit resistance *Rac* is virtually the same as the leakage inductance $R_{ac} = R_s' + R_p$.

Except for the magnetizing inductance effect already discussed, the agreement between measured and predicted data is good at frequencies below about 1 MHz. At higher frequencies, a parallel resonance between the winding capacitance *Cw*, neglected in the field analysis, and the leakage inductance $(L_s' + L_p)$ can cause deviation of the measured data from the predicted curve. However, since the most interesting frequency ranges of power supply transformers are lower than 1 MHz, the impedance characteristic at high frequency (> 1 MHz) has not been shown. Therefore, the element *Lm* has an effect only at very low frequencies, and *Cw* has an effect only at very high frequencies.

As shown in Fig. 2.10, transformer (a) and transformer (b) have different ac-resistances and leakage inductances due to the different winding arrangements. However,

the 1-D analytical method gives the same ac-resistance and leakage inductance for the two winding structures. The reason can be explained as follows:

As shown in Fig. 2.1, in 1-D analytical solution, any winding structure will be transferred into an equivalent foil winding layer. And ac-resistance and leakage inductance are proportional to the field intensity ratio α at the conductor surface, as shown in equations (2.27) and (2.34). Therefore, the interleaved (P-S-P-S) or sandwiched (S-P-P-S) winding structure will have the same magnetic field intensity at conductor surfaces, and therefore the same value of α, once they have been transferred into equivalent-foil winding layer. As a result, they have the same values of power dissipation and energy storage in transformer, and hence same ac-resistance and leakage inductance. That is a big limitation of the 1-D method.

The winding diagrams and short circuit quantities for E-core transformers are shown in Figs. 2.12 and 2.13. The test and prediction data shown are for EE core transformers. In Fig. 2.12, both transformers have a turns ratio of 4:1. Transformer (a) is a five-layer transformer with a four-layer primary and a one-layer secondary. Each primary layer is a two-turn spiral winding constructed by one-ounce double-side PCB. The secondary layer is constructed by 7-mil copper foil. Transformer (b) is a 6-layer structure with four turn of primary in series to construct a four-turn primary, and two turns of secondary in parallel to construct a one-turn secondary. The results show that the predicted values of ac-resistance and leakage inductance agree well with the measured

values for EE core transformer as well. So, the winding model works for planar windings for any kinds of core geometry.

2.5 Summary

This chapter presents an analytical method for predicting ac-resistance and leakage inductance of low-profile transformers at any frequency. The analytical expressions which depend only on the winding geometry and the frequency of sinusoidal excitation are derived. The differences between low-profile transformers and conventional transformers related to field distribution, power dissipation, and energy storage are explored. Calculated ac-resistance and leakage inductance are shown to predict short-circuit impedance well over a wide frequency range, and differences are explained by effects not included in the field analysis.

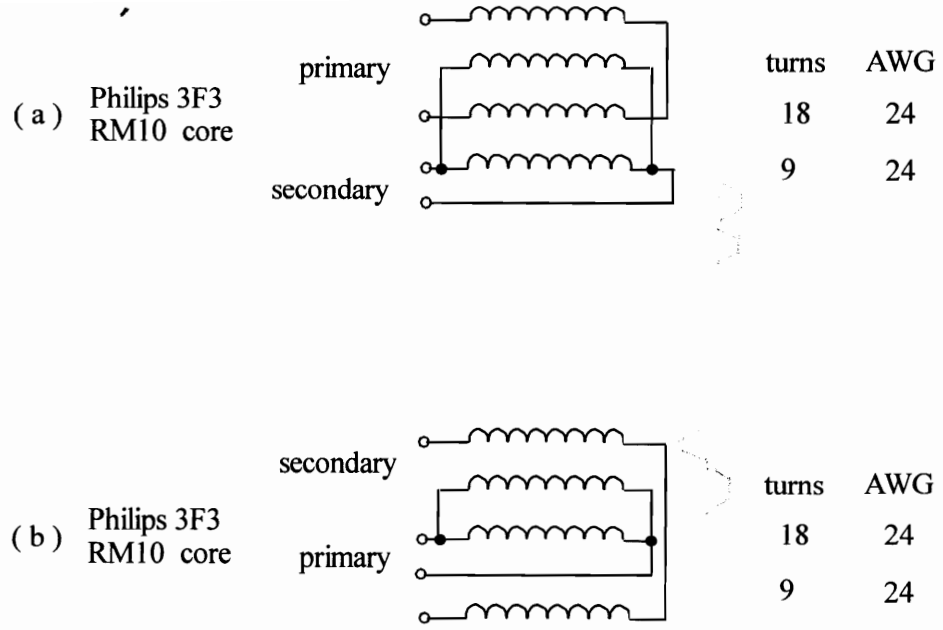

Fig. 2.9 Winding arrangements for verification: (a) 9-turn spiral winding layer with 24 # AWG solid wire and RM10 core, which has interleaved winding arrangement S-P-S-P. (b) 9-turn spiral winding layer with 24 # AWG solid wire and RM10 core, which has sandwich winding arrangement P-S-S-P. With reference to Fig. 4.1, $b_{win} = 5.475$ mm , and the mean length per turn of the winding is 50.79 mm.

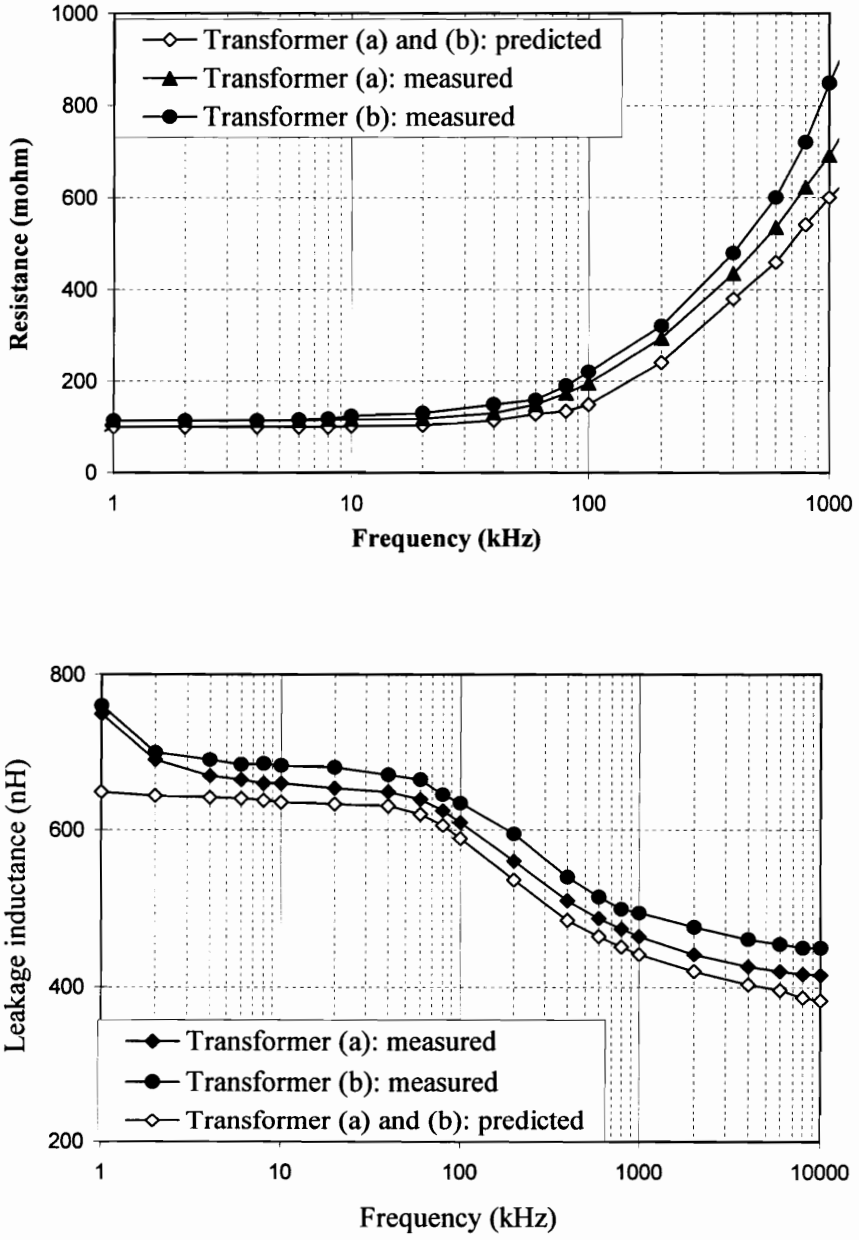

Fig. 2.10 Predicted and measured short circuit test data for winding structures in Fig. 2.9. For these interleaving arrangements, the difference between the measurement and prediction results is below 8.6% for power dissipation, and 10.4% for energy storage over most of the frequency range.

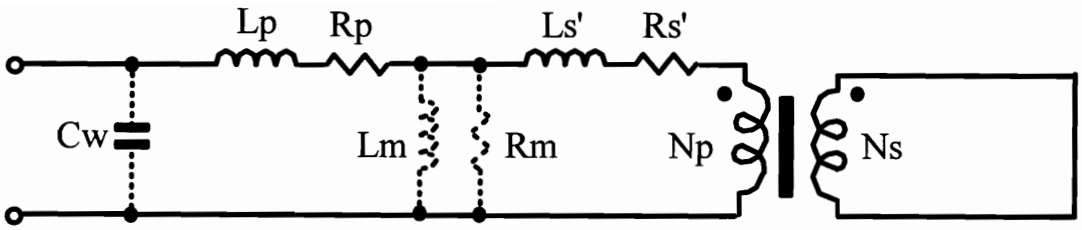

Fig. 2.11 T-equivalent circuit used to model a two-winding transformer during a short circuit test. The effective winding capacitance *Cw* has been added to the T-equivalent circuit, and the stray elements labeled with primed symbols are referred from the secondary side. The effects of the elements drawn with dashed lines are not included in the field analysis.

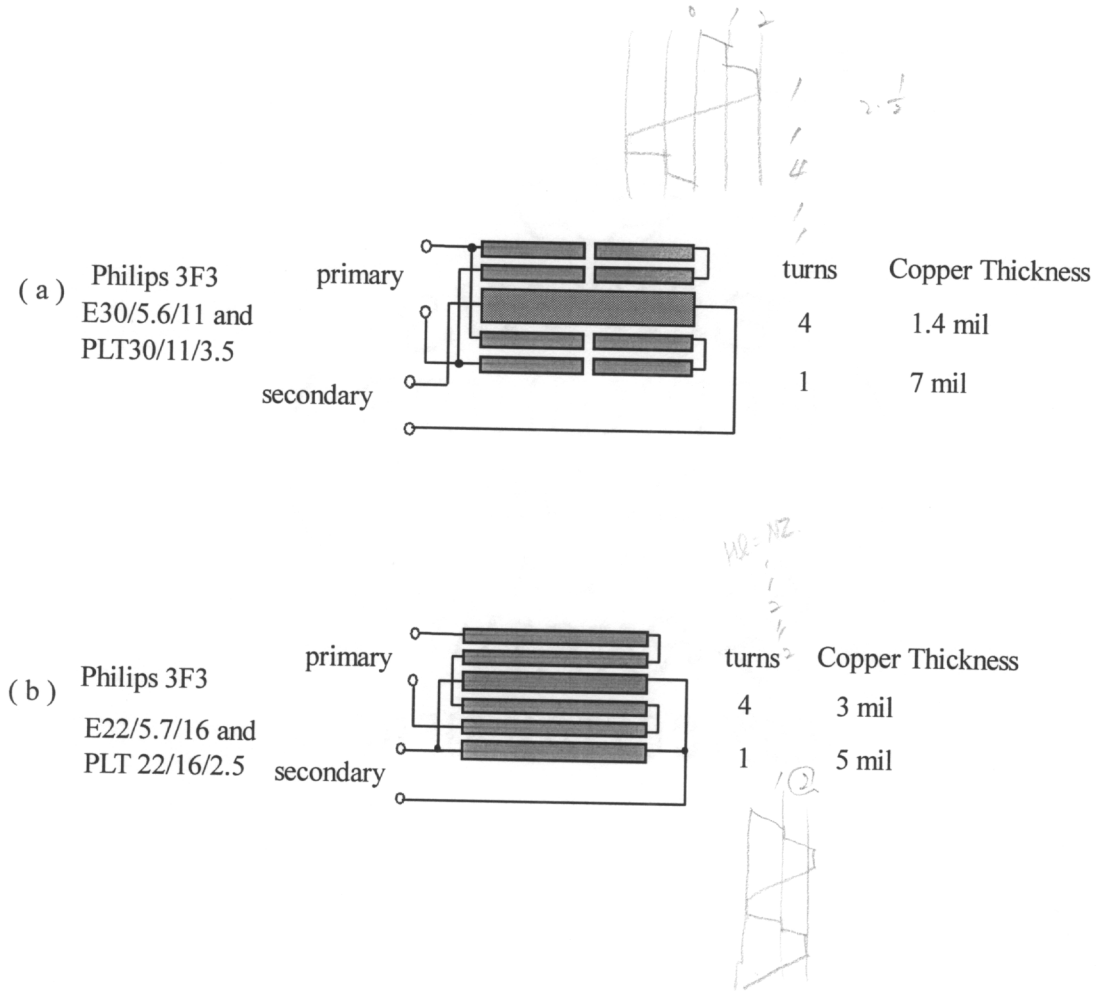

Fig. 2.12 Winding diagrams for (a) a 5-layer spiral winding transformer with window width of 7.3 mm, primary winding width of 2.8 mm, and secondary winding width of 7 mm. (b) a 6-layer planar winding transformer with window width of 5.9 mm, winding width of 5.7 mm.

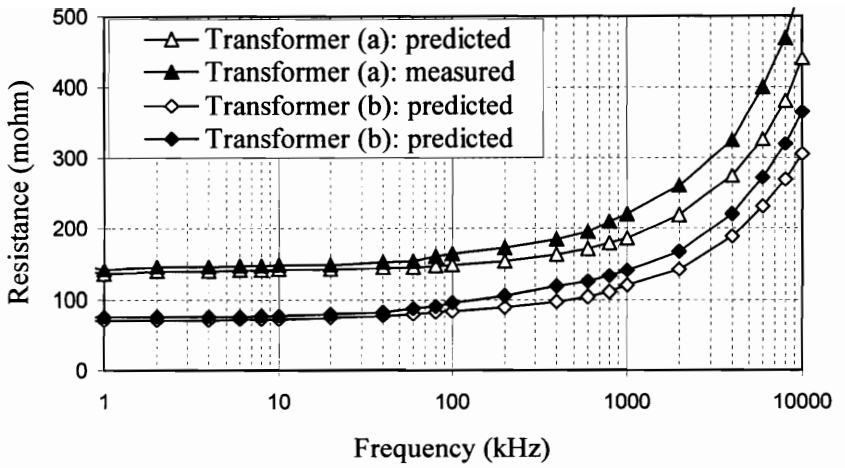

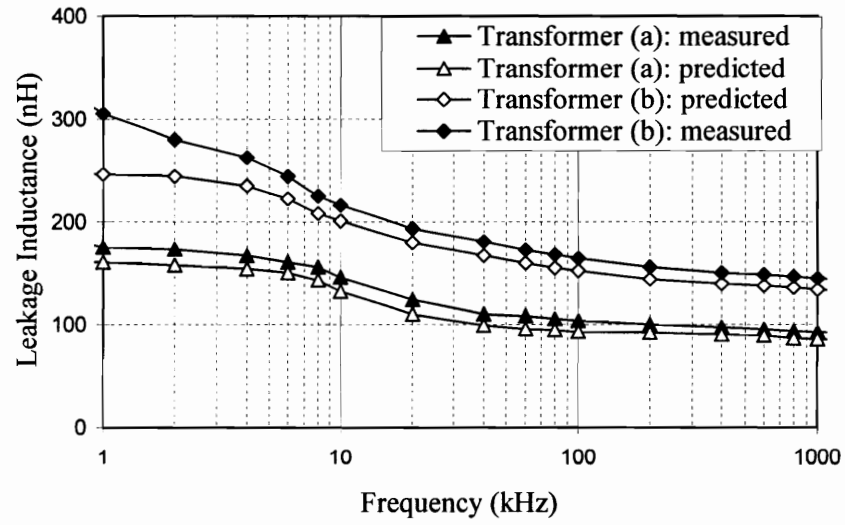

Fig. 2.13 Predicted and measured short circuit test data for winding structures in Fig. 2.12. For these non-interleaving arrangements, the difference between the measurement and prediction results is below 13.6% for power dissipation, and 14.74% for energy storage over most of the frequency range.

Chapter 3

High-Frequency Eddy-Current Effects in Low-Profile Transformer Windings

Low-profile transformer ac-resistance and leakage inductance are predicted in Chapter 2 based on a one-dimensional field analysis using an equivalent foil approximation of each winding layer. However, these predictions are observed to be consistently lower than measured short-circuit resistance and inductance, whereas each short-circuit resistance and inductance are essentially the same as the corresponding ac-resistance and leakage inductance of the transformers. And the 1-D analytical method cannot predict differences in performance of different winding arrangements such as P-S-P-S and P-S-S-P.

In this chapter, a numerical approach is used, namely the finite-element analysis (FEA) is used to investigate the characteristics of different winding arrangements. An

FEA ac-field solver can be used to calculate the field and current distributions and respective energy storage and losses in the transformer. It gives a clear picture of regions of high leakage fields and strong current crowding, and this information is quite useful in minimizing the losses in the winding.

All real transformer structures are actually three-dimensional in nature. An accurate and complete solution would require solving the 3-D problem. However, the 3-D numerical method requires tremendous memory and very long execution times and results in an uneconomical solution. Therefore, the 2-D FEA is more practical. Two-dimensional solutions exploit the 2-D behavior in a given cross section, and then assume that it is repeated in all other sections in the third dimension. In other words, an axisymmetrical core shape is assumed, which would not be true for any practical core (except a pot core). In order to show the degree of deviation of the 2-D solution in different cross sections, two cases (shown in Fig. 3.1) are compared.

Consider an RM type core shown in Fig. 3.1. Two normal sections, A-A' and B-B', are taken. Sectional A-A' shows a geometry in which the windings are completely enclosed by a magnetic core. Section B-B', however, shows only the core center leg, and the windings are not completely enclosed by the core. As shown in Fig. 3.2, the leakage field distributions in the two cases are almost the same. The field distribution is quite similar to the leakage field distributions shown in Fig. 3.2. It indicates that the leakage field is dominated by the winding arrangement. The corresponding ac-resistance and

leakage inductance were calculated for both sections. These curves are shown in Fig. 3.3. As is clear, the ac-resistance and leakage inductance are entirely dominated by the winding arrangement, while the existence of the core has a very minor effect. This provides a good indication that 2-D results which have been carried over from totally enclosed cross sections provide a good approximation to results obtained in non-axisymmetric structures such as EE cores, RM cores, PQ core, ETD core, and RD cores, that are widely used to build transformers.

This chapter evaluates the design options associated with the transformer with planar winding configurations in a 100-W @ 3.3-V, 300-kHz active clamp forward converter (as shown in Fig. 3.4) with maximum height of 6 mm. Several winding configurations with different wire types are characterized using 2-D Finite Element Analysis (FEA), to calculate the eddy current and magnetic field distribution. An appropriate winding configuration with the lowest ac-resistance and leakage inductance is selected.

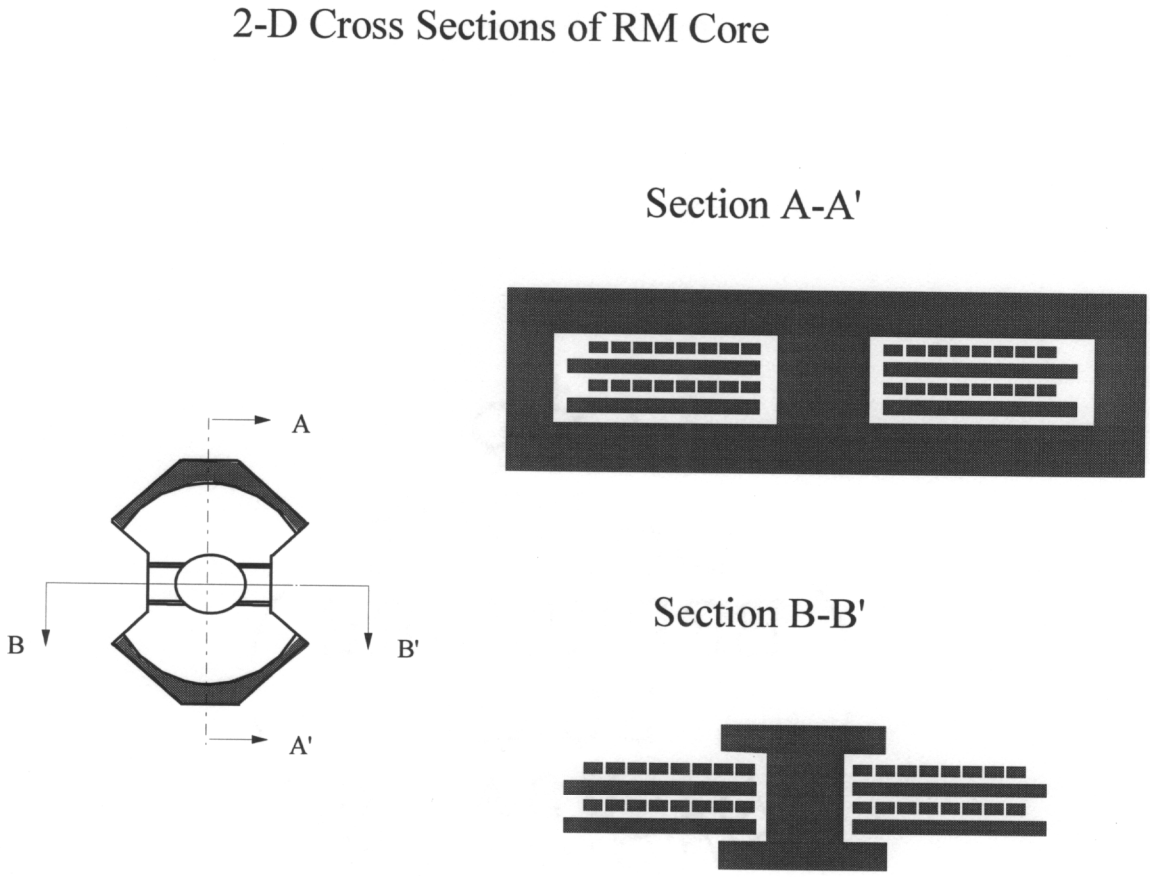

Fig. 3.1 Two cross sections in an RM type core. In section A-A', the windings are enclosed in the ferrite window. In section B-B', the core center leg and top and bottom plates appear; the windings are not completely surrounded by ferrite.

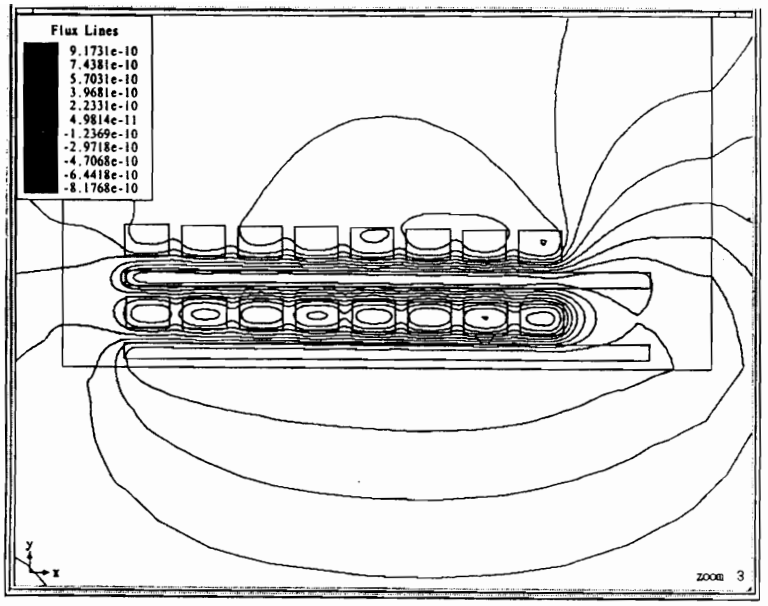

(a) leakage distribution in section A-A'.

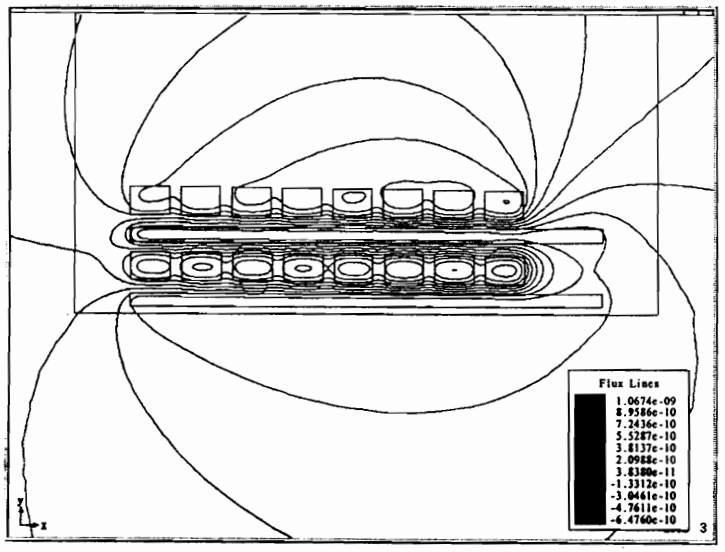

(b) leakage distribution in section B-B'.

Fig. 3.2 Leakage field distributions in sections A-A' and B-B'. The field distributions in the two sections are almost the same. The field is only slightly different at the boundary between core and window areas. It indicates that the leakage field is dominated by the winding arrangement.

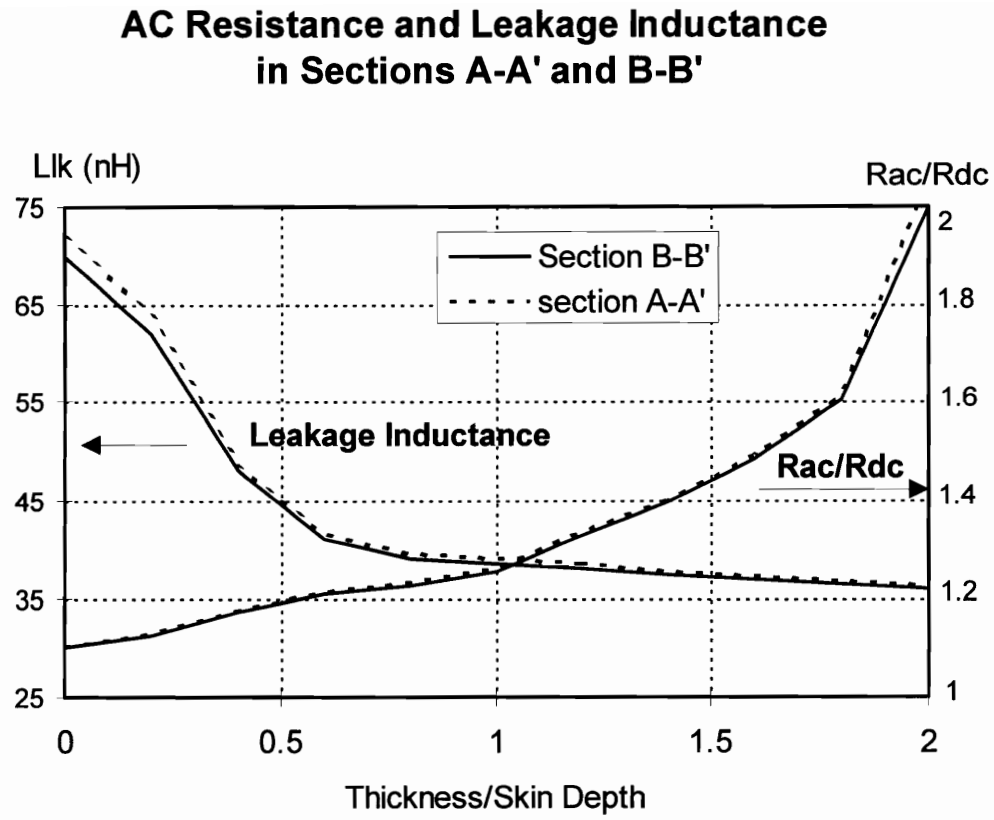

Fig. 3.3 The FEA calculated ac/dc resistance and leakage inductance of sections A-A' (dashed) and B-B' (solid) vs. normalized frequency. The results show that ac-resistance and leakage inductance are dominated by the winding arrangement, and are not affected by the presence of the core.

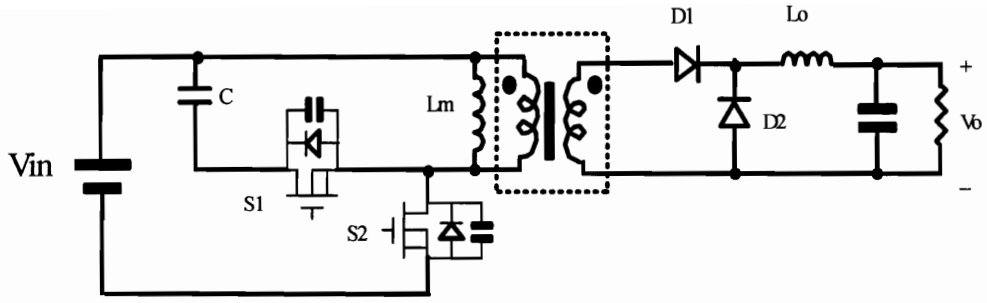

Fig. 3.4 Circuit diagram of an active clamp forward converter. The height of the transformer should be lower than 6 mm in order to meet package requirement.

3.1 Low-Profile Transformer Winding Arrangements and Winding Constructions

With a pot core transformer model, eight different winding types, six for wire-foil winding patterns, and two for all-foil winding patterns (shown in Fig. 3.5), are evaluated using a two-dimensional FEA solver. The winding configurations involve various interleaving arrangements and wire types, including solid wire, printed wire, Litz wire, and copper foils. For all winding configurations studied, the turns ratio is 4:1, with four primary turns and one secondary turn. The resistance and inductance for these different winding structures are calculated with the dimensions of an RM10 core, as shown in Fig. 3.6.

3.1.1 Wire-Foil Winding Patterns

As shown in Fig. 3.5, Cases 1-3 are solid wire-foil winding arrangements. S-P-P-S, P-S-S-P and S-P-S-P are four-layer structures with two wire-wound primary layers and two foil secondary layers. Each primary layer is a two-wire-parallel four-turns spiral winding. Two primary layers and two secondary layers are parallel to construct a four-turn primary and a one- turn secondary, respectively. The solid wire is 28 AWG with a cross-sectional area of 0.11 mm^2. The Litz wire is considered to have the same effective

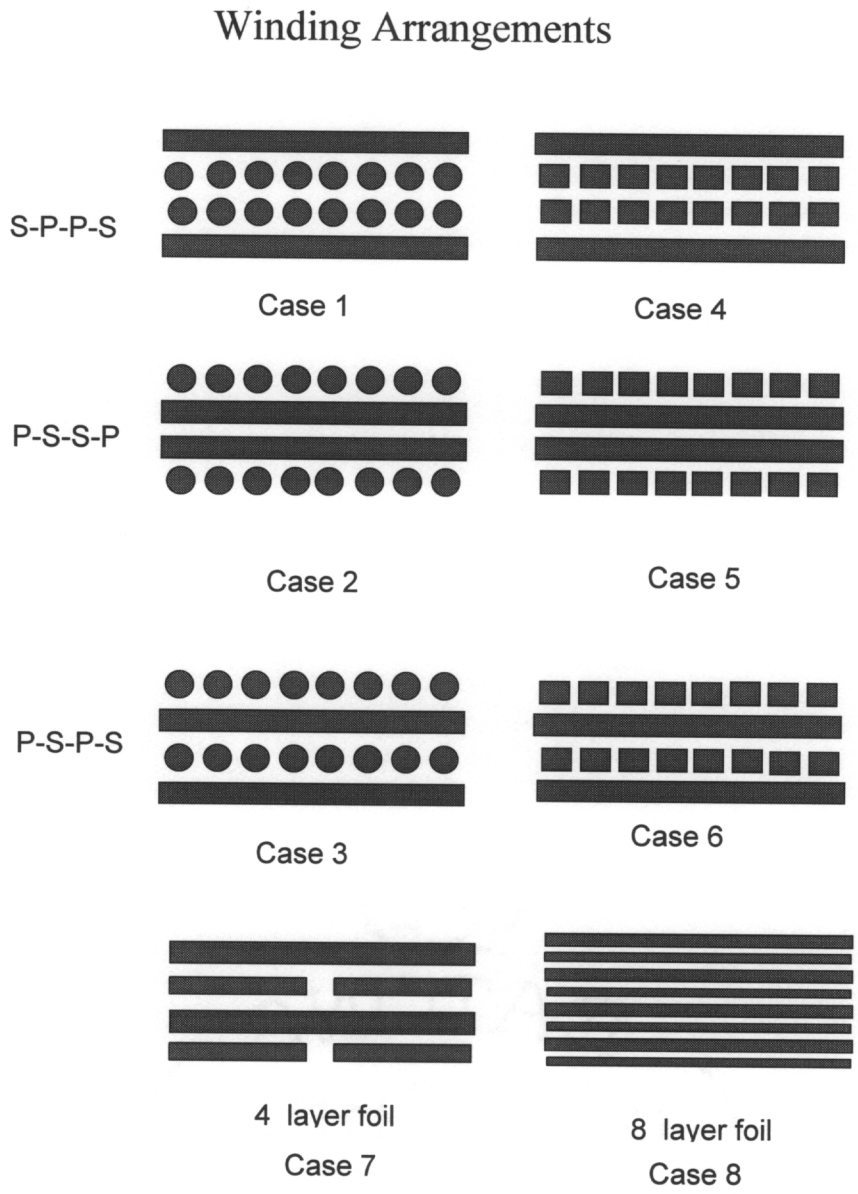

Fig. 3.5. Various winding configurations. S-P-P-S, P-S-S-P and S-P-S-P are four-layer structures with two wire-wound primary layers and two foil secondary layers. "P" represents a primary winding layer, and "S" represents a secondary winding layer. Cases 1-3 use 28# AWG solid wire for the primary. Cases 4-6 use 7 mil printed-wire for the primary. Cases 7 and 8 use 5-mil copper foil. The secondary has a thickness of 5 mil for cases 1-7 and of 3 mil for case 8.

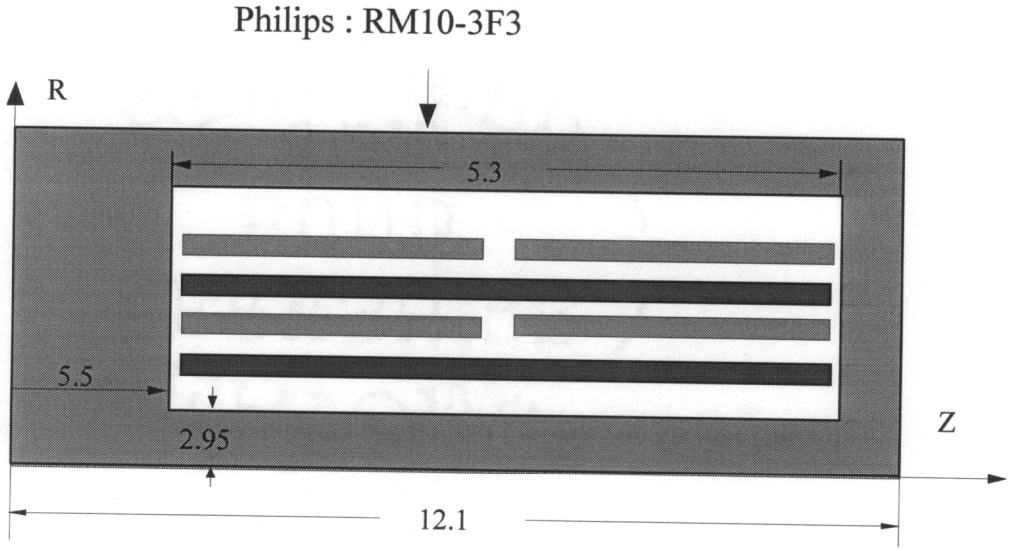

Dimensions in mm, unless otherwise noted.

Fig. 3.6 Dimensions of an RM10 core. The dimensions represent the window in the enclosed region of an RM10 core.

cross-sectional area as the solid wire, and is modeled as a solid wire that has no eddy current in it. Cases 3-6 are four-layer structures with a printed-wire primary: two layers for the primary and two layers for the secondary. The two primary layers, consisting of four bifilar turns each, are connected in parallel to construct a four-turn winding. The distance between each two primary turns is 3 mil. The primary winding conductors have a thickness of 7 mil and the same cross-sectional area as the 28# gauge conductors used in solid wire windings of cases 1, 2, and 3. The secondary is constructed of two parallel connected five-mil copper foils.

3.1.2 Copper Foil Winding Patterns

Two copper foil winding patterns are also shown in Fig. 3.5. Case 7 is a four-layer foil structure, P-S-P-S, with two layers for the primary winding and two layers for the secondary winding. Each primary layer is a two-turn spiral winding. The primary winding conductors have a thickness of 0.127 mm (5 mil). The distance between each two primary turns is 0.127 mm (5 mils). The secondary is constructed of two parallel-connected five-mil copper foils. Case 8 is the all-foil 8-layer structure made of copper foils that are fully interleaved. The primary consists of four-layer copper foils connected in series to form a four-turn winding. Each primary layer has a thickness of 0.127 (mm). The secondary is constructed of four parallel-connected turns, with each turn constructed of 3 mil copper foil.

3.2 Field and Current Density Distribution

3.2.1 Wire-Foil Winding Patterns

Solid Wire Primary

Case 1 The magnetic field and current distributions in the window area of the core for the S-P-P-S with a solid wire primary (Case 1) are shown in Fig. 3.7. The field is expelled from the central portions of the winding and bent at the top of the primary winding, which results in current crowding at the interface region. This winding arrangement results in a resistance of 107.35 mΩ and 200.5 nH leakage inductance.

Case 2 Figure 3.8 shows the field and current distributions of the winding arrangement P-S-S-P with a solid wire primary. This winding arrangement makes a little better utilization of the primary conductors, because magnetic field exists on the upper and lower sides of the primary winding, which allows the eddy current to flow on the non-interleaving side. It results in a lower ac-resistance of the primary winding (67.4 mΩ) compared to that of Case 1 (71.9 mΩ), whereas secondary winding resistance is 35.45 m Ω for both cases. As a result, it has a lower resistance (102.9 mΩ) compared to that of Case 1.

Case 3 Figure 3.9 shows the field and current distributions of the winding arrangement S-P-S-P with a solid wire primary. For this case, the foil is used more effectively and has a more uniform current distribution, which lowers the ac-resistance (96.6 mΩ).

Figures 3.10, 3.11, and 3.12 show the magnitude of field intensity along the secondary foil surface (lines of AB and CD) and the center of the primary winding (lines of A'B' and C'D') in cases 1, 2, and 3. The plots display that the interleaving structure S-P-S-P (Case 3) has the lowest magnetic field intensity in the transformer window area, and the sandwiched structure P-S-S-P (Case 2) has the highest leakage field intensity. As a result, Case 3 has the lowest leakage inductance (178.4 nH), and Case 2 has the highest leakage inductance (206.5 nH), since the leakage inductance is proportional to the magnitude of leakage field intensity.

Figure 3.13 gives the plot of ac-resistance and leakage inductance of the three winding arrangements at different frequencies based on the FEA method and compared with the one-dimensional method. It shows that the one-dimensional method fails to show the differences between these three winding structures and just simply gives the same ac-resistance and leakage inductance. The FEA exposes the values of ac-resistance, and leakage inductance of the interleaving winding structure S-P-S-P is much lower than that of the other two sandwiched structures. It demonstrates that the one-dimensional

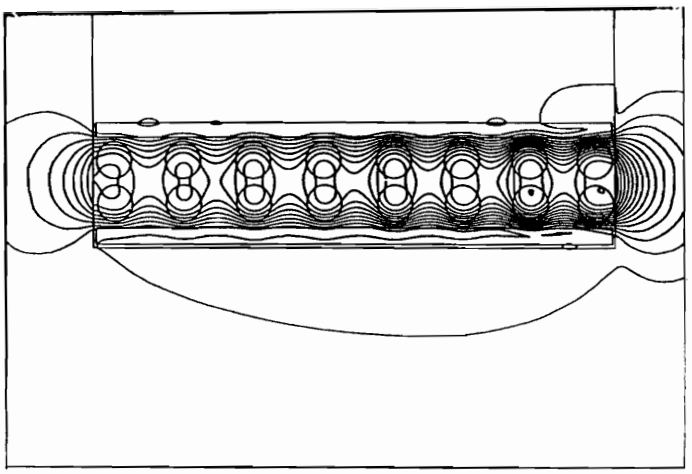

(a) Field distribution

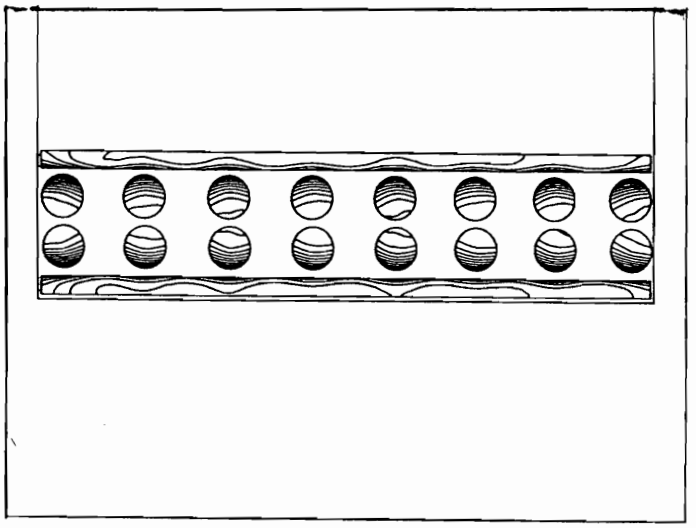

(b) Current density distribution

Fig. 3.7 The magnetic field and current distributions of the **S-P-P-S (case 1)** winding arrangement with **solid wire** at 300 kHz. The field is expelled from the central portions of the winding, which results in current crowding at the interface region. This winding arrangement has a 107.35-mΩ ac-resistance and leakage inductance of 200.5 nH.

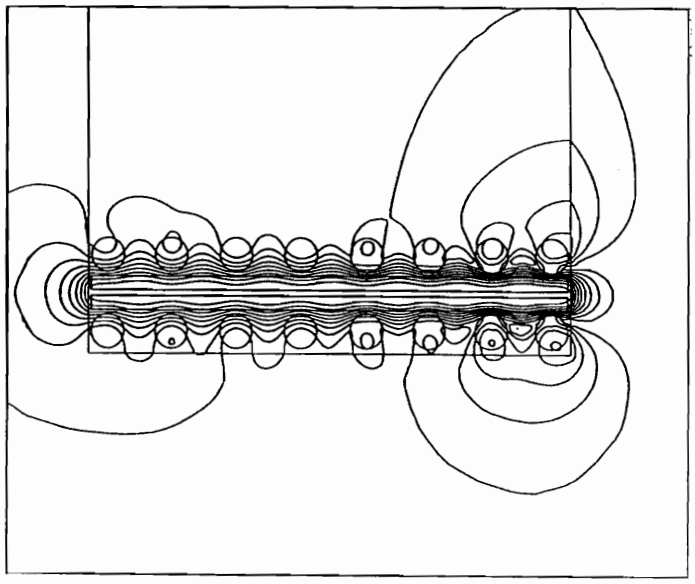

(a) Field Distribution

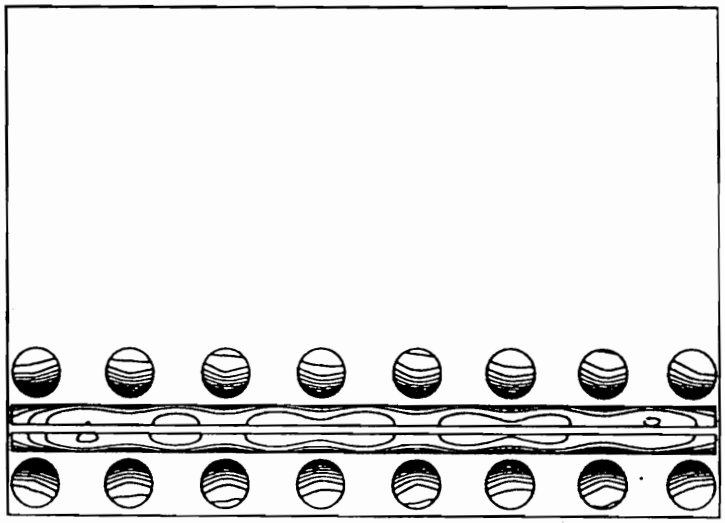

(b) Current Density Distribution

Fig. 3.8 The magnetic field and current density distribution of the **P-S-S-P (case 2)** winding arrangement with **solid wire** at 300 kHz. This winding arrangement makes a little better utilization of the primary conductors because magnetic field exists on the upper and lower sides of the primary winding, which allows the eddy current to flow on the non-interleaving side. As a result, it has a 102.9-mΩ ac-resistance and 206.5-nH leakage inductance.

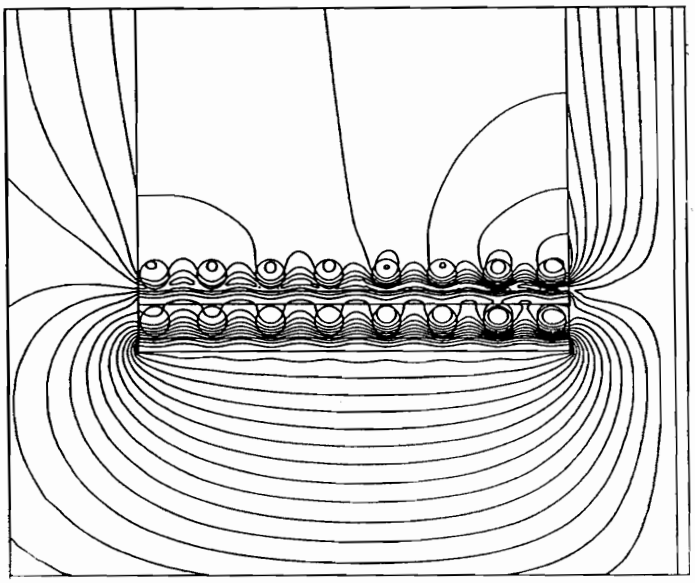

(a) Field Distribution

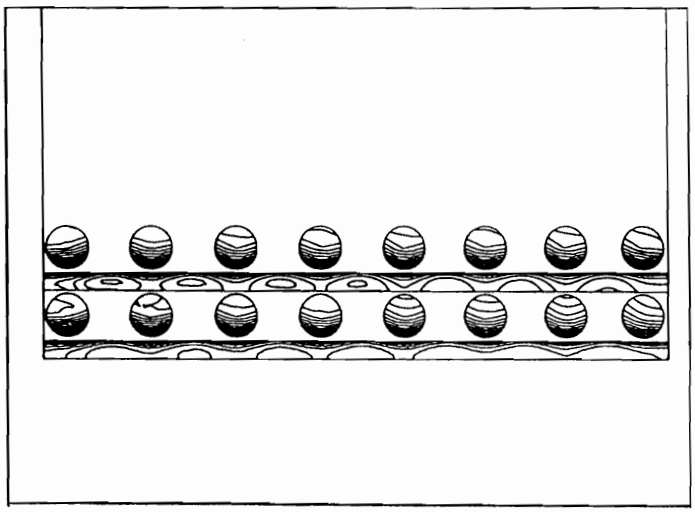

(b) Current Density Distribution

Fig. 3.9 The magnetic field and current distribution of the **S-P-S-P (case 3)** winding arrangement with **solid wire** at 300 kHz. There is a larger tangential component of magnetic field compared to the previous two cases. This winding arrangement has the ac-resistance of 96.6 mΩ and 178.4-nH leakage inductance.

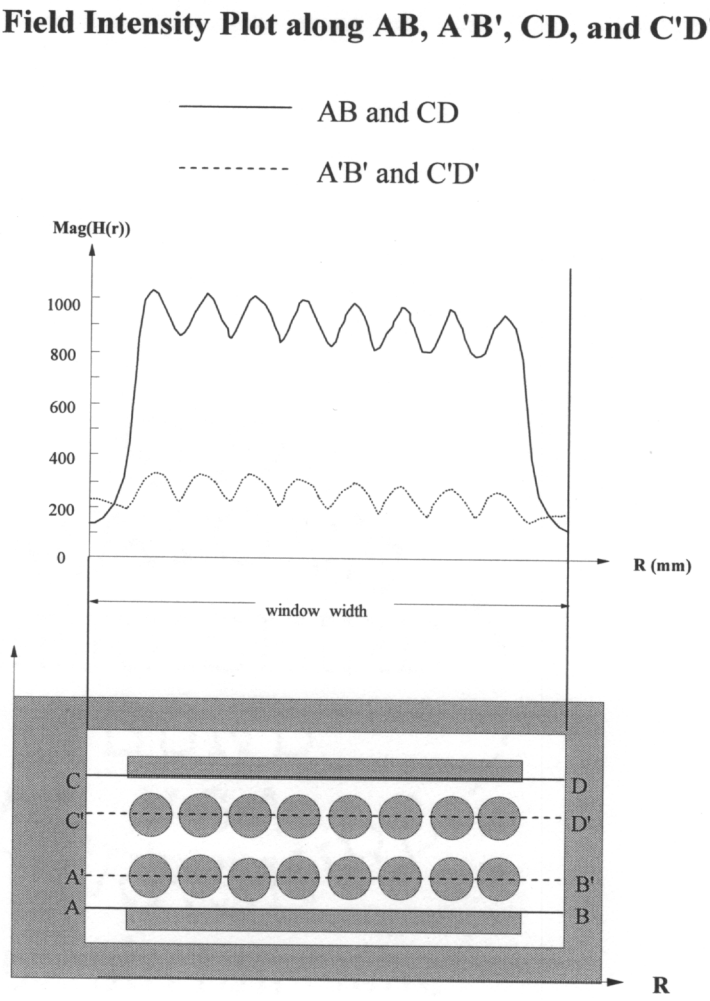

Fig. 3.10 Magnetic field intensity along the lines of AB and A'B' for **Case 1 (S-P-P-S)**.

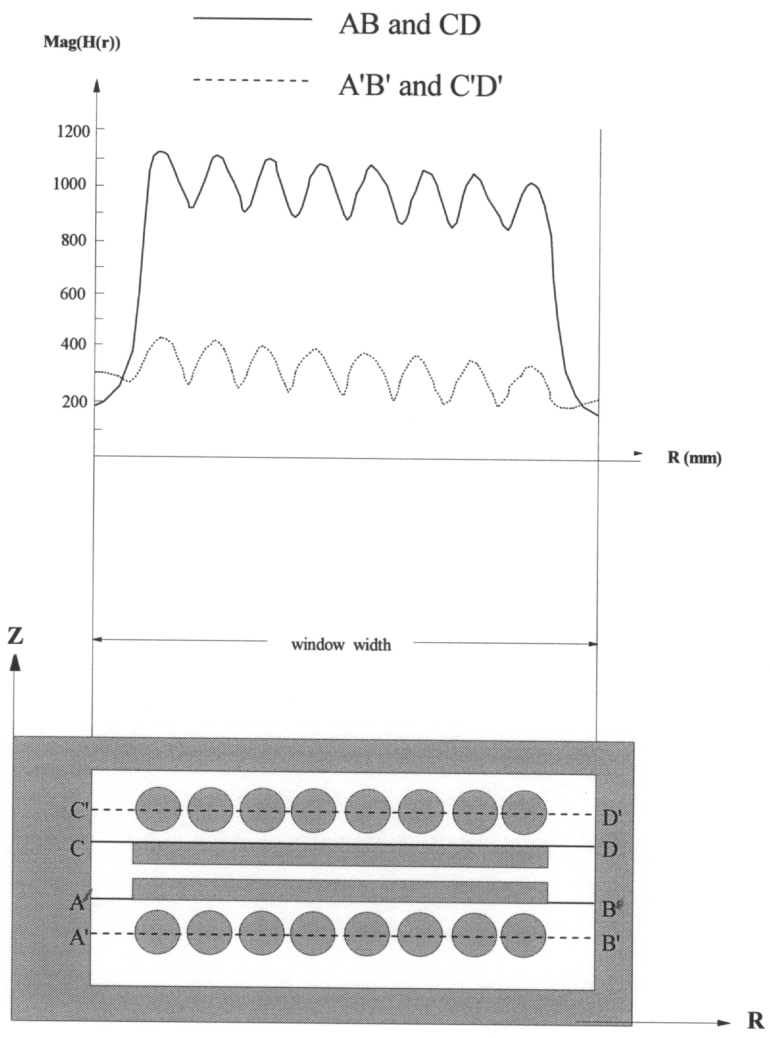

Fig. 3.11 Magnetic field intensity along the lines of AB and A'B' for **Case 2 (P-S-S-P)**.

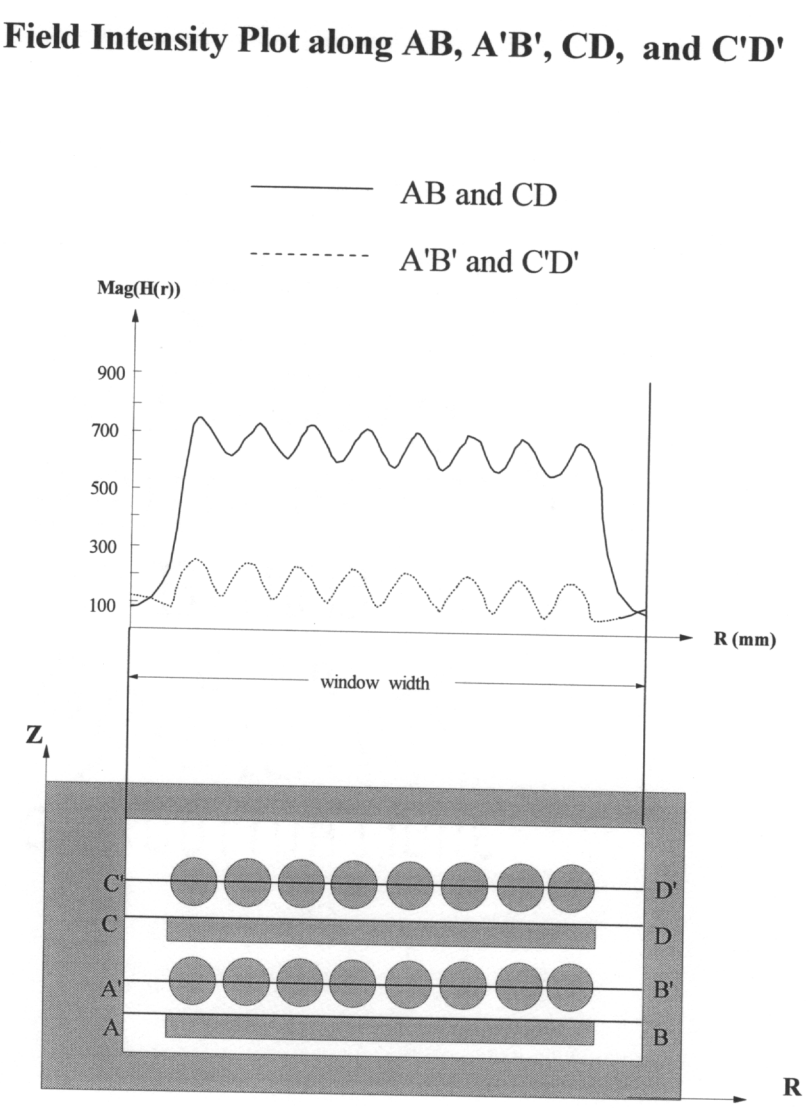

Fig. 3.12 Magnetic field intensity along the lines of AB and A'B' for **Case 3 (P-S-P-S)**. The interleaving structure S-P-S-P has the lowest leakage field intensity compared to P-S-P-S and S-P-P-S.

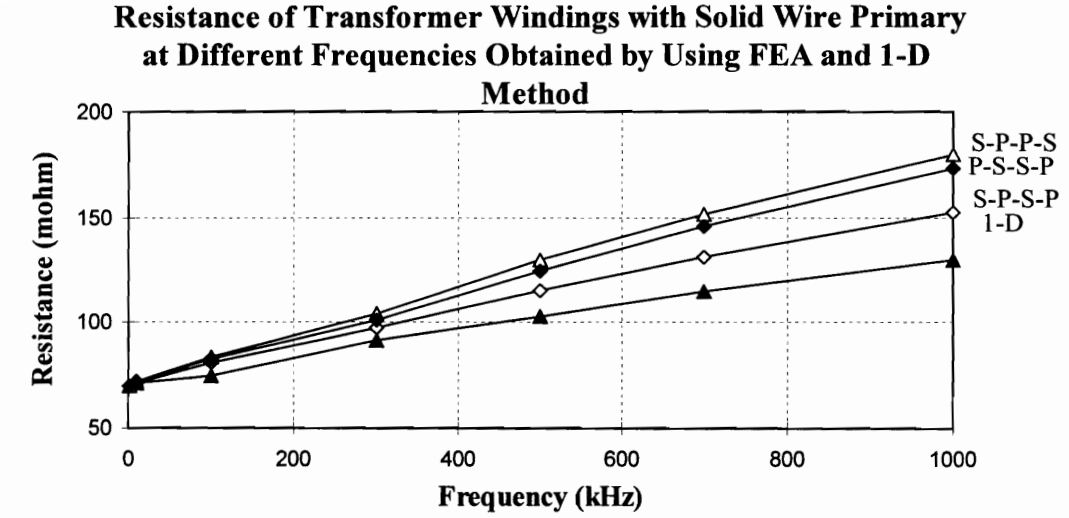

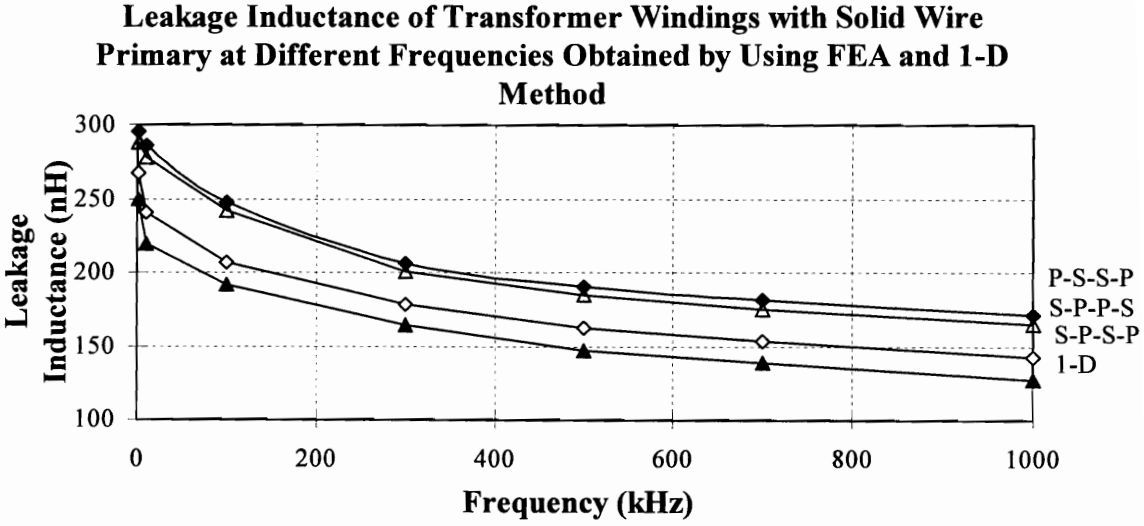

Fig. 3.13 The plots of ac-resistance and leakage inductance of the S-P-P-S, P-S-S-P, and S-P-S-P winding arrangements with a **solid wire primary** when frequency ranges from DC to 1 MHz. The 1-D method fails to show the difference among these three winding arrangements, and consequently predicts a lower resistance and leakage inductance. The FEA method shows the exact results.

method is not accurate enough to predict the characteristics of different winding arrangements.

One important aspect related to the winding configuration is the effect of the balance in the widths of the primary and secondary windings. For the interleaving winding structure S-P-S-P, there are two ways to implement the winding construction (as shown in Fig. 3.14), which include the primary winding width being less than that of the secondary (designated as the unequal Case A), and the primary winding width being equal to that of the secondary (designated as the equal Case B). In Case A, the primary is tightly packed turn by turn. In Case B, the primary is evenly packed and fills the full window width.

Figures 3.15 shows the magnetic field and current density distribution for Case A. If the field distribution of Case A is compared with that of Case B, it is apparent that the area of the leakage field distributed between the top of the primary and the top edge of the foil is quite larger in Case A. It means that a considerable volume is used for energy storage in Case A. Furthermore, the equal $\bar{A}$ lines bending at the top of the primary causes a part of the secondary foil to be unused. The edge effect in Case A causes a relatively large normal magnetic field, which gives rise to high ac-resistance and leakage inductance. When the primary has the same width as the secondary, both the normal magnetic field and the volume in which the leakage energy exists are drastically reduced, and much more of the foil is used, as shown in Fig. 3.9. The ac resistance drops from

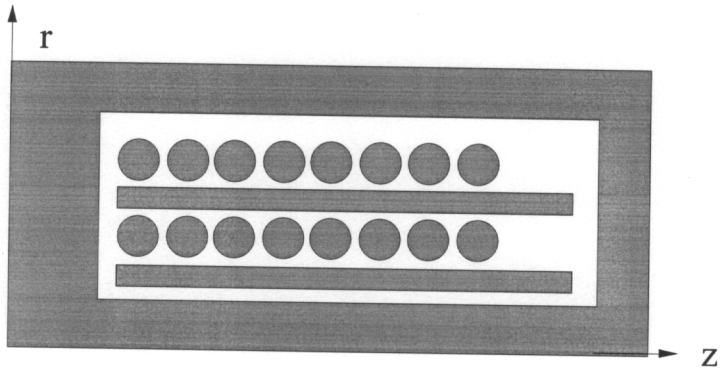

CASE A

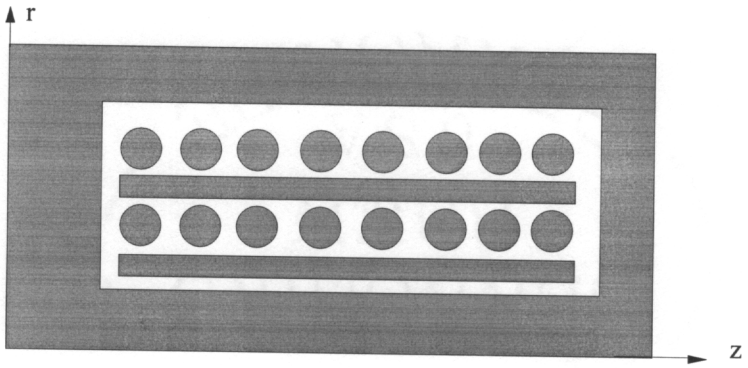

CASE B

Fig. 3.14 Two winding implementations for the winding arrangement P-S-P-S.

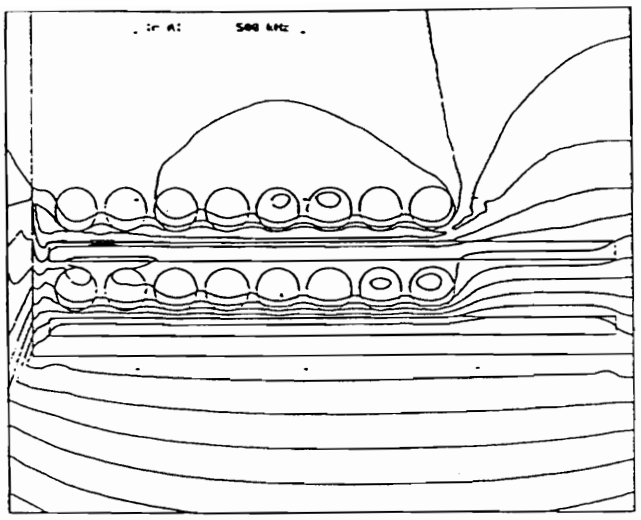

(a) Field Distribution

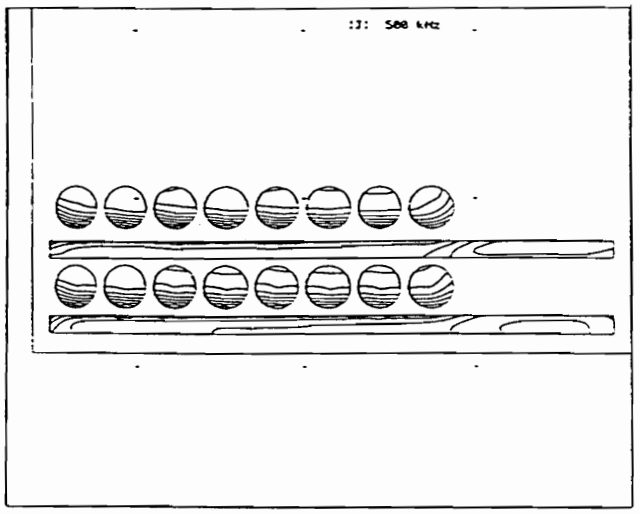

(b) Current Density Distribution

Fig. 3.15 The magnetic field and current distribution of the **unequal case (S-P-S-P** arrangement with **solid wire** at 300 kHz**),** in which the primary winding width is less than that of the secondary. It is apparent that the area of the leakage field distributed between the top of the primary and the top edge of the foil is quite larger than Case 3. This winding arrangement has the ac-resistance of 107.36 mΩ and 209.1 nH leakage inductance.

107.3 mΩ to 96.6 mΩ, and leakage inductance drops from 209.1 nH to 178.4 nH. There is a 9% reduction in ac-resistance and a 19% reduction in leakage inductance.

Litz Wire Primary

In dc applications, conductor resistance is easily reduced by merely increasing the cross-sectional area, and thereby reducing current density and hence also the power dissipation. At high frequency, however, ac resistance is reduced by trying to force a uniform current density and eliminate regions of high current density. A common way is to construct the wire from a number of thin insulated conductors or strands which are transposed or waved in some pattern that would achieve a uniform current distribution. Litz wire is constructed for this purpose so that the individual strands possess both azimuthal and radial transposition. This construction provides immunity against external proximity effects and internal skin effects. The purpose of this type of transposition is to force each strand to occupy all positions of every other strand comprising the wire. This will force the impedances of all the strands to be equal, resulting in an equal current distribution. So, Litz wire is modeled as a solid wire that has no eddy current in it in FEA.

Figure 3.16 shows the current density and field distributions of the S-P-S-P with a Litz wire primary. The Litz wire is 50/44# with the same effective cross-sectional area as that of a 26 AWG solid wire. The FEA results show that the transformer with Litz wire has lower ac-resistance, but higher leakage inductance than that with 26 AWG solid wire.

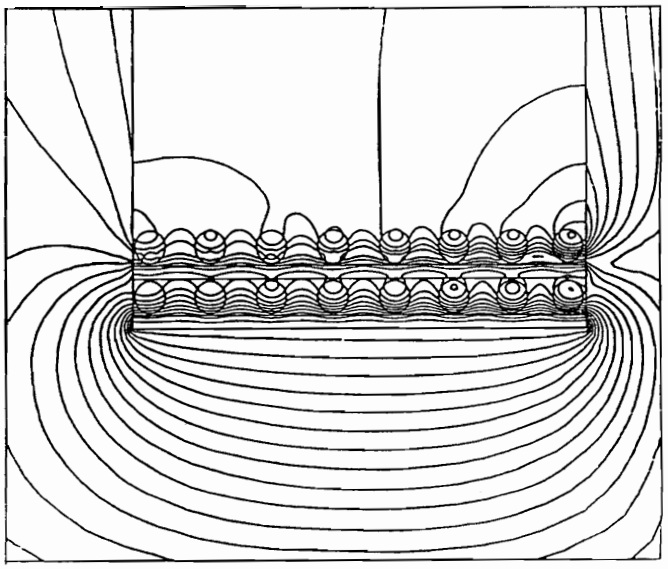

(a) Field Distribution

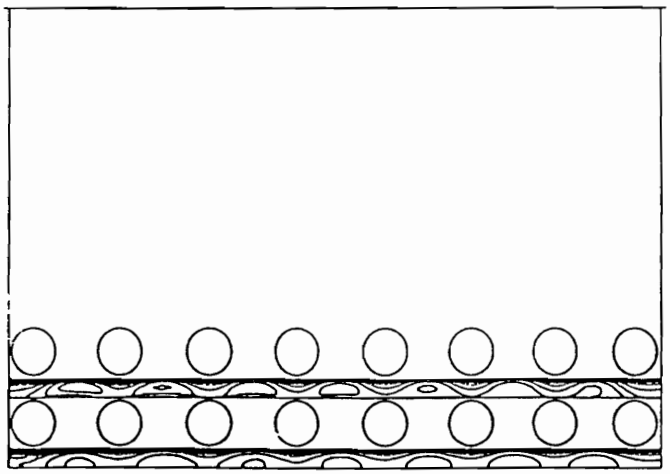

(b) Current Density Distribution

Fig. 3.16 The magnetic field and current density distribution of the **S-P-S-P** winding arrangement with **Litz wire** at **300 kHz**.

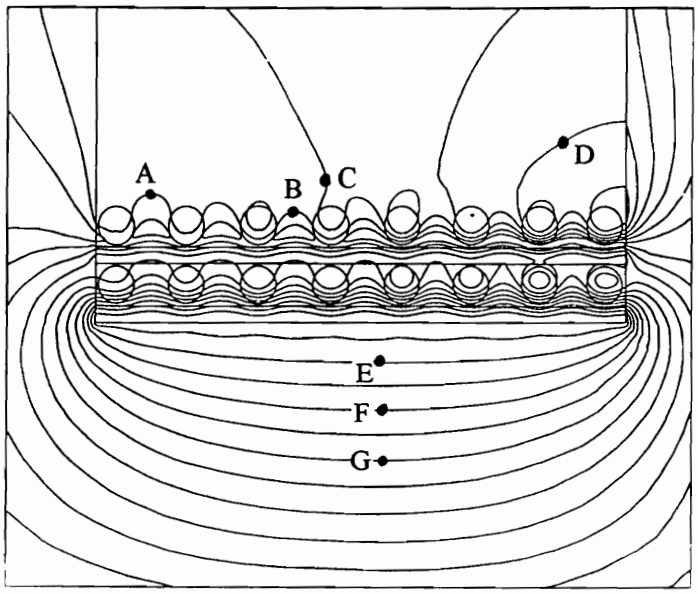

(a) Solid wire primary

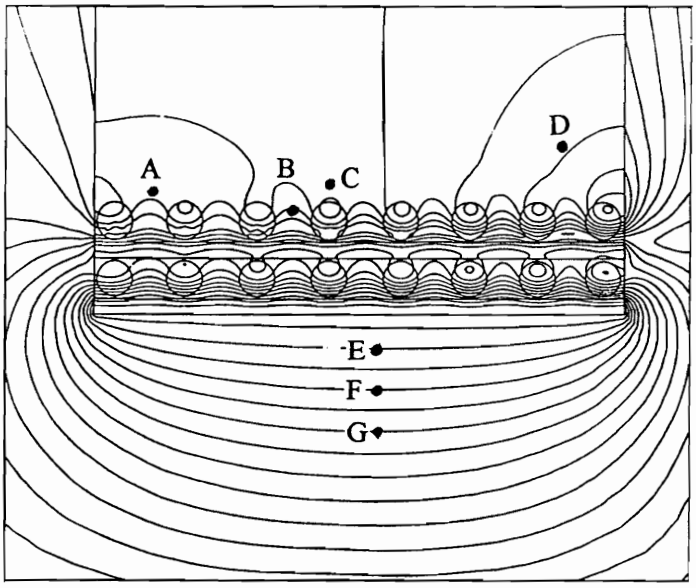

(b) Litz wire primary

Figure 3.17 Comparison of the leakage field distributions of the transformers with the Litz wire primary and solid wire primary arrangements.

The lower resistance is due to the uniform current distribution in the primary. The higher leakage inductance is due to the much higher magnetic field in the transformer window area. Figure 3.17 compares the leakage field distributions of the transformers with the Litz wire primary and solid wire primary arrangements. Table 3.1 shows some values of the magnetic field intensity at various points in the winding area of the Litz wire primary and solid wire primary arrangements. At all points shown, the magnetic field intensity in the Litz wire case is much higher than that of the solid wire case. Since the leakage inductance is given by the volume integral of the field intensity, the higher field intensity results in a higher leakage inductance. Therefore, for this winding structure, the leakage inductance is 337.54 nH, which is almost 2 times that of the transformer with the solid wire primary (178.4 nH), and the ac resistance is 78.34 mΩ, which is much lower than that of the solid wire case (96.57 mΩ).

Table 3.1 The Magnetic Field Intensity in the Transformer Window Area

	Magnetic Field Intensity (A/M)	
Point selected	Transformer with **solid** wire primary	Transformer with **Litz** wire primary
A	42.78	86.08
B	131.14	213.54
C	16.70	34.21
D	24.04	31.13
E	0.034	0.050
F	0.038	0.048
G	0.036	0.046
Leakage Inductance (nH)		
	178.4	337.54

Printed-Wire Primary

Case 4 Figure 3.18 shows the current and magnetic field distributions of the S-P-P-S winding arrangement with a printed-wire primary. Similarly as in the solid wire case, the field is expelled from the central portions of the winding and bent at the top of the primary winding, which results in current crowding at the interface region. This winding arrangement results in a resistance of 102.3 mΩ and a 175.5 nH leakage inductance.

Case 5 Figure 3.19 shows the current and magnetic field distributions of the P-S-S-P winding arrangement with printed-wire primary. Because magnetic field exists on the upper and lower sides of the primary winding, which allows the eddy current to flow on the non-interleaving side, the ac-resistance of the primary winding (62.75 mΩ) is lower compared to case 4 (66.85 mΩ). As a result, the transformer with the winding arrangement P-S-S-P (Case 5) has lower resistance (98.2 mΩ) compared to the transformer with winding arrangement S-P-P-S (Case 4).

Case 6 Figure 3.20 shows the current and magnetic field distributions of the S-P-S-P winding arrangement with a printed-wire primary. The interleaved winding arrangement P-S-P-S has the most uniform current distribution, which results in the lowest ac-resistance (92.66 mΩ) and leakage inductance (151.64 nH) compared to Cases 4 and 5.

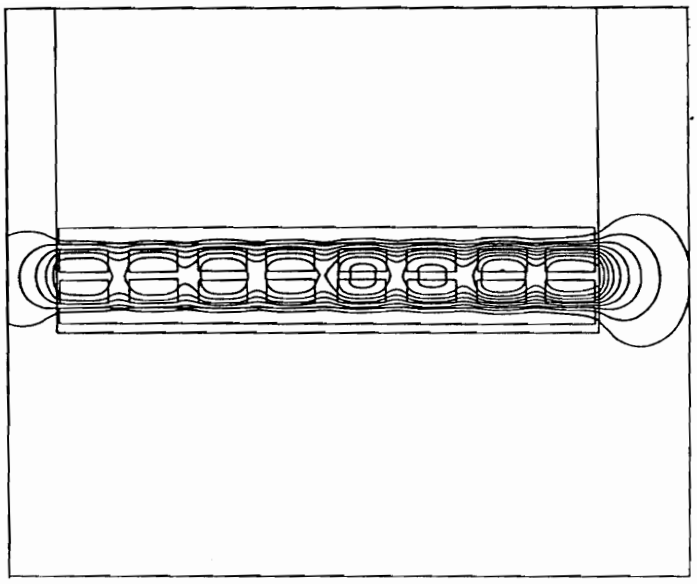

(a) Field distribution

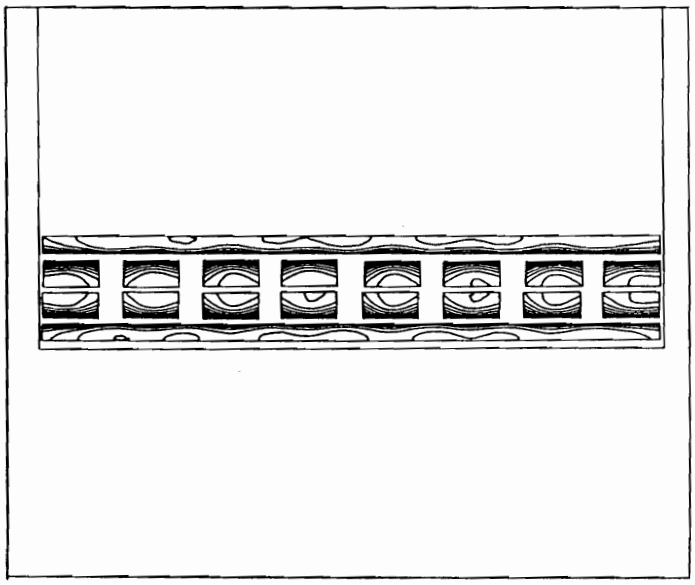

(b) Current density distribution

Fig. 3.18 The magnetic field and current distribution of the **S-P-P-S (case 4)** winding arrangement with a **printed-wire** primary at 300 kHz

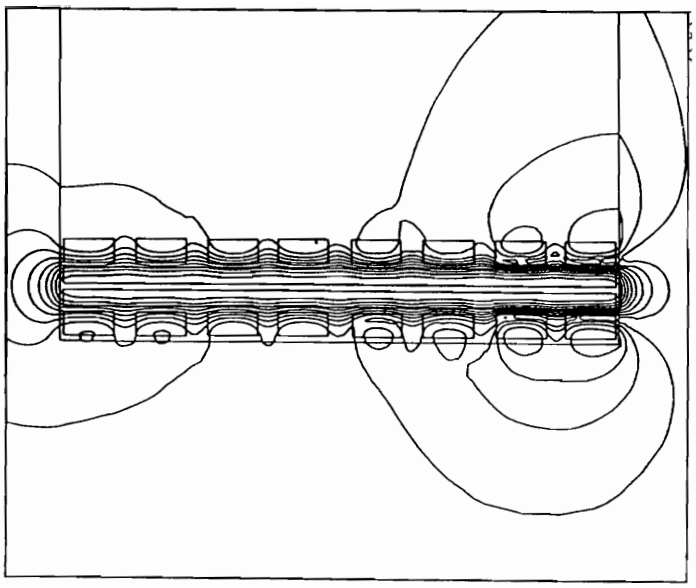

(a) Field distribution

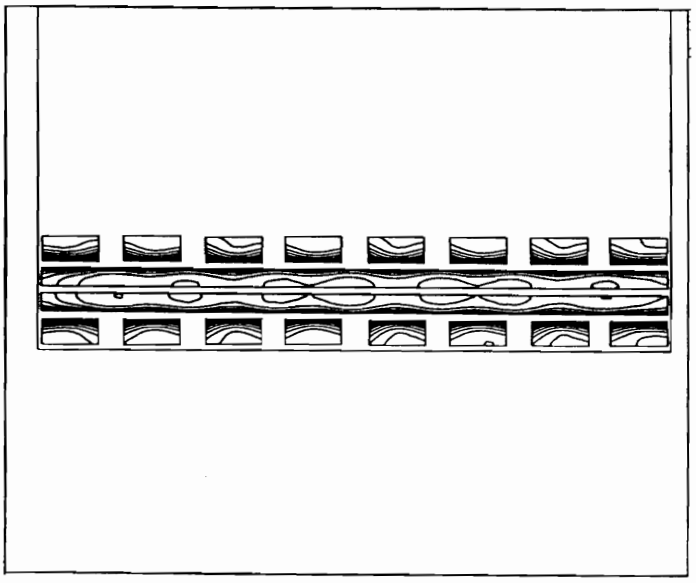

(b) Current density distribution

Fig. 3.19 The magnetic field and current distributions of the **P-S-S-P (case 5)** winding arrangement with a **printed-wire** primary at 300 kHz .

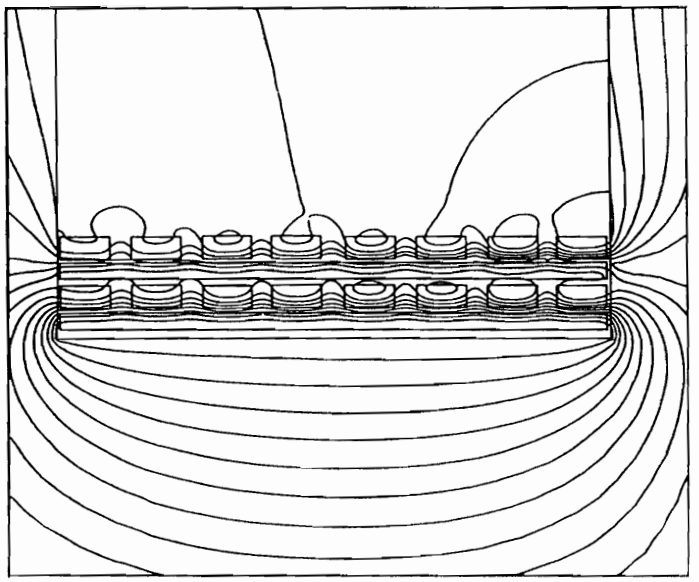

(a) Field distribution

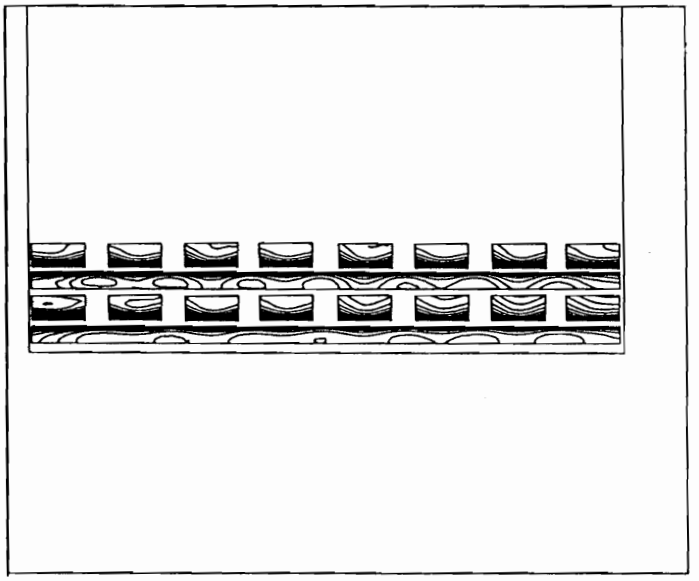

(b) Current density distribution

Fig. 3.20 The magnetic field and current distributions of the **P-S-P-S (case 6)** winding arrangement with a **printed-wire** primary at 300 kHz .

Figure 3.21 gives the plot of ac resistance and leakage inductance of the three winding arrangements with a printed-wire primary at different frequencies. Again, it shows that the one-dimensional method is not accurate enough to predict the characteristics of different winding arrangements.

Solid wire, printed-wire vs. Litz wire

Figure 3.22 illustrates the current density distribution in transformers with a solid wire primary, printed-wire primary, and a Litz wire primary for the S-P-S-P winding arrangement. It shows that the maximum current density appears at the interface region, which means that the current is crowded at this region. In the solid wire case, less area has been used for carrying the high-frequency current, and the current density changes from 0.9 to 4.7. In the printed-wire primary, more conductor area has been used to carry high-frequency current, and current density changes from 0.9 to 3.7. The current distribution in the solid wire primary is more crowded than that in the printed-wire primary. Since the ac-resistance is proportional to the square of current, the primary resistance in the solid wire case is higher than that in the printed-wire case. When a transformer is built by using Litz wire, the current distribution in Litz wire is uniform because of the special construction. Therefore, the Litz wire primary has lower resistance compared to the solid wire primary. and Litz wire primary. And in the secondary winding, the current densities for the three cases are almost the same, as shown in Fig 3.22. It means that the three cases have the same secondary winding resistances. As a result, the

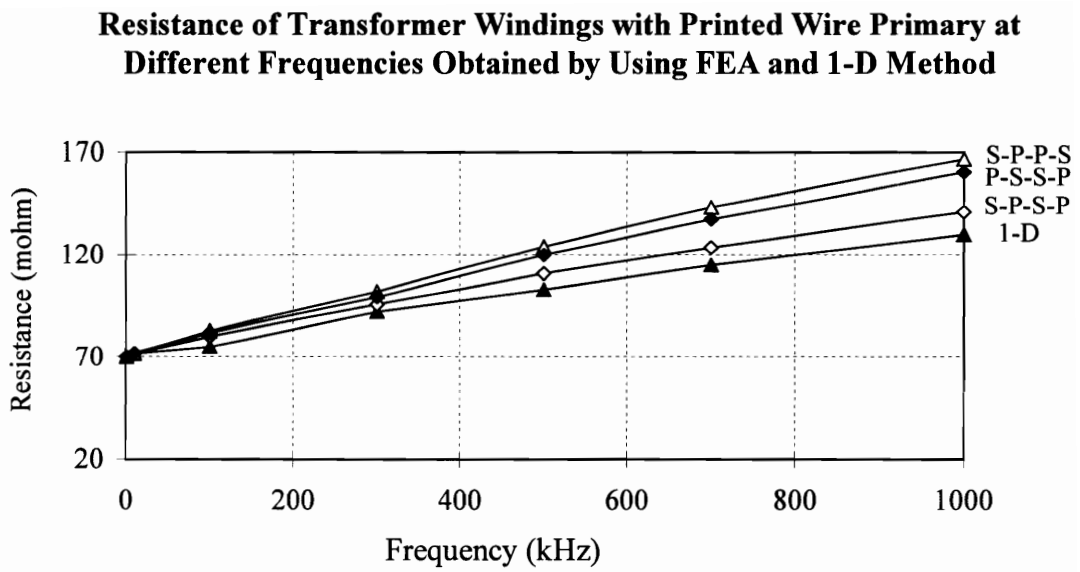

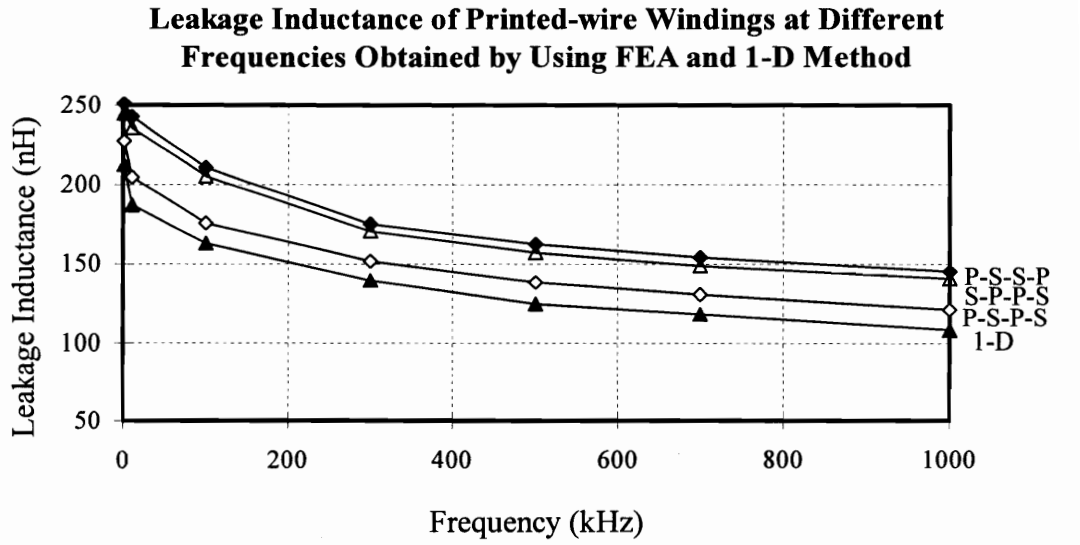

Fig. 3.21 The plot of ac-resistance and leakage inductance of the S-P-P-S, P-S-S-P, and S-P-S-P winding arrangements with a **printed-wire primary** when frequency ranges from DC to 1 MHz. The 1-D method fails to show the difference among these three winding arrangements, and consequently predicts a lower resistance. The FEA method shows the exact results.

transformer winding with the Litz wire primary has the lowest ac-resistance compared to the transformers with printed-wire primary and solid wire primary. And the transformer with the printed-wire primary has a lower ac-resistance than the equivalent winding with the solid wire primary.

Because current crowds at the interface region, the larger interface region in the printed-wire case allows a better cancellation of the electromagnetic field produced by the primary and secondary windings. As a result, the transformer with the printed-wire has the lowest leakage field intensity in the transformer window area. Figure 3.23 compares the magnitude of the electromagnetic field intensity at lines AB and A'B' in the window area of the transformers with the solid wire primary, printed-wire primary and Litz wire primary with S-P-S-P winding arrangements. Comparing the three cases, we can see that the transformer with the printed-wire primary has the lowest magnetic field intensity along the lines AB and A'B', and the transformer with the Litz wire primary has the highest magnetic field intensity. Since the energy stored in the leakage field is proportional to the square of the magnetic field, the transformer with the printed-wire primary (case 6) appears to have the lowest leakage inductance (151.64 nH) compared to the equivalent winding structure with the solid wire primary and Litz wire primary.

As a result, the transformer with the printed-wire primary has the lowest leakage inductance, and the transformer with the Litz wire primary has the lowest ac-resistance for the same winding arrangement. The transformers that are built with different wire

types are suitable for different applications. For hard-switching application, the leakage inductance will increase the voltage stress and current stress of semiconductor devices and increase the switching loss. In such a case, a low leakage inductance transformer is desired. Therefore, the printed-wire transformer is the best choice for the hard-switching application. However, for soft-switching application (e.g. FB-ZVS-PWM converter), the transformer leakage inductance is used to resonate with a capacitor to realize ZVS. Therefore, a low ac-resistance transformer is desired in order to increase the circuit efficiency. The best wire-foil arrangement is the S-P-S-P winding structure with the Litz wire primary, which has the lowest resistance. However, for the purpose of low-profile, it is necessary to build the wire into a spiral pattern that does not lend itself to automated planar manufacturing methods. The all-foil arrangement shown in next section is more manufacturable than the spiral winding configuration.

Current Distribution in Solid Wire P1 and Copper Foil S1

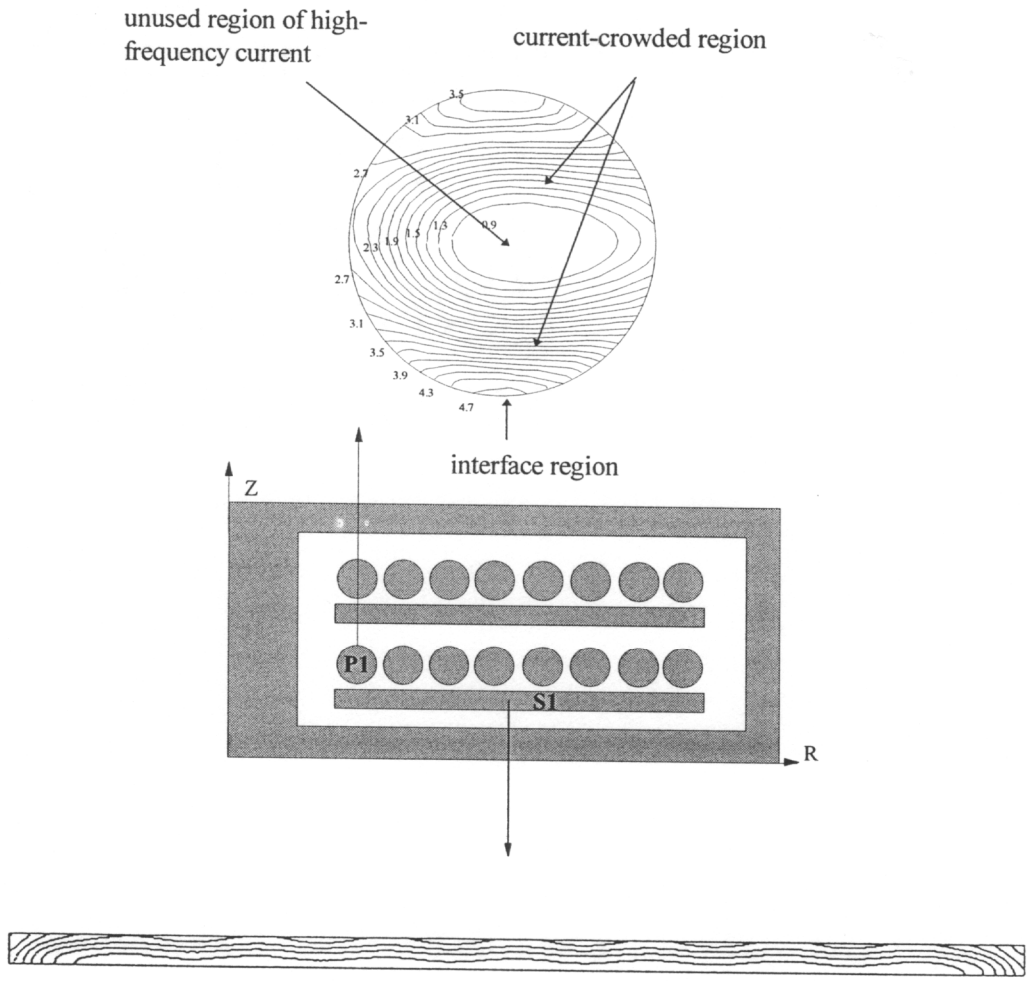

Fig. 3.22(a) Current density distribution in primary and secondary with a solid wire primary. It shows that the current is crowded at the interface region, and current density changes from 0.9 to 4.7. Also, a larger unused area for high-frequency current and a more uneven current density distribution than that in the printed-wire case (as shown in Fig. 3.22(b)) can be observed.

Current Distribution in Printed-wire P1 and Copper Foil S1

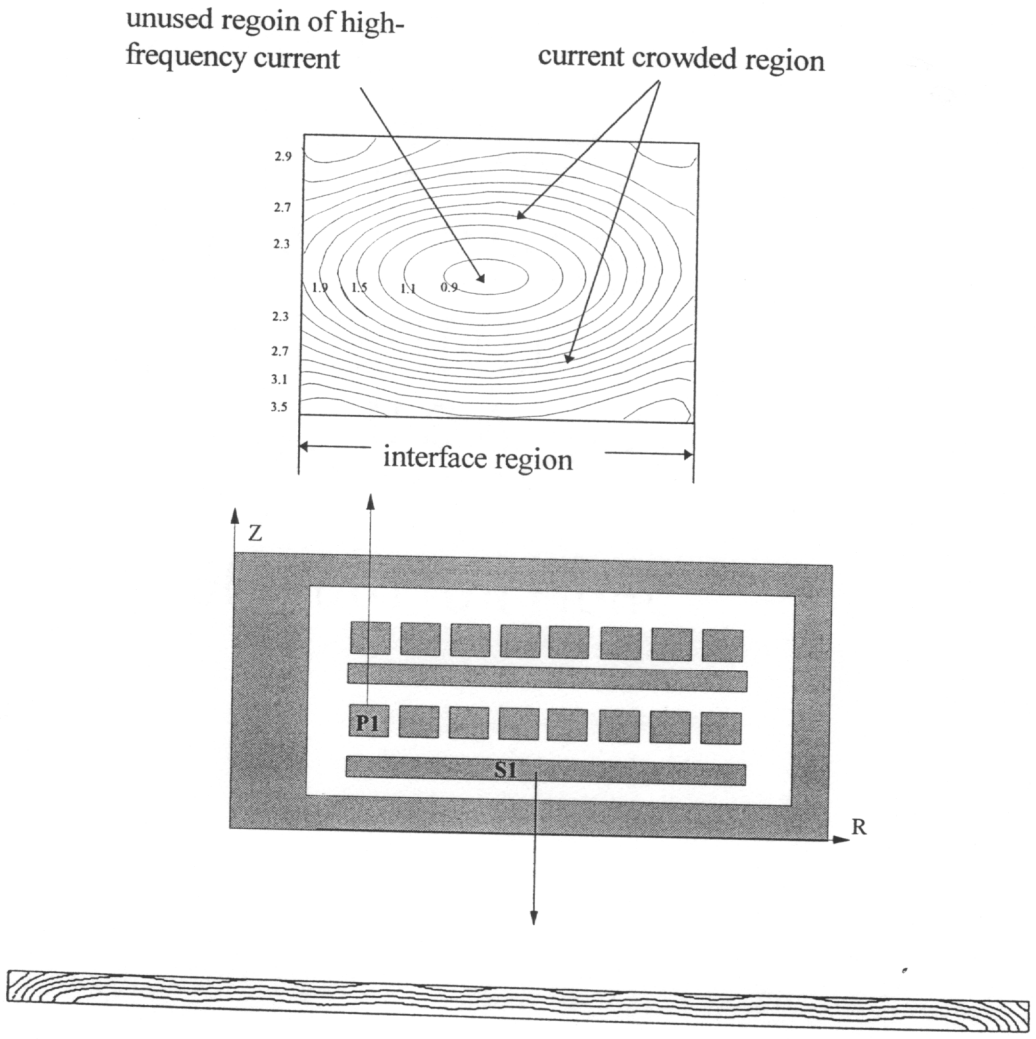

Fig. 3.22(b) Current density distribution in primary and secondary with a printed-wire primary . It is noted that the current is crowded at the interface region, and current density changes from 0.9 to 3.5.

Current Distribution in Litz Wire P1 and Copper Foil S1

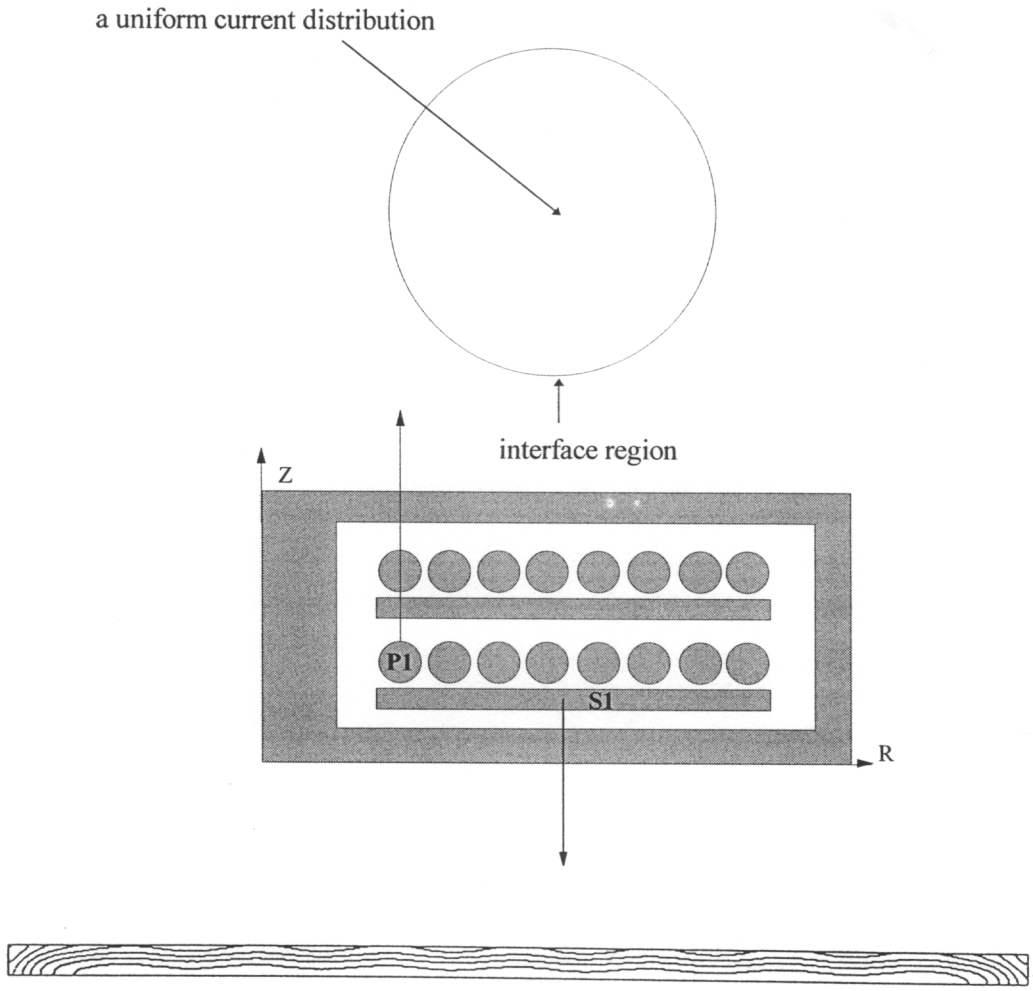

Fig. 3.22(c) Current density distribution in primary and secondary with a Litz wire winding . It is noted that the current is uniformly distributed. The current density is 1.56 A/mm^2.

Magnitude of Magnetic Field Intensity in P-S-P-S Winding Arrangement

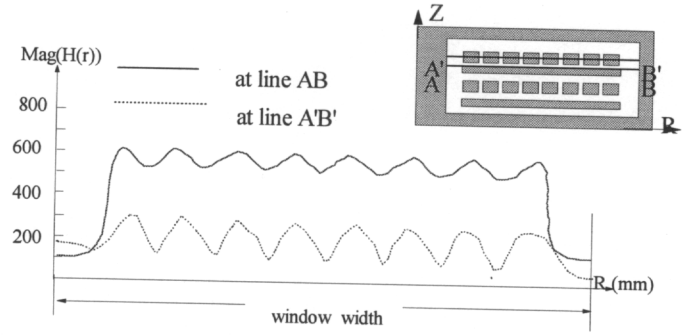

(a) Printed -wire primary.

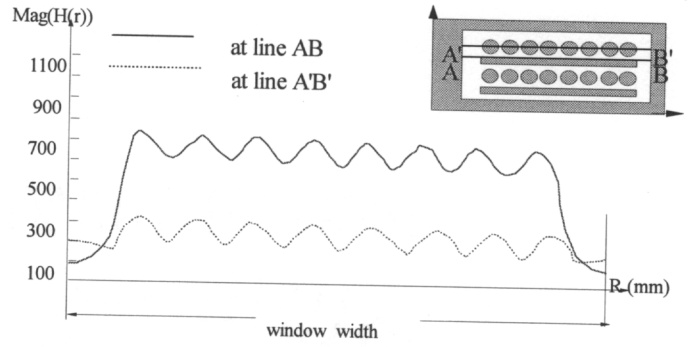

(b) Solid wire primary.

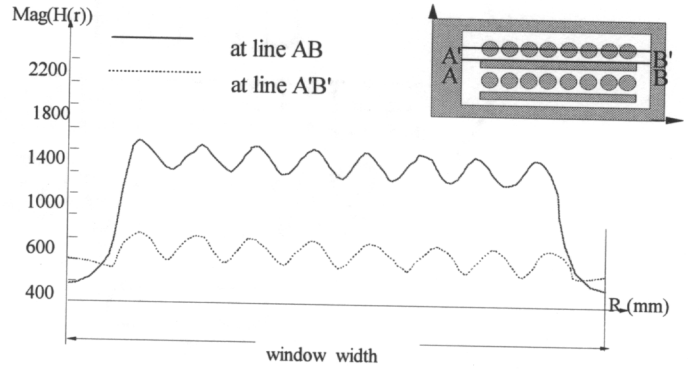

(C) Litz wire primary.

Fig. 3.23 Comparison of field intensities at AB and A'B' in the window area of the interleaving structure S-P-S-P with the printed-wire primary and solid wire primary.

3.2.2 Copper Foil Winding Patterns

Case 7 The electromagnetic field and current distribution of the 4:1 transformer with the winding arrangement Case 7 are shown in Fig. 3.24. Obviously, the current distribution in this case is much more uniform than that of the previous cases, because of the increasing of the interface region between primary and secondary windings. However, some of the leakage field is around the wire, which causes eddy currents in it. This winding arrangement has a 51.3 mΩ ac-resistance and a 113 nH leakage inductance.

Case 8 Figure 3.25 shows the electromagnetic field and current distributions of the 8-layer winding structure. This winding arrangement has the largest interface region between the primary and the secondary, which allows a very good cancellation of the electromagnetic field produced by the primary and the secondary. As shown in Fig. 3.26, the leakage field is much lower compared to the several previous cases. At the same time, the electromagnetic field between layers is almost tangential to the surface of the foil which extends mostly horizontally across the window width, which results in a very uniform current distribution. The 8-layer interleaved winding structure, therefore, has the lowest ac-resistance (39 mΩ) and leakage inductance (81 nH) of all the other cases studied above.

Figure 3.27 gives the plot of ac resistance and leakage inductance of the winding arrangements in cases 7 and 8 at different frequencies. At all frequencies shown, the 8-

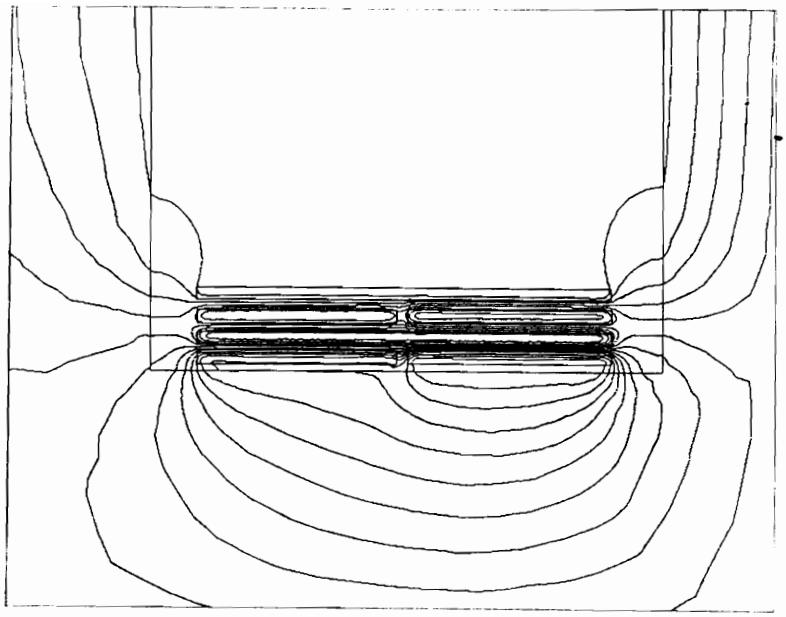

(a) Field distribution

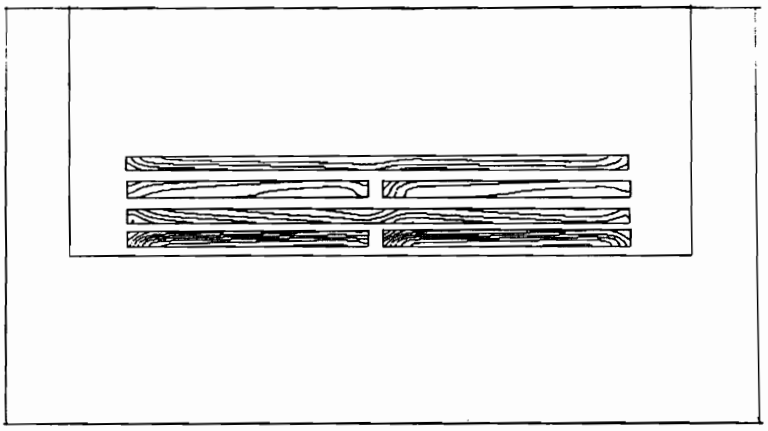

(b) Current density distribution

Fig. 3.24 The magnetic field and current distributions of **Case 7** at 500 kHz .

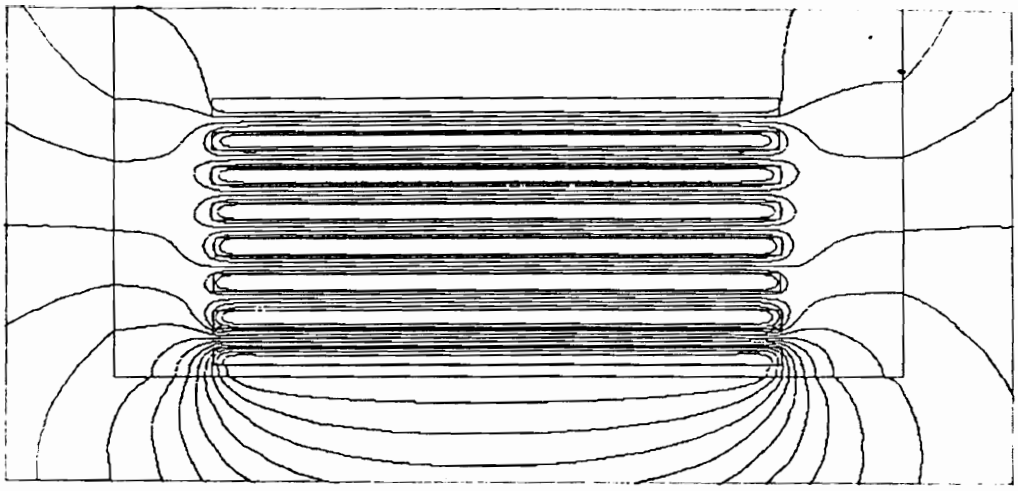

(a) Field distribution

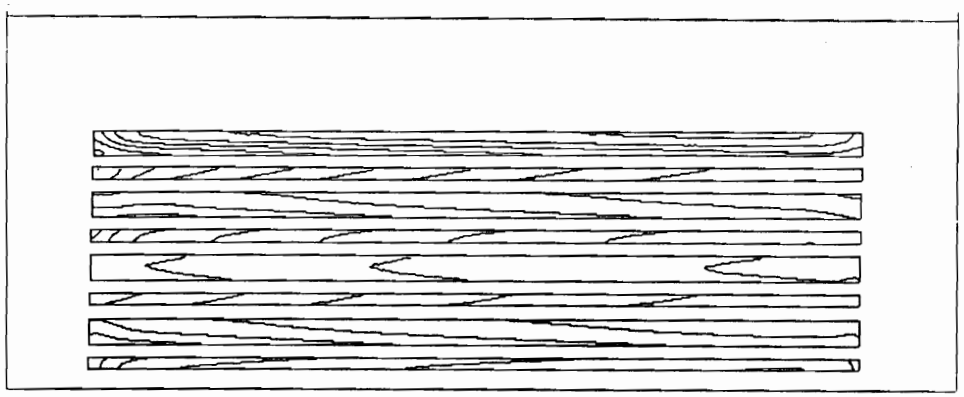

(b) Current density distribution

Fig. 3.25 The magnetic field current density distributions of **Case 8** at 500 kHz .

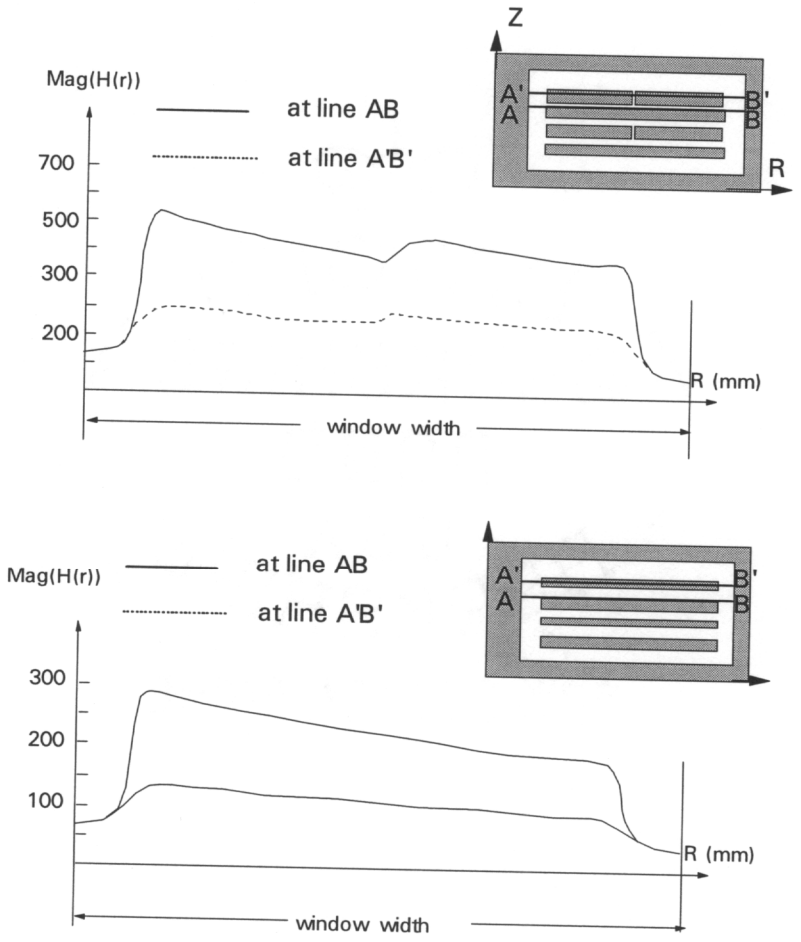

Fig. 3.26 Magnitude of field intensity in transformer winding. In Case 8, the field intensity is much lower than that of Case 7. It results in a lower leakage inductance.

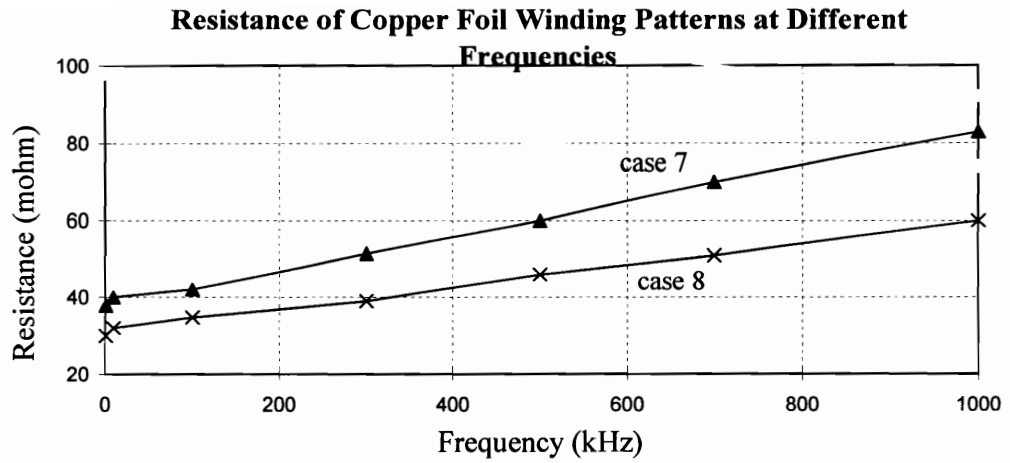

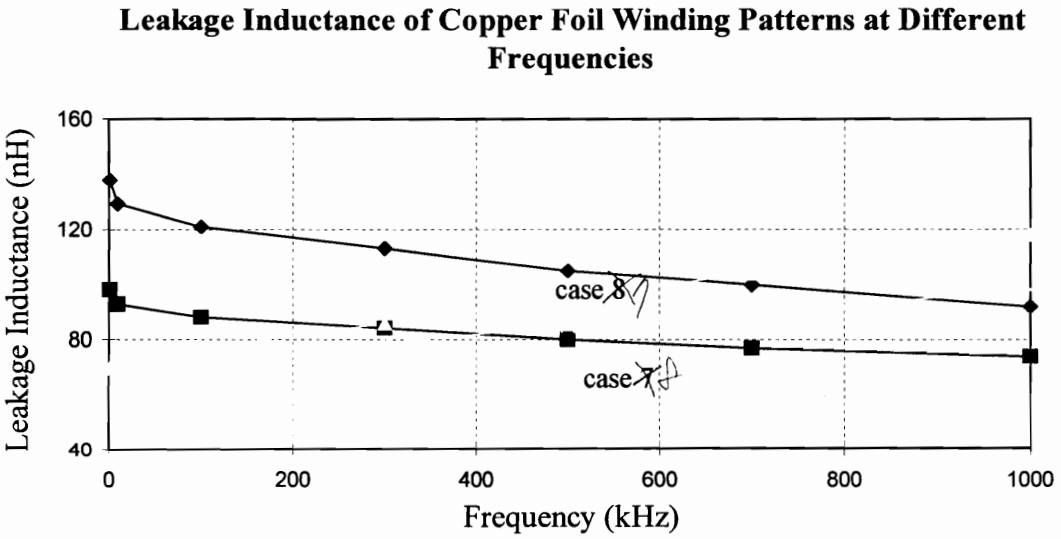

Fig. 3.27 The plot of ac-resistance and leakage inductance of Cases 7 and 8 when frequency ranges from DC to 1 MHz.

layer copper foil interleaving winding arrangement has a lower ac-resistance and leakage inductance than those of the 4-layer copper foil winding structures.

3.3 Summary

Table 3.2 gives the ac-resistance, leakage inductance, and ac-resistance factor for the eight winding arrangements at 300 kHz. It shows that the all-foil winding structure has the lowest ac resistance and leakage inductance. It is most suitable for low-profile transformer applications.

2-D FEA is used to visualize the high frequency magnetic field and current distribution, and to quantify high frequency power dissipation and energy storage by taking high frequency skin effect, proximity effect, and edge effect into account. The regions of high leakage fields and strong current crowding are clearly displayed. The characteristics of different winding arrangements with different wire types (solid wire, Litz wire, and printed wire) are accurately predicted.

FEA results show that the interleaving structure has a lower ac-resistance and leakage inductance than those of the sandwiched structures, regardless of which type of wire is used. For the same winding arrangement, the transformer with a Litz wire primary has the lowest ac-resistance, and the transformer with printed-wire has the lowest leakage

inductance. The fully interleaving copper foil structure has the lowest ac-resistance and leakage inductance compared to any other winding arrangements discussed, because of the largest interface region between primary and secondary windings.

Table 3.2 Comparison of ac resistance and leakage inductance for the eight winding arrangements.

	ac resistance (mΩ)	**leakage inductance (nH)**
Case 1 **S-P-P-S** with **solid** wire primary	107.35	200.5
Case 2 **P-S-S-P** with **solid** wire primary	102.9	206.5
Case 3 **P-S-P-S** with **solid** wire primary	96.6	178.4
Case 4 **S-P-P-S** with **printed** wire primary	102.3	168.4
Case 5 **P-S-S-P** with **printed** wire primary	98.2	175.5
Case 6 **P-S-P-S** with **printed** wire primary	92.7	151.6
Case 7 **P-S-P-S** with **foil winding** structure	51.3	113.7
Case 8 **8 layer all foil structure**	39.2	84.2

Chapter 4

Minimum Volume Design for Low-Profile Transformers

The most commonly used method of transformer design is using the relationships between transformer "Area Product" *Ap* and volume *Vc*, between *Ap* and surface area *At*, and between *Ap* and weight *Wt* for various core types. This method yields a simplified and standard procedure for transformer design. By using these relationships, it is possible to design a transformer of lesser weight and smaller volume, or to optimize efficiency without going through a cut and try design procedure [B21]. In addition to using the "Area Product", the constant transformer aspect ratio is another commonly used assumption in conventional transformer design. With this assumption, a nonlinear

mathematical optimization technique, such as Augmented Lagrange Penalty Function Technique (ALAG) is used to minimize transformer volume or weight [B8, B9, B18, B19]. These methods have been extensively used to optimize high-frequency transformer performance. However, a low-profile transformer core is custom designed. The aspect ratio changes from one core to another. Therefore, the assumption of the constant aspect ratio is not valid, and the relationships between area product and volume for standard transformers do not hold for low-profile transformers. The tools developed for conventional transformer design cannot be extended to low-profile transformer design.

For low-profile transformer design, K. Ngo [B1, B3] pointed out that height reduction may degrade transformer power density (assuming that efficiency is kept constant while the height is reduced). A. Goldberg [B2] analyzed the relationship between footprint and planar winding copper loss. However, both of them used the dc-resistance to predict transformer winding loss by limiting winding thickness to the skin depth. Therefore, their design approaches are inadequate for application to optimizing new generation transformers, the low-profile transformers.

In order to design a low-profile transformer that has a maximum power density and meets both the electrical and thermal specifications, and to clarify trade-offs between core loss and winding loss, and trade-offs between profile and footprint, a new methodology and **a** new design tool for low-profile transformer optimization need to be developed. Therefore, the effort of this chapter is to develop a new design tool to achieve

the maximum power density in low-profile transformers. More specifically, the focus is on the determination of the minimum transformer volume for a given power level and output voltage based on only one fundamental constraint, i.e. the temperature rise.

The design of a low-profile transformer with the maximum power density is an iterative process, as shown in Fig. 4.1. The whole process includes two design procedures: general design and fine tuning. The design starts from the transformer geometry selection. Once the transformer geometry parameters are decided, the transformer winding loss, core loss, and temperature rise are evaluated. The transformer loss and temperature rise are calculated by using winding loss model derived in Chapter 2 and the core loss and thermal model derived in section 4.2. If the transformer geometry parameters result in a minimum volume and meet the design specifications: thermal constraint, the design procedure one -- the general design -- is completed. If the design specifications are not met, the geometry parameters have to be reselected until a transformer geometry that meets the all design specifications is found. The second procedure -- fine tuning -- is optional; in this procedure, the 2-dimensional winding loss calculation is applied to calculate transformer winding loss in order to obtain a more accurate design.

In order to facilitate the design process, low-profile transformer models, including the models of winding loss, core loss, and temperature rise, are set up in terms of structural parameters. Then a number of equations that reveal the relationships among

geometry parameters are derived. From these equations, the key parameters that determine transformer geometry and power dissipation are identified. Due to the complex relationships between the power dissipation and key parameters, the process of identification of the key parameters that results in the maximum power density needs to be automated. A design tool to identify the key parameters is based on a nonlinear optimization technique. Consequently, the maximum achievable power density and the required winding structure will be determined, along with the optimum operating frequency and core geometry. It should be noted that this particular design algorithm is developed for low-profile transformers. Since the availability of low-profile cores and the choice of core geometries are very limited, this design will not be confined within commercially available cores. The outcome of the design will specify a core with certain dimensions and the window aspect ratio deemed optimal for achieving a minimum volume design.

The proposed design procedures are implemented as MATLAB optimization program, and its applicability is illustrated through several examples. The calculation results are experimentally verified.

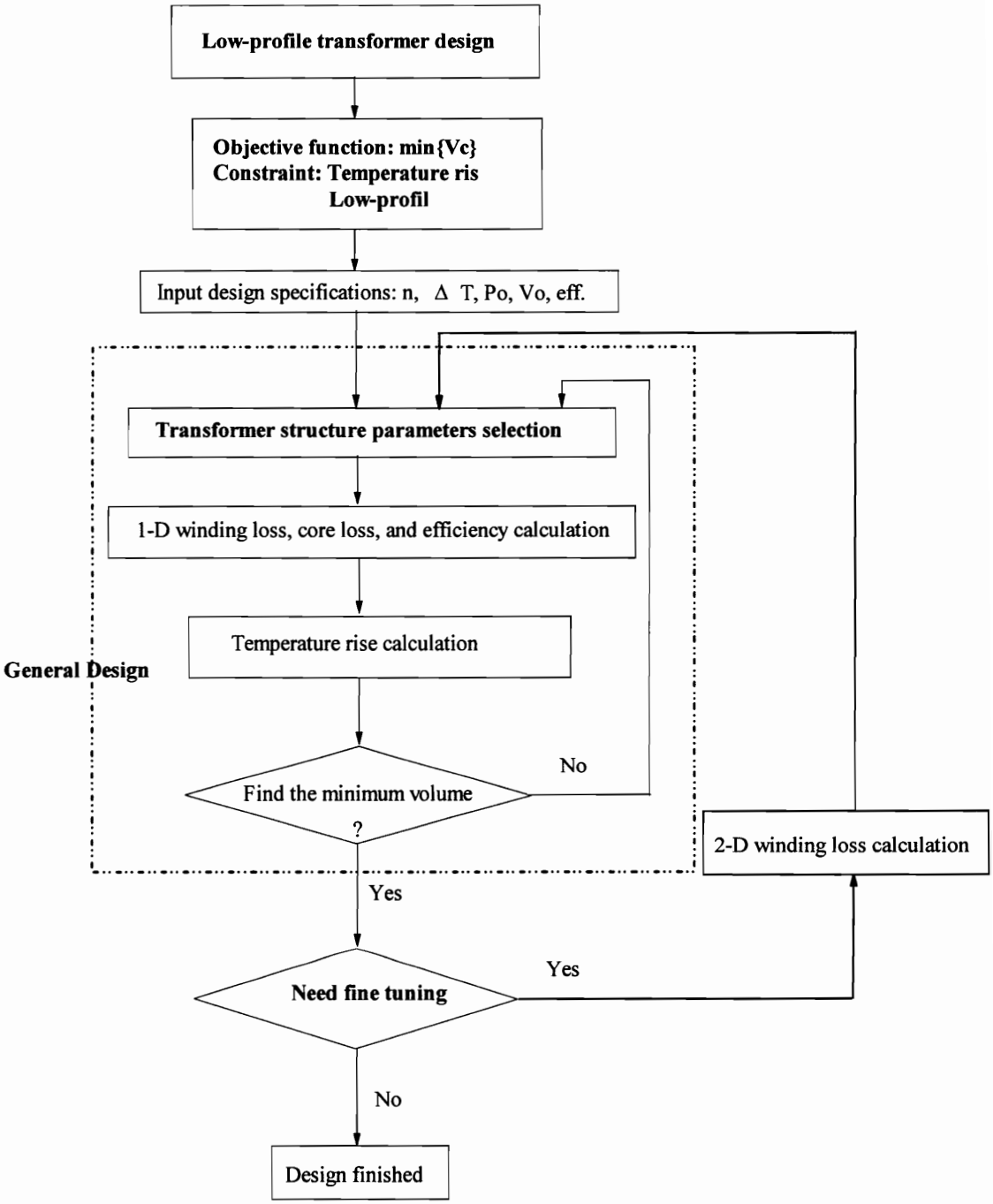

Fig. 4.1 The design procedure for a low-profile transformer. The design is an iterative process.

4.1 Low-Profile Transformer Core Loss Model

The core loss is considered to be piece-wise uniformly distributed in each section and calculated by using the empirical method. In general, any kind of core consists of a "center post", an "outer shell", a "top plate", and a "bottom plate". So, the total loss will be the sum of losses of the four parts.

At a given frequency, the core loss density is related to the peak flux density in the core and operating frequency by

$$P_c = K \cdot f^{\alpha} \cdot B_c^{\beta}, \tag{4.1}$$

where K is the core loss coefficient, while α and β are the core loss exponents, extracted from core loss data, and B_c is the flux density in the core, which is decided by

$$B_c = \frac{n \cdot V_0 \cdot D}{f \cdot N_p \cdot A_e}, \tag{4.2}$$

where Ae is the effective cross-sectional area of core.

Figure 4.2 shows the different geometries of E-core. Since the cross-sectional areas of center post, top or bottom plate, and outer shell are different, the core loss at center post, top or bottom plate, and outer shell can be calculated by

$$P_{cC} = P_C \cdot A_{e1} \cdot Ht, \tag{4.3}$$

$$P_{ct} = P_c \cdot A_{e2} \cdot b_{win}, \tag{4.4}$$

$$P_{cs} = P_c \cdot A_{e3} \cdot H_t \ , \tag{4.5}$$

where A_{e1} is the cross-sectional area of center post, A_{e2} is the cross-sectional of top or bottom plate, A_{e3} is the cross-sectional area of outer shell, H_t is the transformer height, and b_{win} is the window width (as shown in Fig. 4.2).

The total core loss is

$$\begin{aligned} P_f &= P_{cc} + 2P_{ct} + P_{cs} \\ &= P_c A_{e1} H_t + 2 \cdot P_c A_{e2} b_{win} + P_c A_{e3} H_t \\ &= K f^{\alpha} \left(\frac{n V_o D}{N_p f} \right)^{\beta} \left[(H_t - 2H_p) \cdot (D_c \cdot D_w)^{1-\beta} + \right. \\ &\qquad \left. (A - 2H_p) \cdot (2H_p \cdot B)^{1-\beta} + Ht \cdot (2H_{p1} \cdot B)^{1-\beta} \right]. \end{aligned} \tag{4.6}$$

For a conventional E-core, the cross-sectional area is the same along its magnetic length; therefore

$$D_c = 2H_p = 2H_{p1}, \tag{4.7}$$

$$D_w = B, \tag{4.8}$$

and the total core is

$$
\begin{aligned}
P_f &= P_{cc} + 2P_{ct} + P_{cs} \\
&= Kf^{\alpha}\left(\frac{nV_oD}{N_pf}\right)^{\beta}\Big[(H_t - 2H_p)\cdot(D_c \cdot B)^{1-\beta} + \\
&\qquad (A - 2H_p)\cdot(2H_p \cdot B)^{1-\beta} + Ht\cdot(2H_p \cdot B)^{1-\beta}\Big] \\
&= Kf^{\alpha}\left(\frac{nV_oD}{N_pf}\right)^{\beta}(D_c \cdot B)^{1-\beta}\big[2H_t + A - 2D_c\big].
\end{aligned}
\tag{4.9}
$$

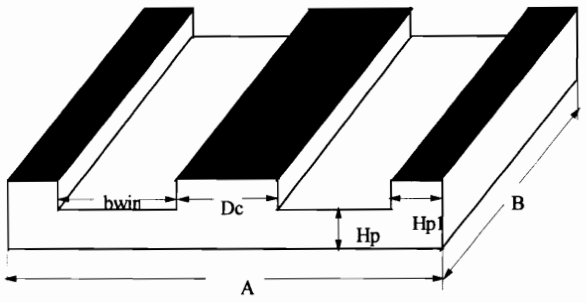

(a) $D_w = B, \quad H_p = H_{p1} = \dfrac{D_c}{2}$

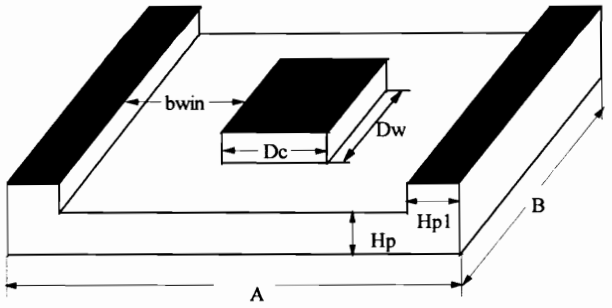

(b) $D_w \neq B, \quad H_p = H_{p1} = \dfrac{D_c}{2}$

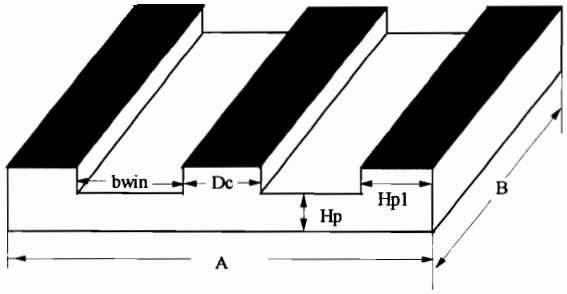

(c) $D_w = B, \quad H_p > H_{p1} = \frac{D_c}{2}$

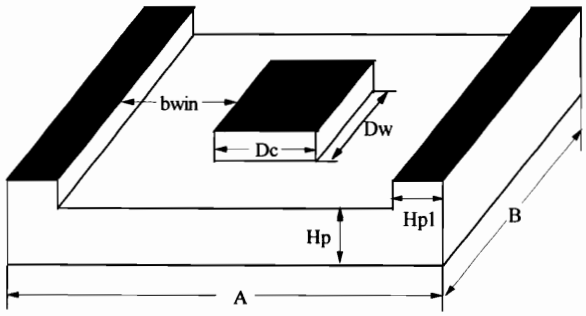

(d) $D_w < B, \quad H_p > H_{p1}$

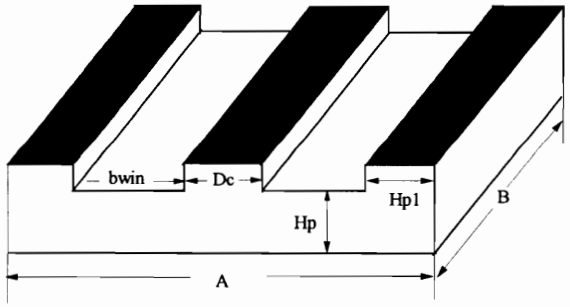

(e) $D_w = B, \quad H_p = H_{p1} > \frac{D_c}{2}$

Fig. 4.2 Different geometries of E-core transformer.

4.2 Low-Profile Transformer Thermal Model

4.2.1 Conductive Thermal Model

A low-profile transformer is typically packaged into a small "brick" type converter, where the entire circuit is encapsulated or sealed off from the external environment. In such a case, the transformer must be cooled by conduction to the case of the converter first, and then by convection from the heat sink via natural or forced air cooling. So, a purely conductive thermal model can be used for temperature rise calculation for a low-profile transformer. Figure 4.3(a) illustrates the heat transfer path of a low-profile transformer sits on a heat sink. All heat generated by the core and winding will be transferred to the heat sink.

According to the heat transfer path, the temperature rise can be evaluated by electrical and thermal analog technique, as shown in Fig. 4.3(b). The power dissipation in transformer is analogous to current; the temperature rise is analogous to voltage; and thermal resistance is analogous to electrical resistance. The thermal resistance can be calculated by

$$R_{th} = \frac{l_{th}}{A_{th}} \sigma_{th}, \tag{4.10}$$

where l_{th} is the length of the heat path, A_{th} is the cross-sectional area of the heat path, and σ_{th} is the thermal conductivity.

Since the thermal conductivity of the air is ten times smaller than that of the insulator and hundred times smaller than that of the conductor, it is reasonable to analyze the heat transfer characteristics for the core and windings separately. According to Fig. 4.3(b), the temperature rise from the heat sink to the top of core can be expressed as

$$\Delta T_{cor} = P_{ct1} \cdot R_{ct1} + (P_{ct1} + P_{cw}) \cdot R_{cw}, \tag{4.11}$$

and

$$\Delta T_{cor} = P_{ct2} \cdot R_{ct2} + (P_{ct2} + P_{cc}) \cdot R_{cc}, \tag{4.12}$$

where

$$P_{ct1} + P_{ct2} = P_{ct}, \tag{4.13}$$

$$R_{ct1} + R_{ct2} = R_{ct}, \tag{4.14}$$

and R_{ct} is the thermal resistance of the top plate, R_{cw} is the thermal resistance of the outer wall, R_{cc} is the thermal resistance of the center post, P_{ct} is the power dissipation of the top plate, P_{cw} is the power dissipation of the outer wall, P_{cc} is the power dissipation of the center post.

Combining equations (4.11), (4.12), (4.13), and (4.14), the P_{ct1} is

$$P_{ct1} = \frac{P_{ct}R_{ct2} + P_{ct}R_{cw} - P_{cw}R_{cw} + P_{cc}R_{cc}}{R_{ct} + R_{cc} + R_{cw}}, \tag{4.15}$$

Substituting (4.16) into (4.13),

$$\Delta T_{core} = (R_{ct1} + R_{cw}) \frac{P_{ct}R_{ct2} + P_{ct}R_{cw} + P_{cw}R_{cw} - P_{cc}R_{cc}}{R_{ct} + R_{cc} + R_{cw}} + R_{cw}P_{cw}$$

$$= (R_{ct1} + R_{cw}) \frac{P_{ct}(R_{ct} - R_{ct1}) + P_{ct}R_{cw} + P_{cw}R_{cw} - P_{cc}R_{cc}}{R_{ct} + R_{cc} + R_{cw}}$$

$$+R_{cw}P_{cw}. \tag{4.16}$$

For an EE-core transformer,

$R_{cC} = R_{cw}$,

$P_{cc} = P_{cw}$,

$R_{ct1} = R_{ct2} = \frac{R_{ct}}{2}$ and $P_{ct1} = P_{ct2} = \frac{P_{ct}}{2}$.

Therefore

$$\Delta T_{core} = (\frac{R_{ct}}{2} + R_{cw}) \cdot \frac{P_{ct}}{2} + R_{cw} \cdot P_{cw}, \tag{4.17}$$

where $R_{ct} = \frac{W_w + H_p}{\sigma_{thf} \cdot D_c \cdot B}$, and $R_{cc} = \frac{H_t}{\sigma_{thf} \cdot D_c \cdot B}$.

The maximum temperature difference between the hot spot of the winding and the heat sink:

$$\Delta T_w = (P_w + P_c) \frac{H_p}{2W_w B} \sigma_{thf} + P_w \frac{\sigma_{thi} t_i + \sigma_{thc} t_c}{2W_w B}, \tag{4.18}$$

where σ_{thi} is the thermal resistivity of the insulation, σ_{thc} is the thermal resistivity of the conductor, t_i is the total thickness of the insulation layers, and t_c is the total thickness of the conductor layers.

4.2.2 Experimental Verification

To check the accuracy of the thermal model, calculated values of the temperature rise of winding and core are compared with the measured values. The measured data were obtained in circuit tests performed on two transformers by using 2166A 10 Channel Digital Thermometer. The first test transformer is a multilayer PCB transformer in a 300-W 5-V-output active-clamp forward converter. The transformer core geometry and winding arrangement for testing are shown in Fig. 4.4. The power stage of the converter was assembled on a copper-clad aluminum substrate that was sitting on a heat sink with a layer of thermally conductive paste placed at the interface between the substrate and the heat sink. The power transformer was attached to the substrate by means of thermal conductive epoxy to provide low thermal resistance from the core to the substrate. The windings were fitted in the core with a layer of thermally conductive paste placed at the interface between the winding and the core. In order to ensure conductive heat transfer and prevent convective and radiative heat transfer in the transformer, the power stage was covered by a plastic box during the testing. Thermocouples were attached to the core, winding, and heat sink to measure the temperature rise of the transformer. All the results were obtained after the converter reached thermal equilibrium.

As shown in Fig. 4.4, the average value of T1 and T2 is the temperature of the transformer winding, the average value of T3 and T4 is the temperature of the core, and the average value of T5 and T6 is the temperature of the heat sink. Table 4.1(a) shows the results of thermal measurements at different power levels. The temperature difference between the winding and heat sink is the temperature rise of the winding, and the temperature difference between the core and heat sink is the temperature rise of the core. Table 4.1(b) shows the comparison of the measurement results and prediction results. Thermal resistivity is 0.0026 °C m /W for copper, 0.25 °C m /W for ferrite, 1.14 °C m /W for thermal glue, and 0.1 °C m /W for aluminum substrate.

The secondary transformer for testing is shown in Fig. 4.5. This is a 5-layer transformer with two pieces of double-side PCB for the primary and one-layer copper foil for the secondary. Each primary layer is a two-turn spiral winding. Two-layer primary windings at the same PCB are connected in series to construct a four-turn primary. The two pieces of PCB are externally parallel. The transformer was tested in a 100-W 3.3-V-output active-clamp forward converter. The transformer was attached to the heat sink by means of double adhesive thermal conduction and electrical insulation tape, to provide low thermal resistance and electrical isolation between the core and the heat sink. The windings were fitted in the core with a layer of thermally conductive paste placed at the interface between the winding and the core. The power stage was covered by a plastic box during the testing. Thermocouples were attached to the core, winding, and heat sink to

measure the temperature rise of the transformer. All the results were obtained after the converter reached thermal equilibrium. Table 4.2 shows the testing results at different power levels and the comparison of the measured results with predicted results.

As Tables 4.1(b) and 4.2(b) indicate, the prediction of the temperature rise agrees well with the measured values, although the predicted values are consistently a little higher than the measured values. The difference between the prediction and measurement results can be attributed to the purely conductive assumption for a theoretical model. In a purely conductive thermal model, there is no air flow. In practice, however, the air is circulating; the hot air goes up, while the cool air goes down because of the difference temperature between the transformer and the air that surrounds it, although the power stage that contains the transformer is sealed from the external environment.

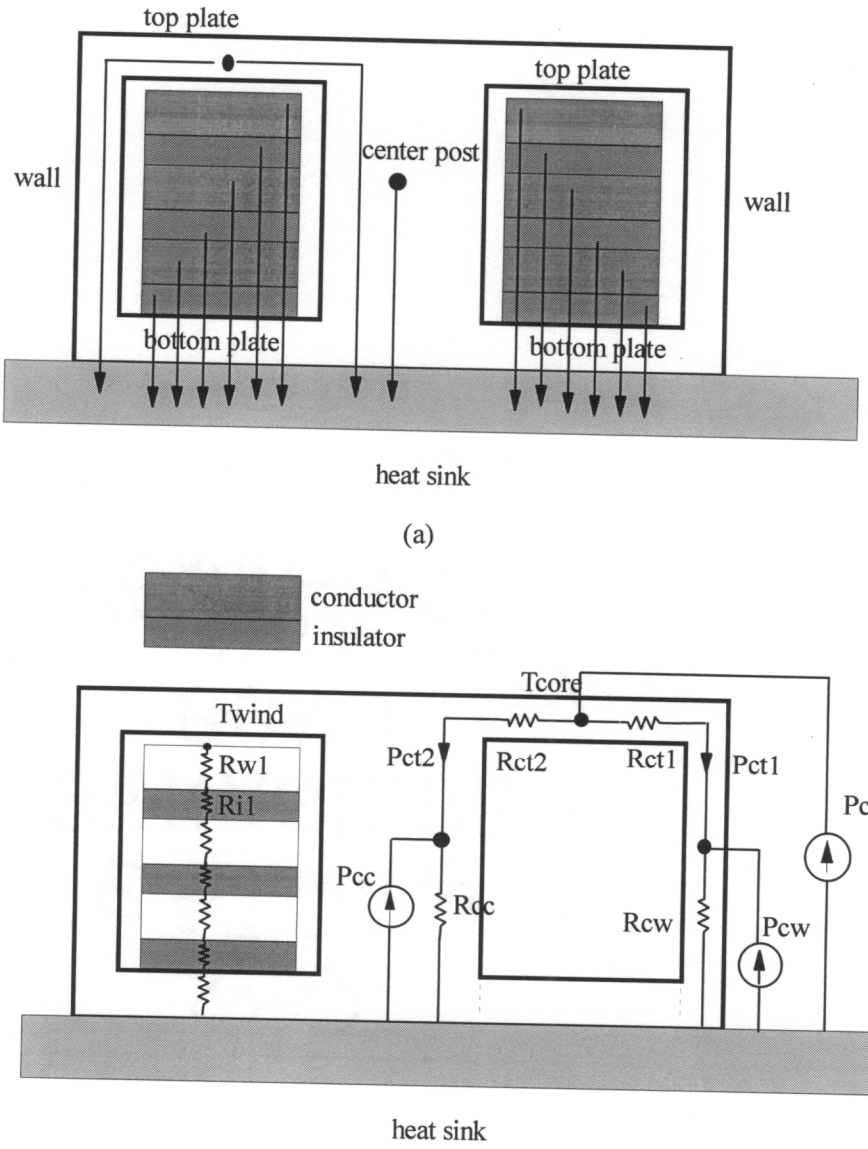

Fig. 4.3 (a) Heat transfer path in a low-profile transformer. (b) Electrical and thermal analog technique for temperature rise calculation.

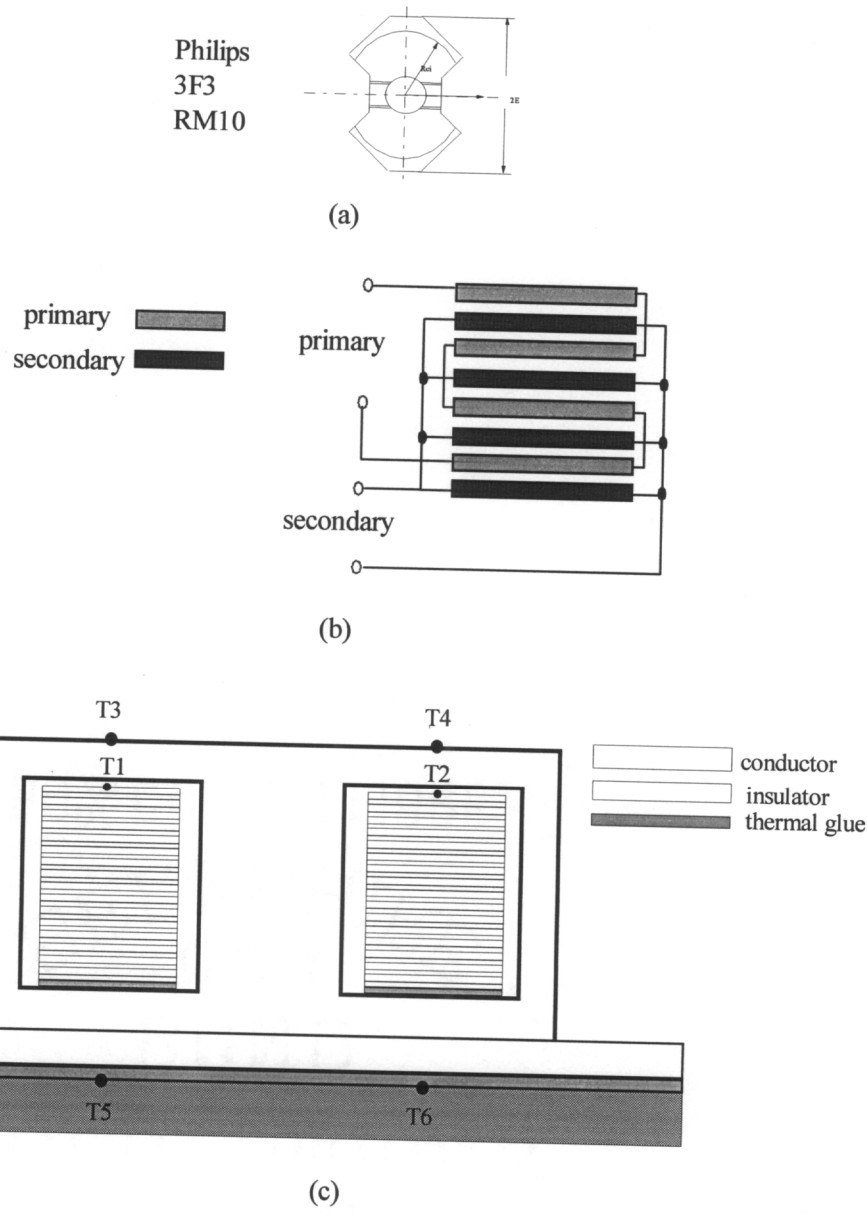

Fig. 4.4 Transformer core geometry and winding arrangement for testing. (a) transformer core geometry. (b) a 4:1 transformer winding structure, four-turn primary and one-turn secondary; the conductor thickness for each winding layer is 0.071 mm, the winding width is 4.9 mm, and insulator thickness is 1.016 mm. (c) test points for winding, core, and heat sink. The thickness of substrate is 2.5 mm; the typical thickness of thermal glue is 2 mil.

Table 4.1 (a) The measurements temperature of winding, core and heat sink at different power levels.

Power Level	Core (°C)	Winding (°C)	Heat sink (°C)
P_o = 200 W	79	82	47
P_o = 300 W	110	116	69

Table 4.1(b) Comparison of measured and predicted results of temperature rise of transformer core and winding.

	P_o = 200 W		P_o = 300 W	
	Core (°C)	Winding(°C)	Core(°C)	Winding(°C)
predicted	32	35	45.1	47.5
measured	31	33	41	47

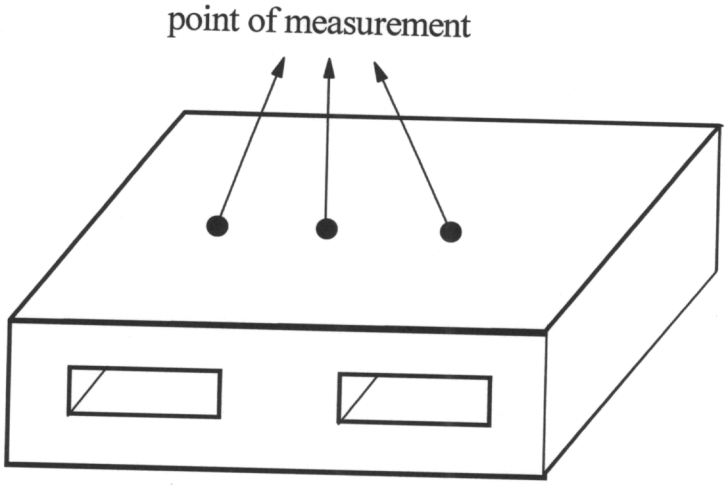

(a)

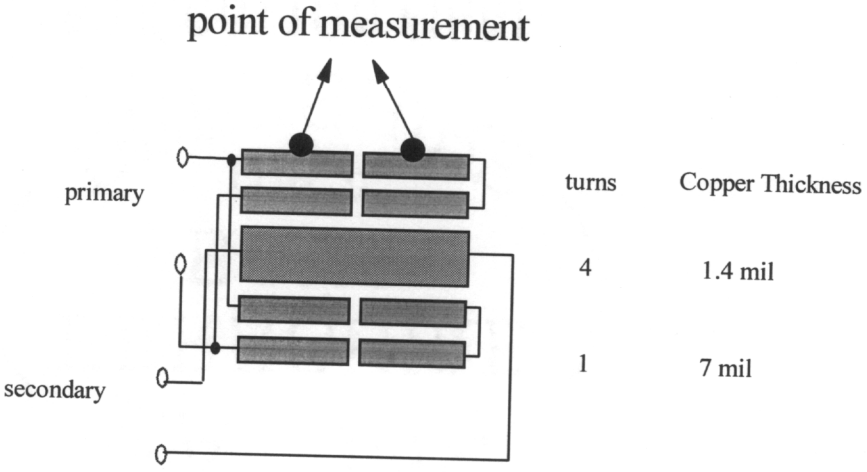

(b)

Fig. 4.5 Transformer core geometry and winding arrangement for testing. (a) transformer core geometry. (b) a 4:1 transformer winding structure, four-turn primary and one-turn secondary; the primary conductor thickness is 1.4 mil, the secondary conductor thickness is 7 mil, and insulator thickness is 2 mil.

Table 4.2(a) The measurements of temperature of winding, core and heat sink at different power levels.

Power Level	Core (°C)	Winding (°C)	Heat sink (°C)
P_o = 60 W	73	74	50
P_o = 100 W	106	107.5	70

Table 4.2(b) Comparison of measured and predicted results of temperature rise of transformer core and winding.

	P_o = 60 W		P_o = 100 W	
	Core (°C)	Winding(°C)	Core(°C)	Winding(°C)
predicted	25.2	27.1	38.8	39.7
measured	24	24	36	37.5

4.3 *Defining Core/Winding Geometry*

In general, transformers with different shapes of cores will have different volumes for the same design. Each shape of core has its own geometry parameters and unique relations among these parameters. An E-core transformer is selected to be an example to show the derivation of design equations. The design equations that are used to find the minimum transformer volume in the optimization program are derived.

As shown in Fig. 4.6, the top and bottom plates thickness H_p of an E-core transformer is determined by transformer height H_t and window height H_w:

$$H_p = \frac{H_t - H_w}{2}, \tag{4.19}$$

The core window width b_{win} can be determined by

$$\begin{aligned} b_{win} &= \frac{A - D_c - 2 \cdot H_p}{2} \\ &= \frac{A - D_c - H_t + H_w}{2}, \end{aligned} \tag{4.20}$$

where A is the core width, and D_c is the center post width.

As a result, the center post depth D_w can be computed by:

$$D_w = \frac{V_c}{H_t \cdot A} - 2b_{win}$$

$$= \frac{V_c}{H_t \cdot A} - (A - D_c - H_t + H_w). \qquad \text{if } b_{win} \geq \frac{B - D_w}{2}, \tag{4.21}$$

where V_c is transformer volume.

The core depth B is

$$\begin{aligned} B &= \frac{D_w \cdot D_c}{2H_p} \\ &= \frac{D_c}{2H_p} \cdot \left(\frac{V_c}{H_t \cdot A} - (A - D_c - H_t + H_w) \right) \end{aligned} \tag{4.22}$$

From equations (4.20), (4.21), and (4.22), we can see that all core geometry parameters can be related to core width A, transformer height H_t, window height H_w, center post width D_c, and transformer volume V_c. Once these parameters are given, the core geometry is decided. These parameters are named **core geometry parameters**.

The winding geometry is decided by conductor width:

$$\begin{aligned} W_{cp} &= (b_{win} - C_s - N_{sp} \cdot C_r) / N_{sp} \\ &= (\frac{A}{2} - H_t + H_w - C_s - N_{sp} \cdot C_r) / N_{sp} \end{aligned} \tag{4.23}$$

$$\begin{aligned} W_{cs} &= (b_{win} - C_s - N_{ss} \cdot C_r) / N_{ss} \\ &= (\frac{A}{2} - H_t + H_w - C_s - N_{ss} \cdot C_r) / N_{ss}, \end{aligned} \tag{4.24}$$

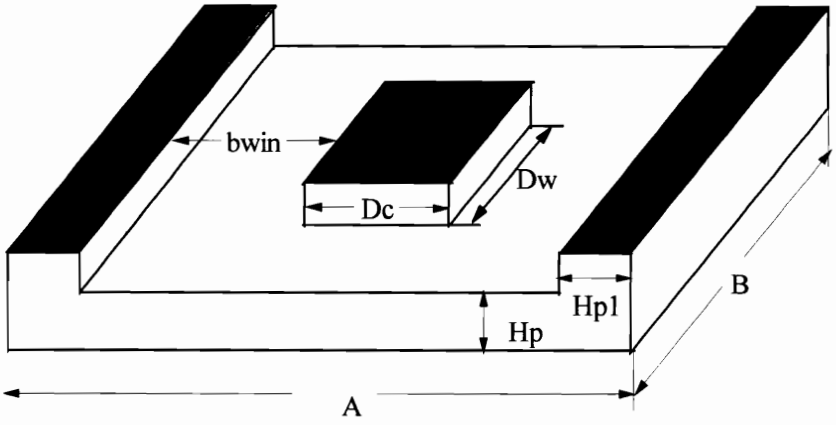

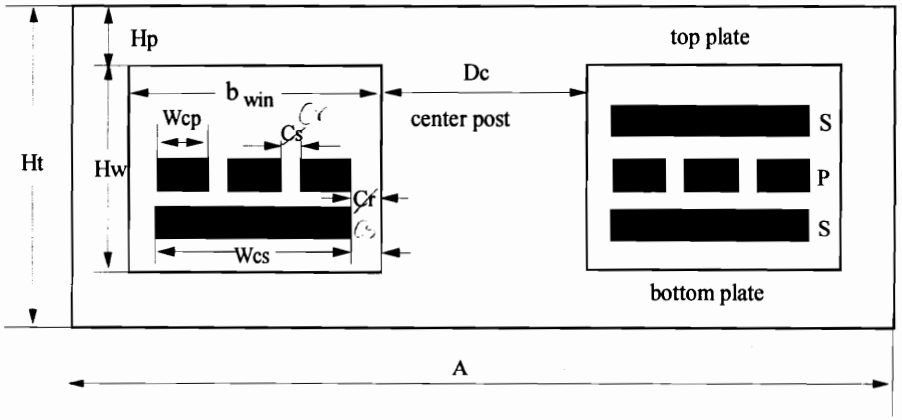

Fig. 4.6 A low-profile E-core.

where W_{cp} and W_{cs} are the conductor widths of primary and secondary windings, respectively; N_{sp} is the number of turns per layer of the primary winding; N_{ss} is the number of turns per layer of the secondary winding; C_s is the clearance distance between the primary and the secondary, and C_r is the distance between traces. The parameters C_s and C_r are decided by the safety requirement.

The total conductor thickness is

$$H_c = K_{vr} \cdot (H_w - (M \cdot NN + 1) \cdot h_i), \tag{4.25}$$

where H_c is the conductor thickness, K_{vr} is window area utilization in a vertical direction, M is the number of sections, and h_i is the insulator thickness between the primary and secondary layers. NN is the total number of layers in each section, which can be decided by:

$$NN = \frac{N_p \cdot M_p}{N_{sp}} + \frac{N_s \cdot M_s}{N_{ss}}, \tag{4.26}$$

where N_p is the primary number of turns in each section, Mp is the number of parallel layers of primary winding in each section, N_s is the number of secondary turns, and Ms is the number of parallel layers of secondary winding in each section. All these parameters are **winding arrangement parameters**.

The total conductor thickness can also be calculated by:

$$H_c = \frac{N_p \cdot M_p}{N_{sp}} \cdot h_p + \frac{N_s \cdot M_s}{N_{ss}} \cdot h_s . \tag{4.27}$$

where h_p and h_s are the thickness of primary and secondary layers, respectively.

If we combine equations (4.25), (4.26) and (4.27), we can calculate secondary winding thickness h_s from the primary winding thickness h_p and winding arrangement parameters:

$$h_s = \frac{K_{vr} \cdot (H_w - (M \cdot NN + 1) \cdot h_i) - \dfrac{N_p \cdot M_p}{N_{sp}} \cdot h_p}{\dfrac{N_s \cdot M_s}{N_{ss}}} \tag{4.28}$$

From equations (4.23), (4.24), and (4.25), we can see that the winding geometry is decided by primary winding thickness, winding arrangement parameters and core geometry parameters.

Therefore, both winding geometry and core geometry are determined by primary winding thickness, winding arrangement parameters and core geometry parameters. These parameters are denominated **geometry parameters.**

4.4 Transformer Loss Expressed as a Function of Core Parameters

According to transformer geometry, transformer power dissipation can be expressed in terms of geometry parameters.

From equation (2.26), power dissipation in transformer winding is proportional to transformer window width b_{win}, mean length per turn l_T, and field intensity H_r:

$$\langle P_d \rangle \propto l_T \cdot \frac{(\sum_{p=1}^{n} N_{tp} I_{tp})^2}{\eta \sigma h_{cu} \frac{D_c + b_{win}}{2} \cdot \ln(1 + \frac{2b_{win}}{D_c})} . \tag{4.29}$$

The mean length per turn l_T can be approximately by

$$l_T = \pi \cdot b_{win} + 2D_w + 2D_c . \tag{4.30}$$

As a result, substituting equations (4.20), (4.21), and (4.30) into (4.29), power dissipation in the transformer cam be expressed by core geometry parameters:

$$\langle P_d \rangle = \frac{\pi \cdot b_{win} + 2D_w + 2D_c}{\frac{D_c + b_{win}}{2} \cdot \ln(1 + \frac{2b_{win}}{D_c})} \cdot \frac{\left(\sum_p N_{lp} I_{lp}\right)^2}{\eta \sigma h_{cu}} \cdot \left[(1 + \alpha_n{}^2 + \beta_n{}^2) G_1(\Delta_n) - 4\alpha_n G_2(\Delta_n)\right]$$

$$\propto \left(\frac{\pi \cdot \frac{A - D_c - H_t + H_w}{2} + 2\left(\frac{V_c}{H_t \cdot A} - (A - D_c - H_t + H_w)\right) + 2D_c}{\frac{D_c + b_{win}}{2} \cdot \ln\left(1 + \frac{2b_{win}}{D_c}\right)} \right) \cdot \frac{\left(\sum_p N_{lp} I_{lp}\right)^2}{\eta \sigma h_{cu}}$$

$$\propto \left(\frac{\pi \cdot \frac{A - D_c - H_t + H_w}{2} + 2\left(\frac{V_c}{H_t \cdot A} - A + H_t - H_w + 2D_c\right)}{\frac{D_c + (A - D_c - H_t + H_w)}{2} \cdot \ln\left(1 + \frac{A - D_c - H_t + H_w}{D_c}\right)} \right) \cdot \frac{\left(\sum_p N_{lp} I_{lp}\right)^2}{\eta \sigma h_{cu}}$$

$$\propto \left(\frac{2\frac{V_c}{H_t \cdot A} + (4 - \frac{\pi}{2})D_c - (2 - \frac{\pi}{2})(A - H_t + H_w)}{\frac{A - H_t + H_w}{2} \cdot \ln\left(\frac{A - H_t + H_w}{D_c}\right)} \right) \cdot \frac{\left(\sum_p N_{lp} I_{lp}\right)^2}{\eta \sigma h_{cu}} .$$

(4.31)

According to equation (4.6), the core loss is considered to be piece-wise uniformly distributed in each section and calculated by using the empirical method. The core loss can be expressed in terms of core geometry parameters as follows:

$$P_c \propto f^{\alpha} \cdot {B_c}^{\beta} \cdot V_e$$

$$\propto f^{\alpha} \sum_i \cdot \left(\frac{V_p \cdot D}{N_p \cdot f \cdot A_{ei}} \right)^{\beta} \cdot A_{ei} \cdot l_{ei}$$

$$\propto K f^{\alpha} \left(\frac{n V_o D}{N_p f} \right)^{\beta} \cdot \left[(H_t - 2H_p) \cdot (D_c \cdot D_w)^{1-\beta} + (A - 2H_p) \cdot (2H_p \cdot B)^{1-\beta} + Ht \cdot (2H_p \cdot B)^{1-\beta} \right]$$

$$\propto Kf^{\alpha}\left(\frac{nV_oD}{N_pf}\right)^{\beta}\left[\frac{2H_w+A}{\left(D_c\cdot\left(\frac{V_c}{H_t\cdot A}-(A-D_c-H_t+H_w)\right)\right)^{\beta-1}}\right] \tag{4.32}$$

where l_{ei} is the magnetic mean length of each section, and A_{ei} is the cross-sectional area of each section.

Both the winding loss and the core loss are expressed by the following geometry parameters window height H_w, transformer height H_t, core width A, and center post width D_c. The relations between the transformer loss and geometry parameters can be found by taking the partial derivative with respect to the geometry parameters:

$$\frac{\partial P_d}{\partial H_w}\propto\frac{\left(\sum_p N_{lp}I_{lp}\right)^2}{\eta\sigma h_{cu}}\cdot\left\{\frac{\left(\frac{A-H_t+H_w}{2}\cdot\ln(\frac{A-H_t+H_w}{D_c})\right)\left((-1)\cdot(2-\frac{\pi}{2})\right)}{\left(\frac{A-H_t+H_w}{2}\cdot\ln(\frac{A-H_t+H_w}{D_c})\right)^2}\right.$$
$$\left.-\frac{\left(2\frac{V_c}{H_t\cdot A}+(4-\frac{\pi}{2})D_c-(2-\frac{\pi}{2})(A-H_t+H_w)\right)\cdot\left(\frac{1}{2}\ln(\frac{A-H_t+H_w}{D_c})+\frac{D_c}{2}\right)}{\left(\frac{A-H_t+H_w}{2}\cdot\ln(\frac{A-H_t+H_w}{D_c})\right)^2}\right\}$$

$$<0\,. \tag{4.33}$$

$$\frac{\partial P_d}{\partial A} \propto \frac{\left(\sum_p N_{lp} I_{lp}\right)^2}{\eta \sigma h_{cu}} \cdot \left\{ \frac{\left(\frac{A - H_t + H_w}{2} \cdot \ln\left(\frac{A - H_t + H_w}{D_c}\right)\right)\left(-\frac{2V_c}{H_t \cdot A^2} - (2 - \frac{\pi}{2})\right)}{\left(\frac{A - H_t + H_w}{2} \cdot \ln\left(\frac{A - H_t + H_w}{D_c}\right)\right)^2} \right.$$

$$\left. - \frac{\left(2\frac{V_c}{H_t \cdot A} + (4 - \frac{\pi}{2})D_c - (2 - \frac{\pi}{2})(A - H_t + H_w)\right) \cdot \left(\frac{1}{2}\ln\left(\frac{A - H_t + H_w}{D_c}\right) + \frac{D_c}{2}\right)}{\left(\frac{A - H_t + H_w}{2} \cdot \ln\left(\frac{A - H_t + H_w}{D_c}\right)\right)^2} \right\}$$

$$< 0 . \tag{4.34}$$

$$\frac{\partial P_d}{\partial D_c} \propto \frac{\left(\sum_p N_{lp} I_{lp}\right)^2}{\eta \sigma h_{cu}} \cdot \left\{ \frac{\left(\frac{A - H_t + H_w}{2} \cdot \ln\left(\frac{A - H_t + H_w}{D_c}\right)\right)(4 - \frac{\pi}{2})}{\left(\frac{A - H_t + H_w}{2} \cdot \ln\left(\frac{A - H_t + H_w}{D_c}\right)\right)^2} \right.$$

$$\left. - \frac{\left(2\frac{V_c}{H_t \cdot A} + (4 - \frac{\pi}{2})D_c - (2 - \frac{\pi}{2})(A - H_t + H_w)\right) \cdot \left(-\frac{1}{2}\right)}{\left(\frac{A - H_t + H_w}{2} \cdot \ln\left(\frac{A - H_t + H_w}{D_c}\right)\right)^2} \right\}$$

$$> 0 . \tag{4.35}$$

$$\frac{\partial P_f}{\partial H_w} \propto K f^{\alpha} \left(\frac{n V_o D}{N_p f}\right)^{\beta} \left[\frac{2D_c \cdot \left(\frac{V_c}{H_t \cdot A} - (A - D_c - H_t + H_w)\right) + (2H_w + A)(\beta - 1)D_c}{\left(D_c \cdot \left(\frac{V_c}{H_t \cdot A} - (A - D_c - H_t + H_w)\right)\right)^{\beta}} \right]$$

$$> 0 . \tag{4.36}$$

$$\frac{\partial P_f}{\partial A} \propto \frac{Kf^{\alpha}\left(\frac{nV_oD}{N_pf}\right)^{\beta}}{\left(D_c \cdot [\frac{V_c}{H_t \cdot A} - (A - D_c - H_t + H_w)]\right)^{\beta}} \cdot$$

$$\left[D_c \cdot [\frac{V_c}{H_t \cdot A} - (A - D_c - H_t + H_w)] + (2H_w + A)(\beta - 1)(\frac{D_c V_c}{H_t A^2} + D_c)\right]$$

$$> 0. \tag{4.37}$$

$$\frac{\partial P_f}{\partial D_c} \propto Kf^{\alpha}\left(\frac{nV_oD}{N_pf}\right)^{\beta}\left[-\frac{(\beta - 1)\cdot\left(\frac{V_c}{H_t \cdot A} - (A - D_c - H_t + H_w) + D_c\right)}{(\beta - 2)\left(D_c \cdot \left(\frac{V_c}{H_t \cdot A} - (A - D_c - H_t + H_w)\right)\right)^{\beta-2}}\right]$$

$$< 0. \tag{4.38}$$

The transformer winding loss increases with center post width D_c, and decreases with core width A, and window height H_w, whereas the transformer core loss increases with core width A, window height H_w, and decreases with center post width D_c.

Equations (4.33) and (4.36) show that the variation of transformer window height *Hw* impacts the core loss and the winding loss. With the fixed transformer volume and transformer height (which means the fixed transformer footprint), the increase of the window height causes the decrease of the winding loss and the increase of the core loss. The higher window height will result in a wider window width and smaller center post

depth, as indicated by equations (4.20) and (4.21), which implies the lower current density in the winding and higher flux density in the core, and hence the lower copper loss and higher core loss. Because the transformer with a larger window area has a lower copper loss and a higher core loss, and the transformer with a smaller window height has a higher copper loss and a lower core loss, the total transformer loss displays a U-shaped characteristic as a function of the changing window height. Therefore, there is a window height that will result in a minimum transformer loss.

Equations (4.34) and (4.37) show that the variation of core width A impacts the core loss and winding loss. With the fixed transformer volume and height, as core width A increases, core depth B decreases, as indicated by equation (4.22), which results in a smaller cross section area of the core, and hence the higher core loss. On the other hand, the larger core width A will result in a larger winding width (indicated by equation (4.20)). Therefore, the winding loss is reduced. So, as the core width increases, the transformer loss displays a U-shaped characteristic, which implies the existence of a core width A that will result in a minimum loss.

Similarly, as the window height and core width affect the total loss, the variation of center post width D_c impacts the core loss and winding loss too. The larger center post width D_c will result in a higher winding loss and lower core loss, and vice versa. The transformer total loss displays a U-shaped characteristic as the changing of center post

width. Therefore, there is a center post width that will result in a minimum transformer loss.

As window height H_w, core width A, and center post width D_c affect the total loss, the primary thickness will affect the winding loss. With the fixed winding height and insulator thickness, as the primary thickness increases, so does the secondary winding resistance, while the primary winding resistance decreases. So, there is a primary winding thickness which will result in a minimum winding loss.

It is clear that for a given transformer height and volume, there is one set of the geometry parameters that gives the minimum transformer loss. The geometry that corresponds to the minimum transformer loss is found by an optimization process.

4.5 Minimum Volume Design for Low-Profile Transformers

4.5.1 Design Algorithm

Based on the above analysis, an algorithm is developed for transformer design which maximizes power density. The derived winding loss model, core loss model, and thermal model are used in the optimization program to find the maximum power density of the transformer. Figure 4.7 gives the conceptual flow chart of the algorithm. Two

design procedures are involved in the optimization process. They are the general design and fine tuning.

Procedure I (General Design):

In this procedure, the method based on one-dimensional winding loss model derived in Chapter 2 is used to calculate the winding loss, and the core loss and thermal models derived in sections 4.1 and 4.2 are used to evaluate the transformer core loss and temperature rise. The detailed design steps can be described as follows:

(1) The values of input constants are given. The input constants are temperature rise requirement, output power, output voltage, material characteristics, insulation thickness, and core-winding clearance.

(2) The range of design variables, operating frequency, turns ratio, efficiency, and transformer height, are chosen.

(3) The search process starts with a selected frequency and height to obtain a design that offers the minimum volume of transformer and meets the efficiency requirement and thermal constraint.

(4) The height of transformer is varied, and the minimum volume design is then identified. This process continues until the entire range of the pre-specified transformer height is explored.

(5) The next step is to vary the operating frequency and repeat the same process as the one described in step 3.

(6) The outcome of the design process defined in steps 4 and 5 will generate a family of curves, where every point on the design curve represents a minimum volume design for a given transformer height and operating frequency. Based on these curves, it is very easy to identify the maximum achievable power density.

(7) Once the minimum volume design is identified, the program will spell out the detailed design parameters, such as transformer geometry, maximum power density, optimum frequency, and winding structure.

Figure 4.8 describes in a greater detail the design process of searching for the minimum transformer volume under the constraints defined by the design specifications. In order to find the minimum transformer volume for each given height, an initial value of the transformer volume is given. With the given transformer volume and height, the optimization routine will search for a transformer geometry with the minimum power dissipation and the acceptable temperature rise. If the transformer does not meet the efficiency requirement, the transformer volume has to be changed, and the same process will be carried out again for the new transformer volume. If the transformer efficiency

finally meets the requirement, the design is completed. The final results are "optimal" among all possible solutions.

Procedure II (Fine Tuning):

In design procedure I, a one-dimensional method is used for winding loss analysis. As mentioned in Chapter 2, the one-dimensional method neglects the transformer edge effect and termination loss, and it has at least 10% error in transformer winding loss calculation. In order to obtain a more accurate design, procedure II (fine tuning) is applied. In this procedure, the FEA method is used to calculate winding loss for the transformer designed in procedure I; this time, the transformer edge effects and termination effect are taken into account. The correcting factor K_p, which is defined as

$$K_p = \frac{\text{Winding loss calculated from FEA method}}{\text{Winding loss calculated from 1-D method}}, \qquad (4.39)$$

will be found. In the optimization routine, the 1-D winding loss will be increased K_p times to compensate for the effect that has been ignored. Therefore, the subsequent steps are:

(8) Transformer winding loss is calculated by using the FEA, the correcting factor is found, and the 1-D winding loss calculation is modified.

(9) The final step is to repeat the same process that is described in steps 3 and 4, and output the design results.

The algorithm is realized by using a nonlinear optimization technique and is coded into a program. The program is written using Matlab which has a built-in optimization routine and good graphics capability. Following the above design algorithm and design procedures mentioned in the following section, the transformer can be optimized.

4.5.2 Design Objectives

The optimization is realized according to the following objective function:

$$\text{minimize } f(x)$$

$$\text{subject to } g_j(x) \le 0,\ j = 1, 2, \ldots, r$$

$$\text{and } x \in S,$$

where f(x) is the objective function, x is an n-dimensional vector of geometry parameters, $g_j(x)$ are the inequality constraints, and S is a subset of the n-dimensional space. For the above mentioned transformer optimization, the objective function is power dissipation of transformer $P_{loss}(x)$, and the constraints are:

Temperature rise:	$\Delta T \le$ a given temperature rise requirement
Flux density:	$0 \le B_m \le 0.7B_{sat}$,
Plate thickness:	$1.5 \text{ mm} \le H_p \le \frac{H_t}{2}$,

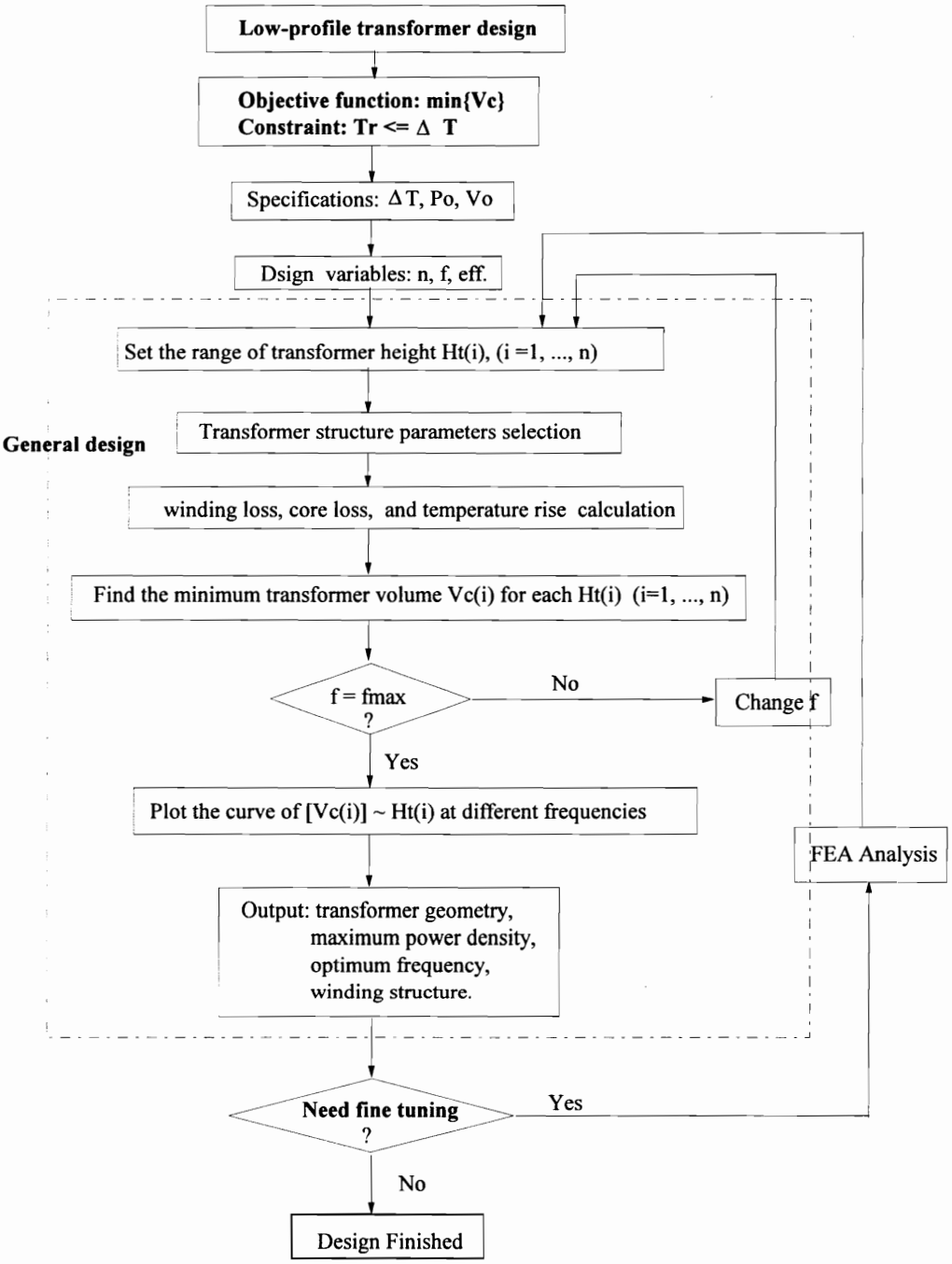

Fig. 4.7 The functional flow chart of the design algorithm.

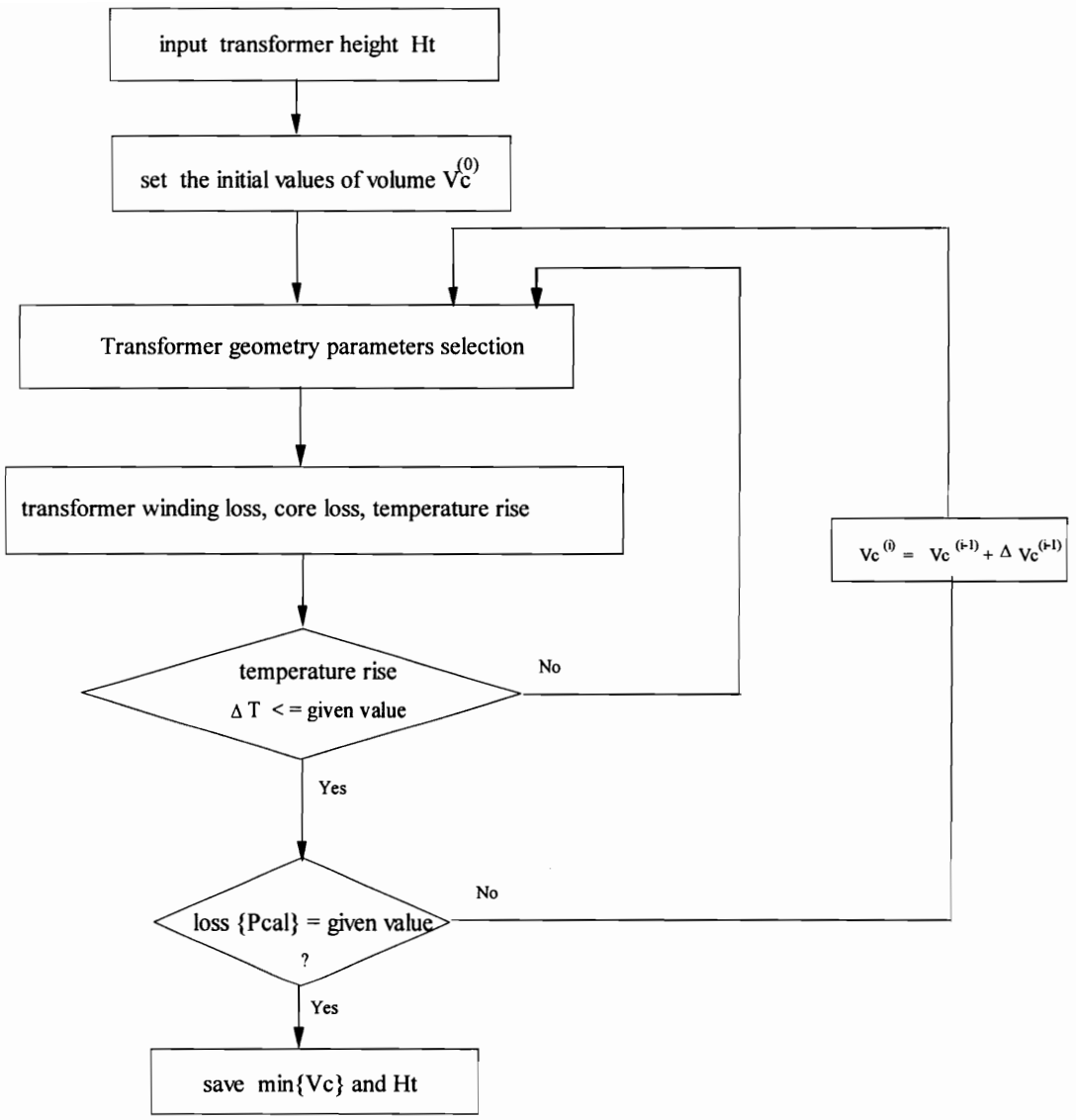

Fig. 4.8 The design procedure for a transformer with the minimum volume.

Window width: $b_{win} \geq 0$,
Primary thickness: $h_s \geq 0$,
Primary winding width: $W_{cp} \geq 0$,
Primary winding width: $W_{cs} \geq 0$,

where the first constraint confines the temperature rise of the transformer. The second constraint limits the flux density in the transformer to prevent core saturation and ensure that the core loss density remains within the reasonable range (below 0.5 W/cm^3). The third constraint ensures that the core plate thickness provides enough mechanical strength (>= 1.5 mm) and that the window height is positive. Other constraints specify the physical dimensions of the transformer as positive numbers to ensure that the results are physically meaningful.

4.5.3 Design Examples

To demonstrate the described optimization algorithm and the proposed procedures of determining the maximum power density of transformers, several transformers are designed by using the optimization program and built to verify the design results.

Example I: Low-Profile Transformer Design with Maximum Power Density

A low-profile transformer for a 100-W, 3.3-V output active clamp forward PWM converter (shown in Fig. 4.9(a)) was designed with the following design targets:

- Input voltage V_{in} : 56 V,
- Output voltage V : 3.3 V,
- Output power P_o: 100 W,
- Transformer turns ratio n: 7:1,
- Operating frequency f: 300 kHz.

The design constraints are:

- Temperature rise: $\Delta T \leq 50\ ^{o}$
- $D_w = B$

The first constraint is to limit the temperature rise of the transformer. The second constraint is to limit the center post depth to the core depth. As a result, the transformer core has the geometry as shown in Fig. 4.10.

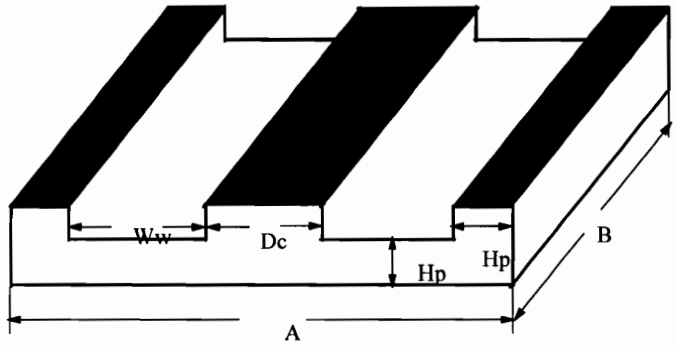

Fig. 4.10 Transformer core geometry for design example 1.

The winding arrangement of the transformer is shown in Fig. 4.11(b), which is an interleaved structure with a 7-layer series-connected primary and a 7-layer parallel-connected secondary.

The input constants are listed in Table 4.3. The optimization results from procedure I -- general design-- are shown in Fig. 4.12. It gives the plot of the 100-W, 3.3-V-output, 7:1 transformer volume versus height at different frequencies (from 100 kHz to 2 MHz). Each curve of the transformer volume versus height shows a V-shape. The transformer volume decreases as the height is initially reduced from a large value, and it reaches its minimum value at some point. After that, the transformer volume increases greatly. It indicates the existence of a critical height for each frequency, at which the power density of the transformer reaches its maximum value. The height at which the power density peaks is designated as **optimal height**. The reason for the existence of the optimal height is explained as follows.

When the transformer is very thin, the total loss is dominated by the winding loss (as shown in Fig. 4.13(b)). The winding width has to be increased to lower the winding resistance. Therefore, the footprint is increased and power density is decreased. On the other hand, when the transformer height is larger, the total loss is dominated by the core loss, which also can be seen in Fig. 4.13(b). As a result, the cross-sectional area of the core has to increase to lower the flux density, and hence the core loss. Since the increase of the cross-sectional area results in the increase of core width A and core depth B, the transformer footprint has to increase as well. Finally, the core volume increases and the power density drops.

From Fig. 4.12, we can also see that the optimal heights and the transformer volume are reduced as the frequency increases from 100 kHz to 1 MHz, since the core size decreases with the increase of frequency. However, if the frequency is increased to 2 MHz, both the transformer volume and optimal height will increase to values larger than those at 500 kHz and 1 MHz. This is due to the fact that the conductor thickness is limited by high-frequency skin depth, and the winding width has to be increased to lower the ac-resistance. Furthermore, any ferrite material is optimal only within a certain frequency range, e.g. Magnetic-K material is a good material within 1 MHz. Beyond this range, the core loss will increase. So the cross-sectional area of the core has to be increased to lower the flux density, and hence the core loss. As a result, the footprint and volume increase.

From Fig. 4.13(a), it is clear that the optimal height of this transformer is 8 mm, at which the transformer has the maximum power density. The dimensions of the optimally designed transformer are shown in Table 4.4, column A.

For the 100-W transformer, the winding losses calculated by means of one-dimensional and two dimensional methods are 0.607 W and 0.63 W, respectively. The winding loss calculated by using the one-dimensional method is 4% lower than that obtained by the two-dimensional method. So, the winding loss obtained with the one-dimensional method is justified by a weight factor of 1.04. The optimization results after the fine tuning are shown in Table 4.4, column B. Comparing column B with column A, we can see that the change in dimensions is very small. This is because the transformer has the interleaving winding arrangement and operates at 300 kHz, where the edge effect plays only a minor role in transformer winding loss. At this frequency, the one-dimensional method has enough accuracy to predict power dissipation of the transformer for the interleaving arrangement. The fine tuning procedure is not necessary in this case. However, for higher operating frequencies (especially > 500 kHz) and non-interleaving winding structures, this fine tuning procedure is necessary and recommended. This necessity is demonstrated in another design example.

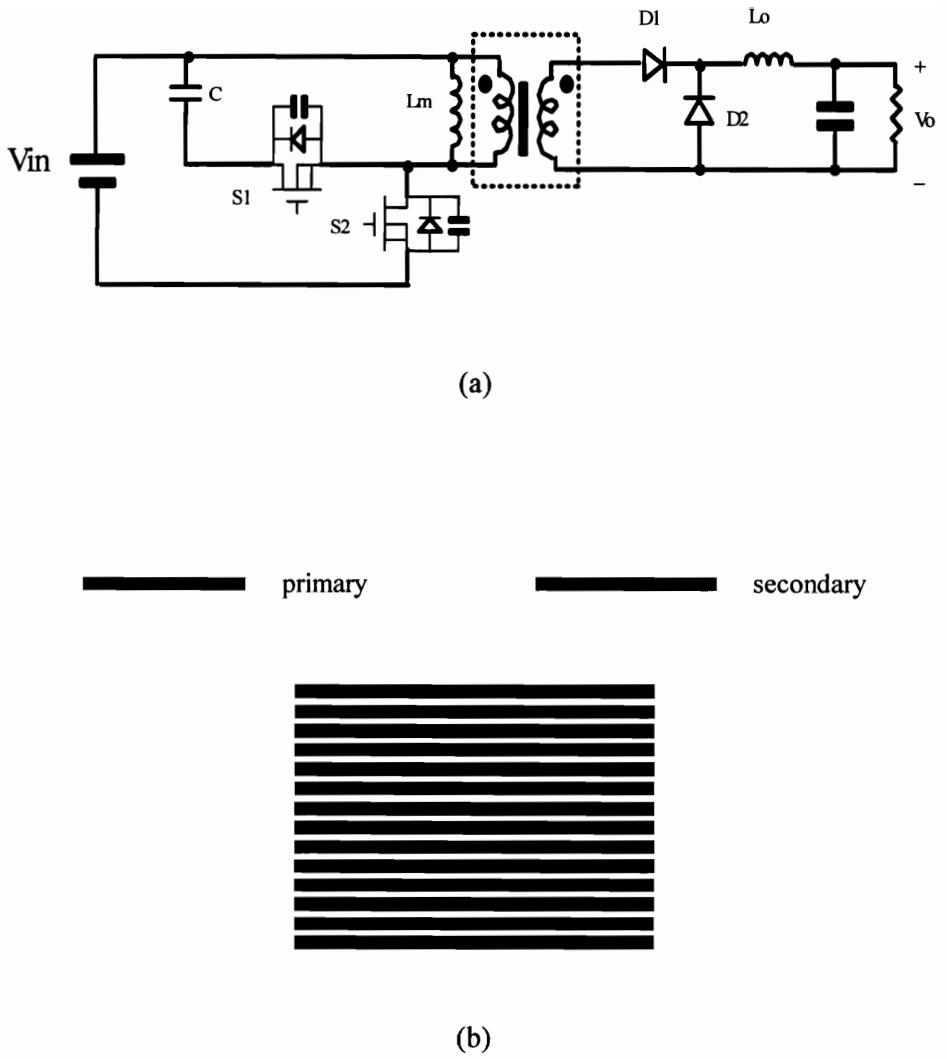

Fig. 4.11 (a) Circuit diagram of an active clamp forward converter. (b) Transformer winding arrangement.

Table 4.3 List of input constants.

Input voltage V_{in} (V)	48
Output voltage V (V)	3.3
Output power P_o(W)	100
Transformer turns ratio n	7:1
Insulator thickness h_i (mil)	4
Clearance distance between primary and secondary C_s (mil)	50
Window area utilization in vertical direction K_{vr}	0.8
Conductivity of copper σ_{cu} (S/m)	5.8×10^7
Permittivity of air μ_o (H/m)	$4\pi \times 10^{-7}$
Thermal resistivity of insulator R_{thi} (m°C/W)	8
Thermal resistivity of copper R_{thc} (m°C/W)	0.0026
Thermal resistivity of ferrite R_{thf} (m°C/W)	0.25
Thermal resistivity of air R_{tha} (m°C/W)	38.76

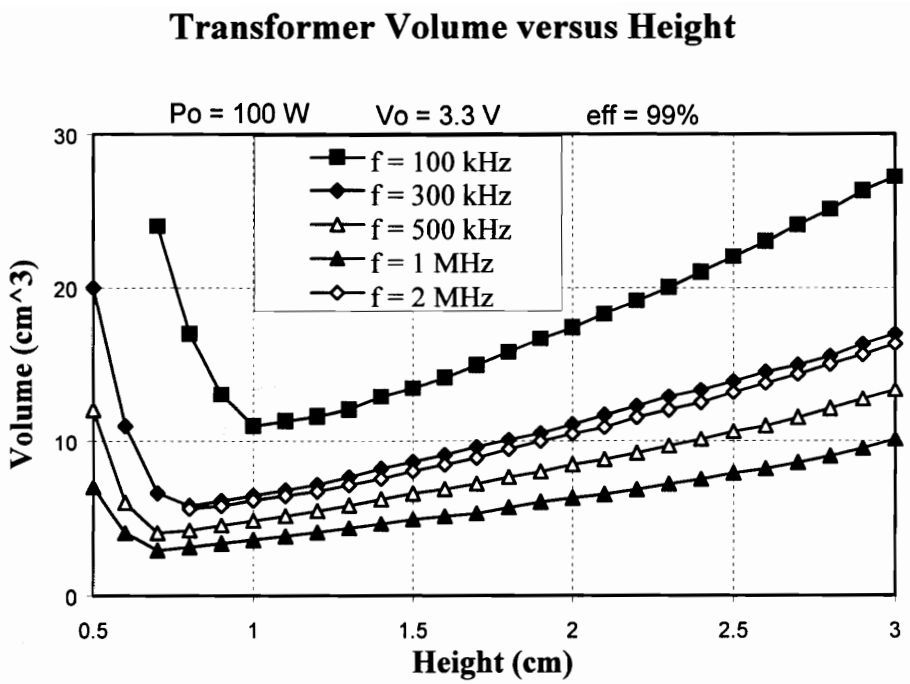

Fig. 4.12 Transformer volume versus transformer height at different frequencies.

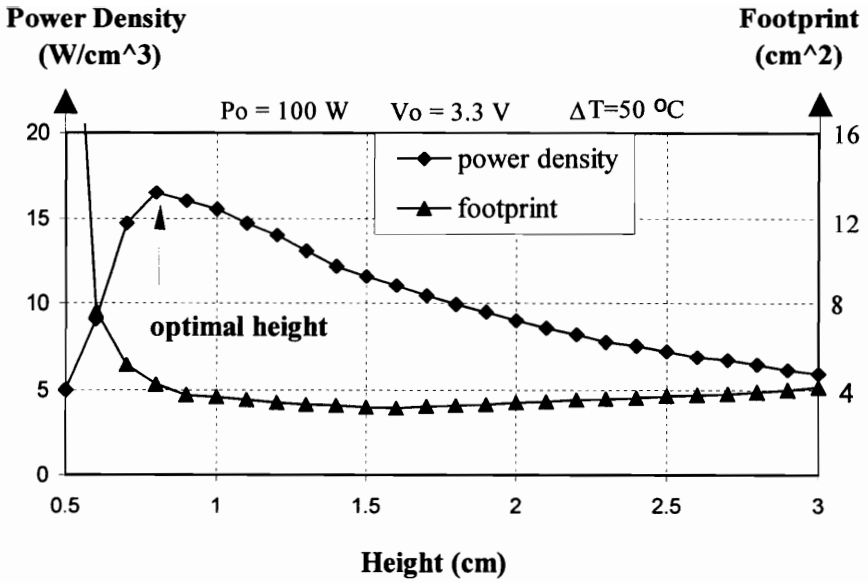

(a) Transformer power density and footprint versus height.

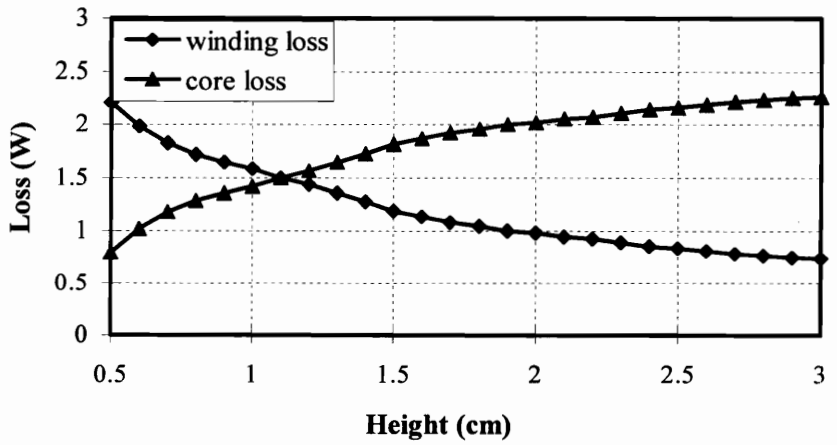

(b) Transformer loss versus height.

Fig. 4.13 (a) The plot of the 100-W @ 3.3-V output, 7:1 transformer power density versus transformer height at 300 kHz. (b) Transformer winding loss and core loss versus height at 300 kHz.

Table 4.4 Optimally designed transformer dimensions. (A) General design results. (B) Optimization results after fine tuning. (C) Measurement results.

	Optimization		Measurement
	(A) Procedure I	(B) Procedure II	(C)
Transformer volume V_c (cm^3)	4.4	4.5	4.6
Transformer height H_t (cm)	0.82	0.82	0.82
Center post width D_c (cm)	0.45	0.44	0.44
Window height H_w (cm)	0.36	0.38	0.38
Plate thickness H_p (cm)	0.24	0.22	0.22
Core depth B (cm)	1.60	1.65	1.65
Core width A (cm)	1.72	1.76	1.76
Window width b_{win}	0.40	0.44	0.44
Primary thickness h_p (mil)	3	3	3
Secondary thickness h_s (mil)	3	3	3
Primary winding width W_p (cm)	0.3	0.34	0.32
Secondary winding width W_s (cm)	0.32	0.33	0.36
Winding loss (W)	0.65	0.652	0.852
Core loss (W)	0.35	0.352	0.392
Temperature rise (°C)	49.2	50.6	53.1

According to the design results shown in Table 4.4, the transformer has been built by using 3 mil copper foil and tested in a 100-W @ 3.3-V active clamp forward converter. The measurement results of the transformer dimension, winding loss, core loss, and temperature rise are shown in Table 4.4 Column C. The transformer winding loss and core loss are measured by Impedance Analyzer HP 4129A, and the temperature rise is measured by the 10 Channel Digital Thermometer.

Example II: Low-Profile Transformer Design With a Given Height Requirement

A 6-mm-high transformer for a 100-W, 3.3-V output active clamp forward PWM converter (shown in Fig. 4.10(a)) was designed with following design targets:

- Input voltage V_{in} : 56 V,
- Output voltage V : 3.3 V,
- Output power P_o: 100 W,
- Transformer turns ratio n: 7:1,

- Operating frequency f: 300 kHz,

- **Transformer height <= 6 mm.**

The design constraints are:

- Temperature rise: $\Delta T \leq 40\ ^{\circ}$

- $D_w = B$

The first constraint is to limit the temperature rise of the transformer. The second constraint is to limit the center post depth to the core depth.

Several possible winding arrangements for this transformer are shown in Fig. 4.14. Case A is a 14-layer interleaving structure with a 7-layer series-connected primary and a 7-layer parallel-connected secondary, which has the minimum ac-resistance and leakage inductance compared to Cases B and C. Cases B and C are 11-layer non-interleaving winding structures with a 7-layer series-connected primary and a 4-layer parallel-connected secondary. But Case C has less power dissipation than case B because of the lower leakage field intensity in the transformer window area. All the winding arrangements are evaluated by the optimization program. Figure 4.15 gives the plot of footprint versus height of transformers with the three winding arrangements. It is clear that the transformer with winding arrangement C has the smallest footprint when

transformer height is 6 mm. Therefore, winding arrangement C is selected, since it meets the height requirement and has the highest power density.

Table 4.5 lists the optimized transformer dimensions after the two design procedures: general design and fine tuning. According to the optimization results, a modified standard EE core Philips-3F3 EE 22/5.7/16 and PLT 22/16/2.5 is selected to build the transformer. The plate thickness and window height were milled down to 1.5 mm and 3 mm from their original dimensions of 2.5 mm and 6.4 mm, to get a 6-mm height low-profile core. Figure 4.16 shows the primary and secondary winding structures. The strip winding pattern is folded to construct a 7-turn primary. The four-layer secondary is paralleled externally. The transformer was built and tested in a 100-W 3.3-V output active clamp forward converter. Table 4.6 shows the comparison of the design and experimental results, with column A giving the optimization design results and column B presenting the experimental results. The winding loss was measured by using HP 4129A Impedance Analyzer, and the temperature rise was measured by using 2166A 10-Channel Digital Thermometer. The experimental results show that the optimization program is accurate enough to design low-profile transformers. The largest mismatch is the temperature rise, which can be attributed to the fact that the constructed transformer has a larger footprint than that required by the design. The discrepancy between the measured and predicted winding losses is due to the termination loss.

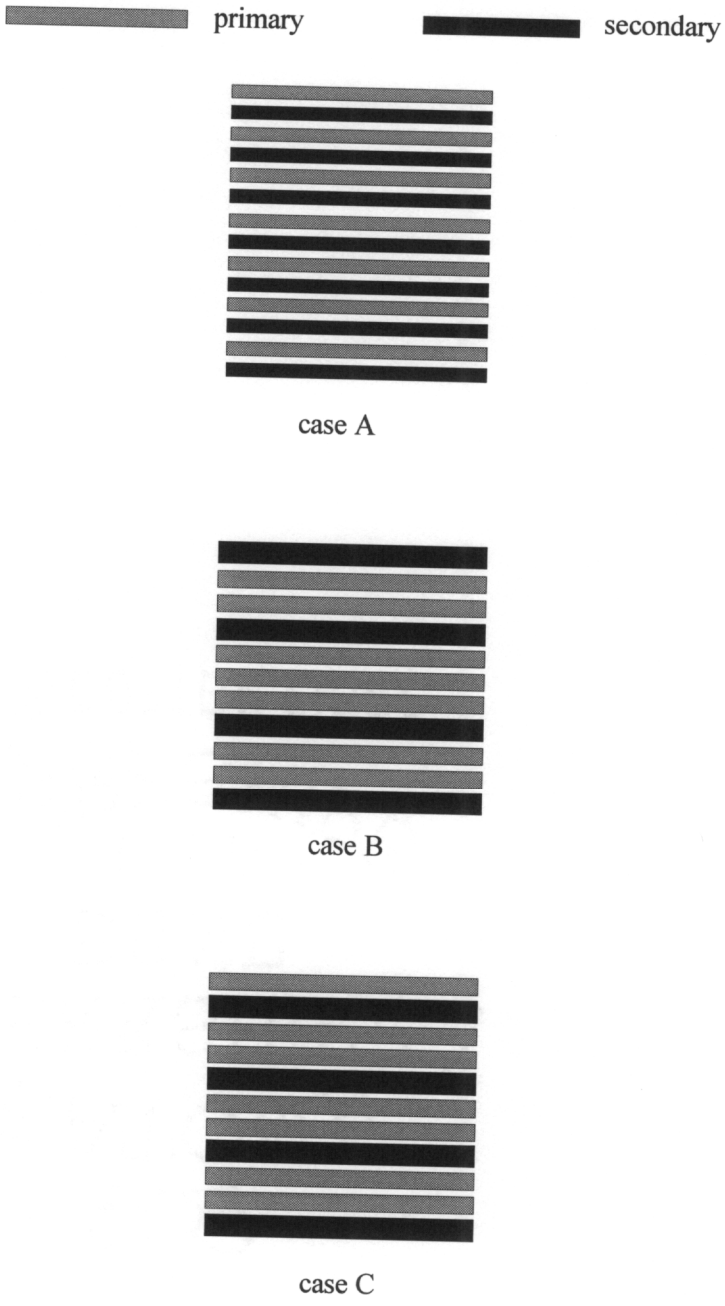

Fig. 4.14 Possible winding arrangements for transformer design example II.

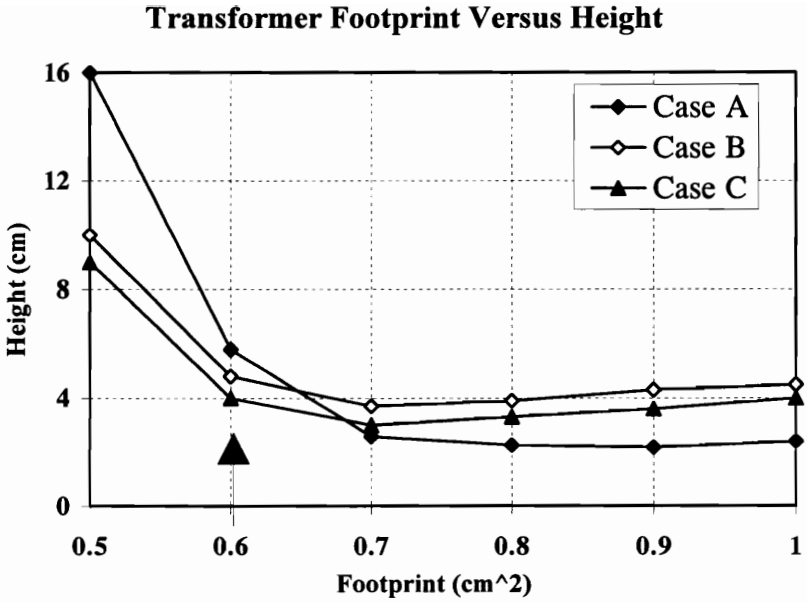

Fig. 4.15 Transformer footprint versus height for different winding arrangements (cases A, B, and C).

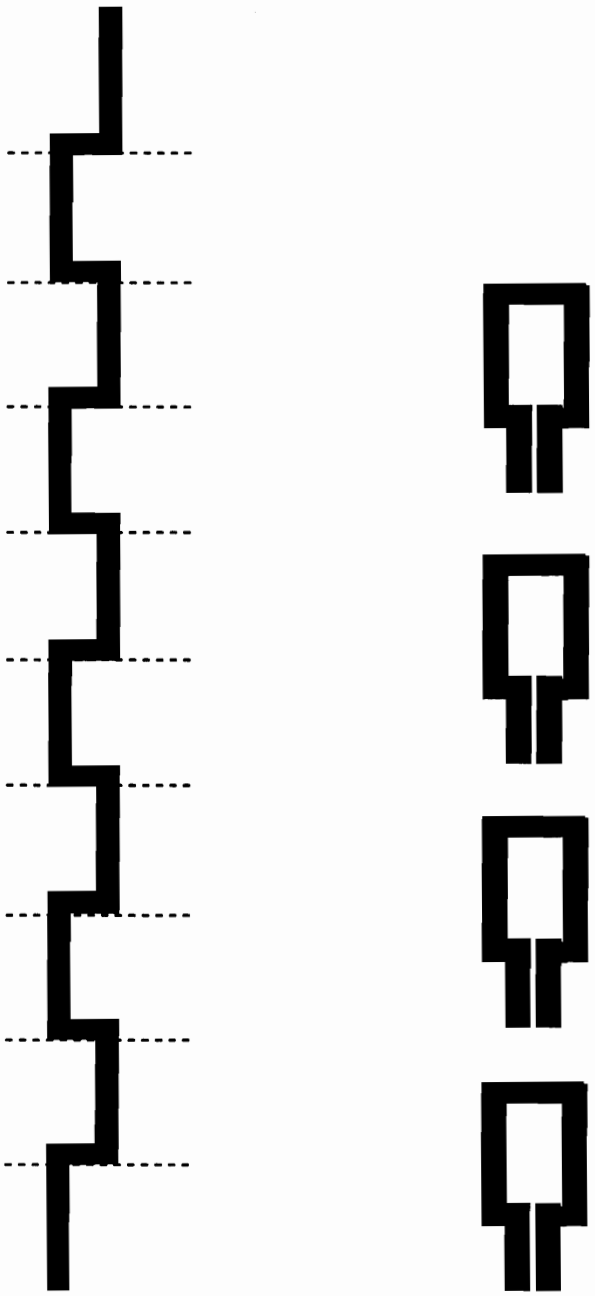

(a) Primary winding pattern. (b) Secondary winding pattern.

Fig. 4.16 Transformer winding pattern. (a) The folded winding pattern is for primary built with 3-mil copper foil. The dashed line represents the fold line. (b) The secondary is externally paralleled, built with 6 mil copper foil.

Table 4.5 Optimally designed transformer dimensions. (A) General design results. (B) Optimization results after fine tuning.

	(A) Procedure I	(B) Procedure II
Transformer height H_t (cm)	0.6	0.6
Center post width D_c (cm)	0.52	0.53
Window height H_w (cm)	0.3	0.30
Plate thickness H_p (cm)	0.15	0.15
Core depth B (cm)	1.4	1.4
Core width A (cm)	1.98	2.02
Window width b_{win}	0.46	0.48
Primary copper thickness h_p (mil)	3	3
Secondary copper thickness h_s (mil)	6	6
Transformer winding loss (W)	0.72	0.68
Transformer core loss (W)	0.28	0.32

Table 4.6 Comparison of the optimization results with real results for design example II.

	predicted	measured
Transformer height H_t (cm)	0.6	0.6
Center post width D_c (cm)	0.53	0.5
Window height H_w (cm)	0.30	0.3
Plate thickness H_p (cm)	0.15	0.15
Core depth B (cm)	1.4	1.58
Core width A (cm)	2.02	2.2
Window width b_{win}	0.48	0.59
Primary thickness h_p (mil)	3	3
Secondary thickness h_s (mil)	6	6
Transformer winding loss (W)	0.68	0.77
Transformer core loss (W)	0.32	0.35
Temperature rise (°C)	37.8	40.5

Example III: Low-Profile Transformer Design With Different Core Geometries

The transformers designed in examples I and II are under constraint: $D_w = B$. However, a total custom designed transformer core should not be confined by the constraint. To demonstrate the advantages of a custom-designed transformer, two transformers have been designed for a half-bridge 50 W @ 3.3 V PWM forward converter. One transformer (named transformer I) was designed with the constraint $D_w = B$. Another transformer (named transformer II) was designed without the constraint.

The design targets are:

- Input voltage V_{in} : 28 V,
- Output voltage V : 3.3 V,
- Output power P_o: 50 W,
- Transformer turns ratio n: 4:1,
- Operating frequency f: 500 kHz.

The design constraints for transformer I are:

- Temperature rise: $\Delta T \leq 25\ ^{o}C$

- $D_w = B$.

The design constrains for transformer II is:

- Temperature rise: $\Delta T \leq 25\ ^{o}C$

Figure 4.17 shows the geometries of transformers I and II. The optimization results of transformer I and II are shown in Table 4.7. According to the design results, both transformers have been built and tested in a 50-W@ 3.3-V forward converter. For the same temperature rise, the custom-designed transformer has smaller footprint and volume. Compared with the transformer I, the custom-designed transformer has a 20% volume reduction with the same temperature rise.

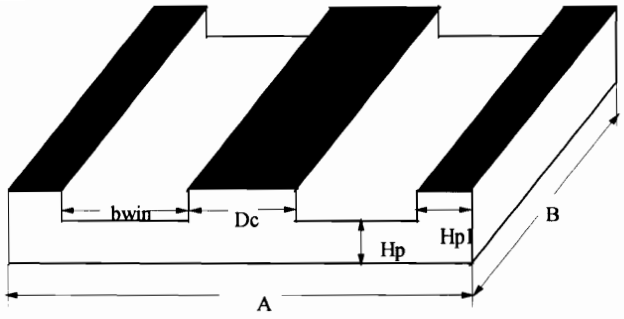

(a) Geometry for transformer I.

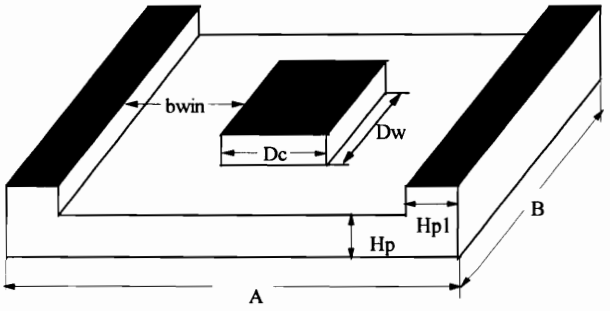

(b) Geometry for transformer II.

Fig. 4.17 Two kinds of transformer geometries.

Table 4.7 Comparison of the optimization results of transformer I and II.

	Transformer I	**Transformer II**
Transformer height H_t (cm)	0.62	0.62
Center post width D_c (cm)	0.46	0.78
Window height H_w (cm)	0.32	0.32
Plate thickness H_p (cm)	0.15	0.15
Core depth B (cm)	1.47	1.64
Core width A (cm)	1.92	2.0
Window width b_{win}	0.5	0.4
Primary thickness h_p (mil)	3	3
Secondary thickness h_s (mil)	3	3
Transformer winding loss (W)	0.68	0.77
Transformer core loss (W)	0.37	0.35
Transformer footprint (cm^2)	4.74	3.28

4.6 Summary

An algorithm has been developed to design a low-profile transformer that has the highest power density and meets a given set of specifications. The maximum achievable power density for a given power level and output voltage has been computed based on only one fundamental constraint: the temperature rise. The algorithm has been realized by using a nonlinear optimization technique and is coded into a program. The program produced a family of curves that present the relationship between the power density and transformer height, where every point in the design curve represents a minimum volume design for a given transformer height and operating frequency. It is found that for any power level and operating frequency, there is an optimal height at which the power density of the transformer reaches its maximum value. Based on these curves, it is very easy to identify the maximum achievable power density, the transformer geometry, optimum frequency, and winding structure.

Several transformers have been designed with the help of the program and built to verify the optimization results. They show that the algorithm is accurate enough. The optimally designed custom core has been compared with the optimally designed conventional core; the results show that the transformer with the optimally designed custom core has a smaller volume than the transformer with the optimally designed conventional core.

Chapter 5

Low-Profile Transformer Termination Design

In addition to the transformer winding loss and core loss, the transformer termination loss is another important factor that affects transformer performance. An optimally designed transformer should have the best winding arrangement and the best termination design as well. In order to show the termination effect and the way to reduce the termination loss, a low-profile transformer and its termination were designed for a 300-W, 5-V-output active clamp forward PWM converter (shown in Fig. 5.1 (a)) with the following design targets:

- Input voltage V_{in} : 56 V,

- Output voltage V : 5 V,
- Output power P_o: 300 W,
- Transformer turns ratio n: 4:1,
- Operating frequency f: 400 kHz,
- Transformer height < 0.25 in".

The winding arrangement of the transformer is shown in Fig. 5.1(b), which depicts an interleaved structure with a 4-layer series-connected primary and a 4-layer parallel-connected secondary. According to the optimization procedure mentioned in Chapter 4, the transformer dimensions are shown in Table 5.1. A modified standard RM10 core Philips 3F3 is selected to build the transformer. There are several approaches to implementing planar windings. The ones we consider here are stamped-copper-foils, flexible printed circuits (copper-on-Kapton), and multilayer printed circuit boards (PCBs). Practical prototypes are built for the RM10 core in order to compare performance.

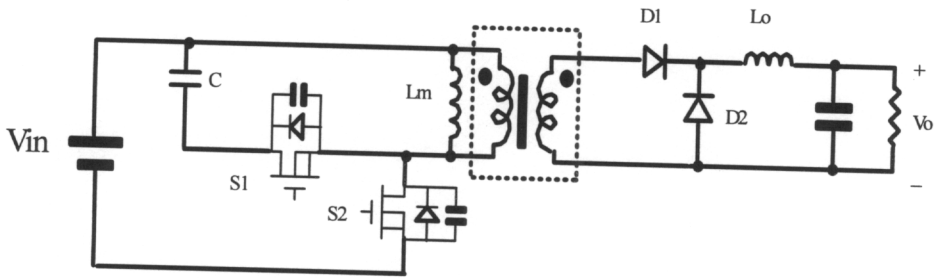

(a)

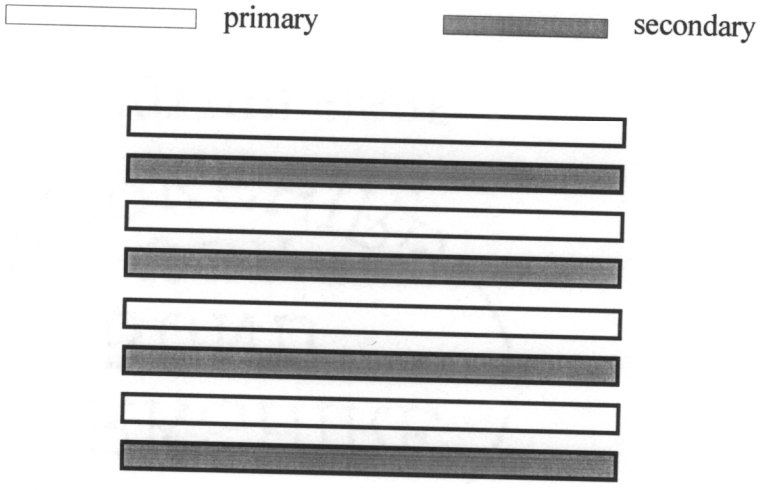

(b)

Fig. 5.1 (a) Circuit diagram of active clamp forward converter. (b) Transformer winding arrangement.

Table 5.1 Optimization results for a 300-W 5-V-output active clamp forward converter.

Transformer height H_t (cm)	0.92
Center post radius R_c (cm)	0.53
Window height H_w (cm)	0.33
Plate thickness H_p (cm)	0.29
Window width b_{win}	0.53
Primary copper thickness h_p (mil)	2.8
Secondary copper thickness h_s (mil)	2.8

5.1 Winding Techniques

5.1.1 Folded Winding Pattern

One of fabrication methods for the low-profile winding is to use the flexible circuit technology. In this approach, an etching process is used to create a number of thin, wide turns that are connected in series or in parallel. For this study, a single pattern was etched using 2.8-mil thick copper on a Kapton substrate. When the strip winding is folded, it creates the desired complete turns, as illustrated in Fig. 5.2(a). The secondaries are implemented using either semi-circular or fully-circular patterns, shown in Fig. 5.2(b). A transformer constructed with this technique has the advantage of the layer insulation being automatically provided by the substrate.

A transformer with folded winding design does not require external interconnections between turns, because the primary winding is a continuous copper strip. The secondaries, however, must be paralleled externally. The transformer turns ratio can be adjusted by changing the number of sections on the strip pattern. However, it is difficult to implement a large number of turns due to the build-up of the material and alignment problems. The leakage inductance will vary, depending on how well the turns are compressed together. In general, it is difficult to achieve consistent leakage inductance in every construction. In addition, the folds in the winding structure increase

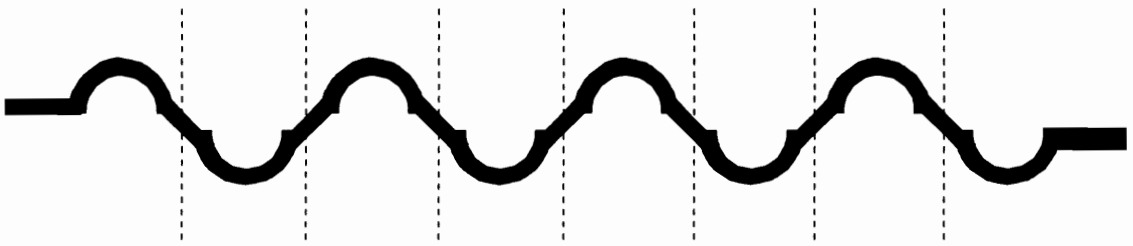

(a) Primary winding pattern

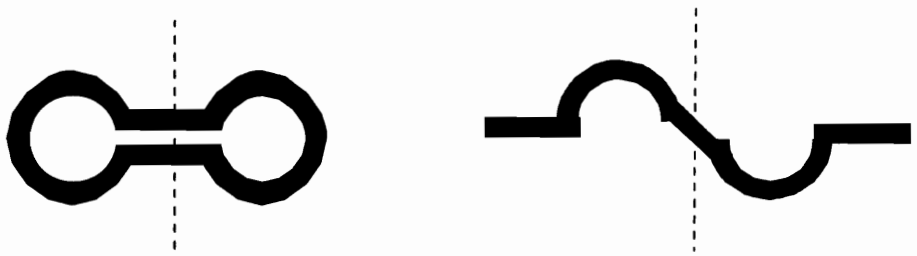

Fully circular winding pattern Semi-circular winding pattern

(b) Secondary winding patterns

Fig. 5.2 Winding patterns for a folded winding using copper foil or flexible printed circuit.

thermal resistance between turns, which may lead to local hot spots in the winding.

5.1.2 Multilayer PCBs

Figure 5.3 shows the winding layers of an eight-layer PCB using standard two-ounce copper (71 μm) in a fully interleaved primary-secondary winding structure. This winding structure results in a series-connected four-layer primary and a four-layer one-turn secondary. The terminations of the four one-turn primary layers are shifted with respect to each other and are connected in series by plated-through holes. The secondary terminals are implemented using two side-by-side vias, one for the secondary start and the other for the secondary finish. Figure 5.4 shows a second design -- Version 2 -- which uses the identical winding structure, but adds an interleaved secondary termination scheme: four interleaved pins are used, with two for the start of the secondary and two for the finish. Six small via holes are used to connect the interleaved termination pins to the appropriate start and finish portions of the secondary. This interleaved termination makes the current distribution in the secondary terminations more uniform.

The PCB winding technique produces a transformer that is consistent from sample to sample, and therefore the performance of such a device is likely to be more repeatable than that of any of the other structures studied here. In addition, the printed winding

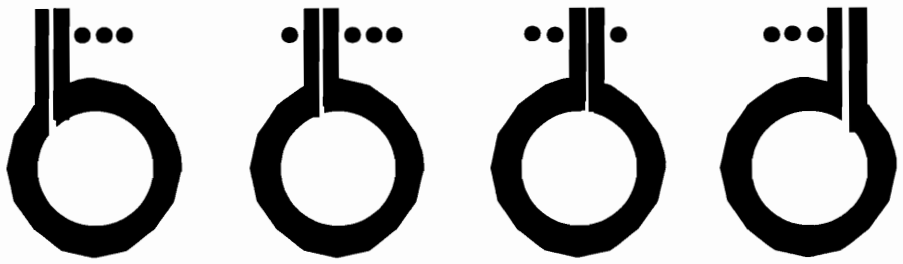

Primary Winding

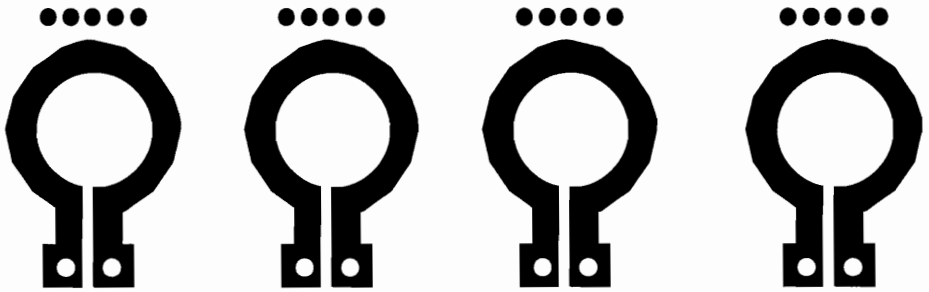

Secondary Winding

Fig. 5.3 Multilayer PCB winding pattern, version 1.

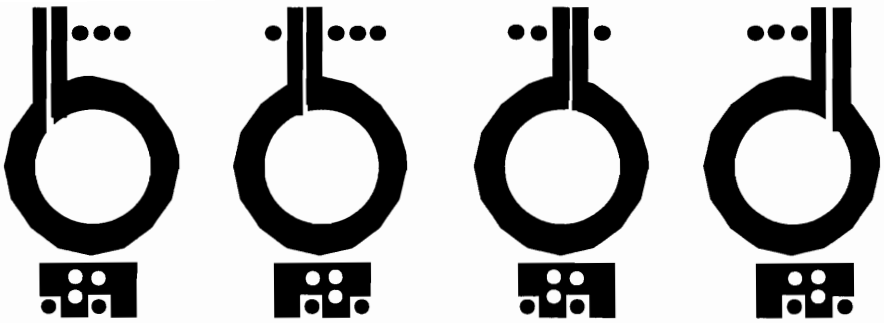

Primary Winding

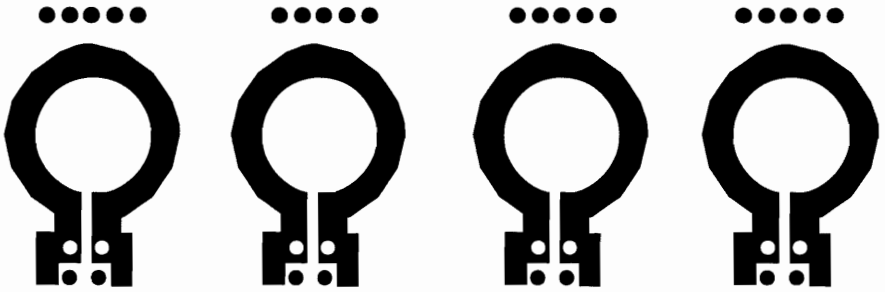

Secondary Winding

Fig. 5.4 Multilayer PCB winding pattern, version 2.

technique is more suitable for mass production. However, the cost of multilayer PCBs can be high, especially if non-standard copper thickness is desired. In a multilayer PCB, the insulator thickness is often greater than the copper thickness, and therefore it is difficult to achieve high window area utilization.

5.2 Termination Resistance

In order to compare the performance of the transformers, the dc-resistances of the windings were calculated and measured, including both the resistance of the annular ring that makes up each winding layer and the dc interconnection resistance. The short-circuit ac-resistances were measured using an HP4194A impedance analyzer. The ac-resistances of terminations and interconnecting vias were estimated by subtracting the FEA calculated ac-resistance of the ring portion of the winding from the measured total resistance of the winding. Table 4.9 shows the dc- and ac-resistance distribution for transformers with different winding techniques. It shows that, at DC, the interconnection resistances represent typically 25% to 33% of the total resistance. The ring resistance dominates the winding loss. At higher frequencies, however, the interconnection resistances contribute as much as 65-80% of the total resistance. In other words, at high frequencies, the termination resistance can make up approximately three-fourths of the

measured short-circuit resistance. It is therefore important to reduce the termination resistance as much as possible.

Figure 5.5(a) shows the current direction and the effective current carrying regions at high frequency in the two pins of the first PCB winding design shown in Fig. 5.3. The shaded areas of the termination pins indicate that only the inner surfaces of the two pins are utilized at high frequency because of the proximity effect induced in the pins. This results in a high termination resistance. If four pins are used side by side, as shown in Fig. 5.5(b), the proximity effects at high frequency still redistribute the current to only the inner surfaces of the two innermost pins. This means that the effective current carrying region is exactly the same as that of the two-pin case, and therefore the termination resistance cannot be reduced simply by putting more pins side by side. If the four pins are interleaved, as shown in Fig. 5.5(c), the high frequency currents are forced to flow on both surfaces of the center two pins and on the inner surfaces of the outer two pins. This means that the termination resistance is reduced significantly over that of the previous two cases. The short-circuit ac-resistance measurements of the transformers using these two different termination techniques show how the interleaved termination reduces the effective resistance by 27.5%.

The transformer was built from modified RM10-3F3 and 2-ounce copper multilayer PCB winding version 2. Figure 5.6 shows the assembled transformer. The transformer was tested in a 300-W, 40-60-V input, 5-V output active-clamped forward

converter. It worked properly at its full load and line range. The winding loss was measured by using HP 4129A Impedance Analyzer, and the temperature rise was measured by using 2166A 10-Channel Digital Thermometer. The experimental results show that the optimization program has enough accuracy to be used in the design of low-profile transformers.

5.3 Summary

Several ways to implement the low-profile transformer have been discussed. The termination loss of the low-profile transformer has been evaluated. The advantages and disadvantages of the printed-circuit-board (PCB), flex-circuit, and stamped-copper winding technologies are evaluated. The trade-offs between electrical and mechanical properties are emphasized. It is demonstrated that the secondary winding termination resistances for these transformers constitute a large percentage of the total ac-resistance of the transformers. It is also shown that the interleaving termination design can reduce the termination loss significantly.

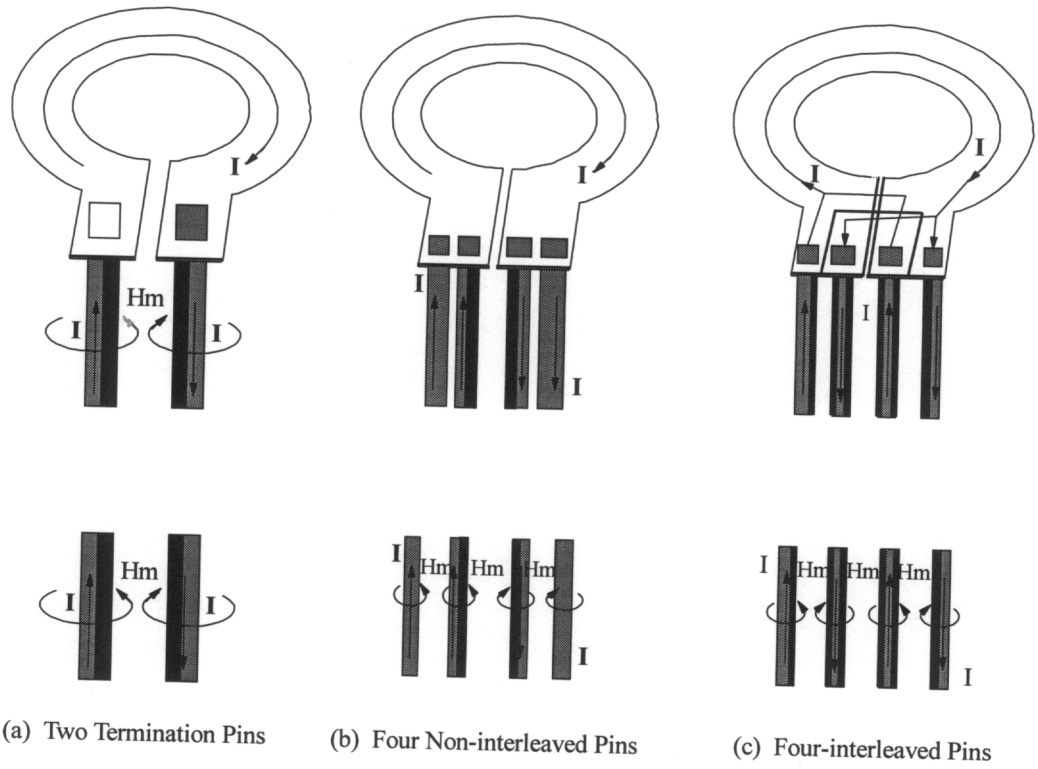

(a) Two Termination Pins (b) Four Non-interleaved Pins (c) Four-interleaved Pins

Fig. 5.5 The current direction and the effective current carrying regions at high frequency in (a) two termination pins, (b) four non-interleaved pins, and (c) four-interleaved pins.

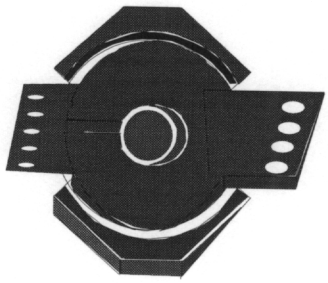

Fig. 5.6 Low-profile transformer with multilayer PCB winding and modified RM10 core.

Table 5.2 DC and AC Resistance Distribution

	DC Resistance (mΩ)		AC Resistance (mΩ)	
Winding Technique	Ring	Interconnection and Termination	Ring	Interconnection and Termination
PCB Version 1	29.5	8.5	88.6	60.5
Copper on Kapton	28.1	8.1	63.6	35.5
Stamped Foil	16.8	5.4	43.1	27.6

Chapter 6

Conclusions and Future Work

A 1-D winding loss model for low-profile winding loss calculation is derived, which takes the high-frequency skin effect and proximity effect into account. The model reveals that a low-profile transformer has a lower ac-resistance than that of an equivalent conventional transformer (where the "equivalent" means having the same window width and conductor thickness as the low-profile transformer) if the window width is small. However, when the window width increases to a certain value, the low-profile transformer has a higher ac-resistance than that of conventional transformers. The leakage inductance of a low-profile transformer is always lower than that of an equivalent conventional transformer.

The electrodynamic behavior of windings in high-frequency transformers has been studied in two-dimensions. The FEA is used to visualize high-frequency magnetic field and current distribution, and to quantify high-frequency power dissipation and energy storage by taking high-frequency skin effect, proximity effect, and edge effect into account. The regions of high leakage fields and strong current crowding are clearly displayed. The characteristics of winding arrangements (interleaved or sandwiched, balanced or unbalanced) with different wire types (solid wire, Litz wire, and printed wire) are accurately predicted. This analysis reveals the mechanism of optimizing the winding structure for minimal loss.

A new algorithm has been developed to design a low-profile transformer that has a maximum power density and meets a given set of specifications. The maximum achievable power density for a given power level and output voltage is computed based on only one fundamental constraint, i.e. temperature rise. Consequently, the maximum achievable power density and the required number of turns are determined along with the optimum operating frequency and core geometry. The algorithm is realized by using a nonlinear optimization technique and is coded into a program. It reveals the relations between the transformer power density and design parameters, the trade-offs between the winding loss and the core loss, and the trade-offs between footprint and profile.

In the optimization process, the 1-D winding loss calculation and the FEA method have been combined. The combination preduces more accurate design results than those

obtained by simply using the 1-D method. The proposed design procedures are implemented as MATLAB optimization program, which can

- design a low-profile transformer with maximum power density with **temperature constraint**;
- design a low-profile transformer with maximum power density with **limited height and temperature constraint**;
- design a low-profile transformer with maximum power density with **highest efficiency**;
- design a low-profile transformer with maximum power density with **limited height and highest efficiency**.

For the low-voltage high-current application, the secondary side termination design becomes critical. An interleaved termination design is proposed to lower the termination resistance.

The future work would involve

- developing a two-dimensional winding loss model for a low-profile transformer to overcome the limitations of a 1-D model.

- Combining the analytical method and the numerical technique. Since the purpose of any modeling efforts is to provide solutions for design software, the combination of analytical and numerical techniques, formulated for the purpose of solving high frequency power magnetics, seems to be the most promising approach. The whole problem is to be broken down into separate parts, with particular models applied to each. For example, the FEA is used to account for fringing fields in gapped core and their corresponding eddy current induced in nearby windings, and the analytical method is used to analyze loss in the windings that are far away from air gap.

- Developing a more accurate thermal model. A purely conductive thermal model is valid only when the low-profile transformer has a good thermal contact with a heat sink. For a gapped transformer or an inductor, the conductive thermal model does not predict accurately the temperature rise. When a magnetic component is involved in different kinds of heat transfer, it is very difficult to set up a good thermal model.

- Incorporating the new magnetic model and extending the capability of the optimization software. The software is developed for a low-profile transformer optimization. For a low-profile transformer with air gap or a low-profile inductor, the new winding loss model has to be set up to account for the fringing effect and

eddy current in a nearby winding. Incorporating of the new model into the optimization design tool can extend the capability of the software.

References

A. Finite Element Analysis and Winding Loss Calculation:

[A1] Goldberg, A. F., Kassakian, J. G., Schlecht, " Finite element analysis of copper loss in 1-10 MHz transformers," *IEEE PESC,* pp. 1105-1111, 1988.

[A2] Rudy Severns, "Additional losses in high frequency magnetics due to non ideal field distributions," *IEEE APEC*, pp.333-338, 1992.

[A3] W. M. Chen, P. D. Evans, W. J. B. Heffernan, "Inductor design concepts for high frequency applications," *Proc. EPE*, pp. I19-I24, 1991.

[A4] G. R. Skutt, and P. S. Venkatraman, "Analysis and measurement of high-frequency effect in high-frequency transformers", *IEEE APEC*, pp. 354-364. 1990.

[A5] R. K. Dhawan, P. Davis, and A. W. Lotfi, "High frequency loss evaluation in high frequency multi-winding power transformers," *IEEE APEC*, pp. 354-360, 1995.

[A6] A. Nysveen and M. Hernes, " Minimum loss design of a 100 kHz inductor with foil windings," *Proc. of EPE*, pp.106-111, 1993.

[A7] K. Gallyas, "Current density and power distribution in sheet windings," *Ph. D. Dissertation*, University of Toronto, Canada, 1975.

[A8] J. Simkin, "Eddy current modeling in three dimensions," *IEEE Trans. Magn., Vol.* MAG-22, No. 5, pp. 609-13, 1986.

[A9] J. Wesis and Z. J. Caendes, "A one-step finite element method for multiconductor skin effect problem," *IEEE Trans. Power Apparatus & Sys., Vol.* PAS-101, No. 10, pp. 3796- 803, 1982.

[A10] A. Konard, "The numerical solution of stead-state skin effect problems-An integrodifferential approach," *IEEE Trans. Magn. Vol.* MAG-17, No. 1, pp.1148-52, 1981.

[A11] O.W. Anderson, "Transformer leakage inductance flux program based on the finite element method," IEEE *Trans. Power Apparatus & Sys., Vol.* PAS-92, pp. 682-9, 1973.

[A12] P. L. Dowell, "Effects of Eddy Currents in Transformer Windings", Proceeding of *IEE*, Vol. 113, No. 8, Aug., 1966, pp. 1387-1394.

[A13] P. S. Venkatraman, "Winding eddy current losses in switch mode power transformer due to rectangular wave currents," *Proceeding of Powercon*, pp. 1-11, A-1, 1984.

[A14] B. Carsten, "High Frequency Conductor Losses in Switchmode Magnetics", *HFPC*, May, 1986, pp. 155-176.

[A15] M. P. Perry, "Multiple layer series connected winding design for minimum losses," *IEEE Transaction on Power Apparatus and System*, Vol. PAS-98, No. 1, Jan/Feb 1979.

[A16] J. P. Vandelac and P. Ziogas," A novel approach for minimizing high frequency transformer copper loss," *IEEE PESC*, pp. 355-367,1987.

[A17] John Rosa, "Calculation of flux leakage in multiwinding transformers," *IEEE PESC*, pp. 639-644.

[A18] Rudy Severns, "A simple , general method for calculating HF winding loss for arbitrary current waveforms," *HFPC*, pp. 149-159, Vol. 6, June, 1991.

[A19] M. P. Perry, "Mutiple layer parallel connected air-core inductor design," *IEEE Transaction on Power Apparatus and System*, Vol. PAS-98, No. 4, July/Aug. 1979.

[A20] Audry M. Urling, Van A. Niemela, Glenn R. Skutt and Thomas G. Wilson, "Characterizing high-frequency effect in transformer windings-a guide to several significant articles," *IEEE APEC*, pp. 373-385, 1989.

[A21] Van A. Niemela, Glenn R. Skutt, Audrey M. Urling, " Calculating the short circuit impedance of a multiwinding transformer from its geometry," *IEEE PESC*, pp. 607-618, 1990.

[A22] Steve Isakson, " Optimal transformer design for minimization of copper losses," Proc. *HFPC*, pp. 124-134, 1992.

[A23] J. A. Ferreira, "Appropriate modeling of conductive losses in the design of magnetic components," *IEEE PESC*, pp. 780-785, 1990.

[A24] Karl B. Mceachron, "Magnetic flux distribution in transformers," *Trans. AIEE*, pp. 247-262, 1922.

[A25] Hurley, William G.; Wilcox, David J, "Calculation of leakage inductance in transformer windings," *IEEE Trans. on Power Electronics*, Vol. 9, No. 1, pp. 121-126, Jan., 1994.

[A26] A. W. Lotfi, "The electrodynamics of high frequency magnetic in power electronics," *Ph. D. dissertation*, Virginia Polytechnic Institute and State University, 1993.

[A27] P. Silvester, "Modern Electromagnetic Fields," Prentice-Hall, Englewood Cliffs, NJ, Chap.7, 1968.

[A28] A. Konard, "Integrodifferential finite element formulation of two-dimensional steady-state skin effect problems," *IEEE Trans. Magn., Vol.* MAG-18, No. 1, pp. 284-92, 1982.

[A29] J. Weis and V. K. Grag, "steady state eddy current analysis in multilt-excite magnetic systems with arbitrary terminal conditions," *IEEE Trans. Magn., Vol.* 24, No. 6, pp. 2676-8, 1988.

[A30] Q. S. Huang, L. Krahenbuhl and A. Nicolas, " Numerical calculation of steady state skin effect problems in axisymmetry," *IEEE Trans. Magn., Vol.* 24, No. 1, pp. 201-3, 1988.

[A31] QW. G. Odendaal, J. A. Ferreira, and W. A. Cronje, " Combined numeric and analytical methods for foil winding design," *IEEE PESC,* pp. 843-849, 1994.

[A32] P. P. Biringer and K. Gallyas, " Analytical approximations for determining the current density and power loss distribution in multolayer sheet windings," IEEE Trans. IAS, Vol. IA-13, No. 4, pp. 315-320, 1977.

[A32] N. Dai and F.C. Lee: "Edge Effect Analysis in a High-frequency Transformer," *IEEE PESC Conf.,* 1994.

B. Transformer Optimization

[B1] K. D. T. Ngo, R. P. Alley, A. J. Yerman, R. J. Charles and M. H. Kuo, "Effect of height on power density in spiral-wound power-pot-core transformers," IEEE Trans. On Power Electronics, Vol. 7, No. 3, pp. 592-600, 1992.

[B2] Andrew F. Goldberg and Martin F. Schlecht, " The relationship between size and power dissipation in a 1-10 Mhz transformer," IEEE *Trans. on Power Electronics,* Vol. 7, No.1, Jan., 1992.

[B3] K. D. T. Ngo, R. P. Alley, A. J. Yerman, R. J. Charles and M. H. Kuo, "Evaluation of trade-offs in transformer design for very-low-voltage power supply with very high efficiency and power density," IEEE APEC, PP. 344-353, 1990.

[B4] Ngo, K. D. T.; Lai, R. S, "Effect of height on power density in high-frequency transformers," IEEE PESC, pp. 667-672,1991.

[B5] A. F. Goldberg, J. G. Kassakian, and M. F. Schlecht, " Issues related to 1-10 Mhz transformer design," IEEE *PESC*, pp.379-386, 1987.

[B6] T. Katane, H. Nohgi, and Y. Sakaki, "Optimum core dimensions of transformer for switching power supplies,' IEEE PESC, pp. 24-28, 1994.

[B7] Steef A. Mulder, "On the Design of Low-profile High Frequency Transformers," *HFPC*, Vol. 5, pp. 141-159, May 1990.

[B8] F. C. Lee, S. Rahman, and C. J. Wu, "A new apparach to the minium weight/loss design of switching power converters," Proc. of Powercon, A-2 pp.1-9, 1981.

[B9] C. J. Wu, and F. C. Lee, "Minimum weight EI core and pot core inductor and transformer designs," IEEE Trans. On Magnetics, Vol. Mag-16, No. 5, pp. 755-757, Sep., 1980.

[B10] N. Froehleke, B. Becker, P. Wallmeier, and H. Grotstollen, "Computer aided optimization of multi-winding transformers for SMPS considering hf-effects," Proceedings of IAS, pp. 1043-1048, 1994.

[B11] Jozef H. Hendriks, "Optimizing Transformers for power conversion," Proceeding of *PCI*, Sep., 1987.

[B12] Mladen Ivankovic, "Optimum SMPS transformer design," Proceeding of *PCI*, pp. 183-188, june, 1986.

[B13] Clifford H. Anderson and Colonel W. T. McLyman, "Computerized design and evaluation of transformer and inductors," Proceeding of Powercon 8, pp. B.1-B.7, 1981.

[B14] Pawel M. Gradzki, Milan M. Jovanovic, and Fred C. Lee, "Computer aided design for high-frequency power transformers," IEEE *APEC*, pp. 1-8, 1990.

[B15] N. R. Coonrod, "Transformer computer design aid for high frequency switching power supplies," IEEE *PESC*, pp. 257-266, 1984.

[B16] Wen-Jian Gu and Rui Liu, "A study of volume and weight vs. Frequency for high-frequency transformers," IEEE *PESC*, pp. 1123-1129, 1993.

[B17] B. Becker, H. Grotstollen, and L. Heinenmann, "Computer aided design and modeling of high frequency magnetic components," IEEE *PESC*, pp. 335-341, 1995.

[B18] A. Lotfi, D. Sable, and F. C. Lee, "Nonlinear design optimization of quasi-resonant converter," IEEE *PESC*, pp. 66-73, 1992.

[B19] A. Lotfi, Q. Chen, and F. C. Lee, " A nonlinear optimization tool for the Full-Bridge Zero-Voltage-Switched DC-DC converter," IEEE *PESC*, pp. 66-73, 1992.

[B20] M. Kazemzadeh, "Optimizing magnetics designs for thermal considerations," *Proceeding of the Power Electronics Show & Conference*, pp. 92-100, 1987.

[B21] Wm. T. McLyman, "Transformer and inductor design handbook," 2nd Endition, Marcel Dekker Inc., 1978.

[B22] J. A. Ferreia, W. G. Odendaal, and W. A. Cronje, "Scant modeling: a new method for optimizing functionality and form of transformers," IEEE IAS, pp. 1218-1224.

[B23] R. K. Dhawan, P. Davis, and R. Naik, "Applying expert systems and fuzzy logic for core selection for high frequency power transformer," IEEE APEC, pp. 342-347, 1995

C. Low-profile Transformer Implementation:

[C1] David A. Peterson, "Low-profile transformer,", U.S patent, No. 4347490, Aug., 1982.

[C2] D. Linde, and C. A. M. Boon, "Design of a high-frequency planar power transformer in multilayer technology", *Proc. EPE*, pp. 1501-1506, 1989.

[C3] N. Dai, A. W. Lofti, G. Skutt, W. Tabisz and F. C. Lee, "A comparison study of high-frequency, low-profile planar transformer technologies", *Proc. of IEEE App. Power Elec. Conf*, pp. 1994.

[C4] N. Dai and F. C. Lee: "Low-profile Transformer Winding Configurations," *First International Power Electronics and Motion Control Conf.(IPEMC)*, 1994.

[C5] B. A. Miwa, L.F. Casey, and M.F. Schlet, "Copper-based hybrid fabrication of a 50 W, 5MHz 40 V-5 V dc/dc converter," IEEE Proc. Applied Power Electronics, No. 2, pp. 256-264, 1989.

[C6] K. D. T. Ngo, R. P. Alley and A. J. Yerman, "Fabrication method for a winding assembly with a large number of planar layers," *Proc. of IEEE App. Power Elec. Conf.*, pp. 543-549, 1991.

[C7] Alex Estrov, " Power transformer design for 1 MHz resonant converter," *HFPC*, pp. 36-54, May, 1986.

[C8] Slobodan Cuk, Ljubisa Stevanovic and Enrico Santi, " Integrated Magnetics Design With Flat, Low Profile Core," *HFPC*, Vol. 5, May, 1990.

[C9] Pawel M. Gradzki and Fred C. Lee, "Design of High-Frequency Hybrid Power Transformer", *VPEC Seminar*, pp. 319-326, Blacksburg, VA, Sep., 1988.

[C10] P. G. Barnwell, and T. J. Jackson, "Low profile high frequency power supplies using thick film planar transformers," Proc. EPE, pp. 93-97, 1993.

[C11] W.A. Roshen, R. L. Steigerwald, R. Charles, W. Earls, G. Claydon and C. F. Saj, "High efficiency, high MHz magnetic components for a low profile converter," IEEE APEC, pp. 674-682, 1992.

[C12] Emilio Alpizar, Khai D. T. Ngo, J. K. Watson, " Development and Characterization of a Low-Profile Matrix Transformer," *HFPC*, pp. 174-183, May, 1990.

[C13] Arun Balakrishnan, William D. Palmer, William T. Joines and Thomes G. Wilson, "Inductance of planar rectangular-spiral strip conductors for low-profile inductors," IEEE PESC, pp. 1401-1408, 1992.

[C14] R. F. Soohoo, " Magnetic Thin Film Inductors for Integrated Circuit Applications," IEEE Trans. On Mag., Vol. Mag. 15, No. 6, pp.1803-1805, Nov., 1979.

[C15] Estrov, A. "Planar magnetics for power converters," IEEE *Trans. on Power Electronics, PE-31*, pp. 46-53, 1989.

[C16] Leo Johnson, Isaac Lagnado and Russell Hammond, "Design Considerations for Low Profile High Performance Inductors and Transformers," *HFPC*, Vol. 7, pp. 140-155, May 1992.

[C17] Michael A. Morrill, Vahe A. Caliskan and C. Q. Lee, "High-frequency planar power transformers," IEEE Trans. On Power Electronics, Vol. 7, No. 3, July, 1992.

[C18] Nishimura, Toshi Hiro; Eguchi, Tetsuji; Hirachi, Katsuya; Maejima, Yasushi; Kuwana, Kouji; Saito, Masao, "Large air gap flat transformer for a transcutaneous energy ," IEEE *PESC*, pp. 1323-1329, 1994.

[C19] Wassem A. Roshen, "Multi-turn z-foldable secondary winding for a low-profile, conductive film transformer," U. S. Patent, No. 5381124, General Electric Company, Oct., 1995.

[C20] U. S. Patent, "Z-foldable secondary winding for a low-profile, multi-pole transformer," General Electric Company, Jan., 1994.

[C21] Emil J. Raggi, Garland, Tex: "Multiple turn low profile magnetic component using sheet windings," U. S. Patent, No. 5179365, AT&T Corp., Dec., 1993.

[C22] L. R. Norgard, James A. Voll, "Low profile transformer," U. S. Patent, No. 348045, OECO Corporation, June, 1994.

[C23] M. P. Sayani, G. Skutt, and P. S. Venkatraman, "Electrical and thermal performance of PWB transformer," IEEE AOEC, pp. 533-542, 1991.

D. Transformer Integration with Circuit Board

[D1] Ionel Dan Jitaru, " High frequency DC-DC converter," *HFPC*, pp. 120-127, April, 1994.

[D2] J. Roudle, JL. Schanen, and R. Perret, "Interconnection modeling in power electronics structure," Submitted to IEEE Trans. Power Electronics.

[D3] A.E. Ruehli, "Inductance calculation in a complex integrated circuit enviroment," *IBM Journal of Researcg and Development*, Sept., 1972, pp. 470-481.

[D4] A. E. Ruehli, and P.A. Brennan, "Efficient capacitance calculations for three-dimensional multiconductor system," *IEEE Trans. Mocrowave Theory Tech.*, Vol. MTT-21, No. 2, pp. 76-82, Feb., 1973.

[D5] H. Heeb, and A. E. Ruejli, "Three-dimensional interconnec analysis using partial element equivalent circuit," *IEEE Trans. Circuit Systems*, Vol. 39, No. 11, pp. 974-982, Nov., 1992.

[D6] Leo. F. Casey, Andrew F. Goldberg, and Martin F. Schlet, "Issues regarding the capacitance of 1-10 Mhz transformers," *IEEE APEC*, pp. 352-359, 1988.

[D7] F. Blache, J. P. Keredec, and B. Cogitore, "Stray capacitances of two winding transformers: equivalent circuit, measurement, calculation and lowering," *IEEE IAS*, pp. 1211-1217, 1994.

[D8] B. Cogitore, J. P. Keredec, and F. Blache, "The two-winding transformer: an experimental method to obtain a wide frequency range equivalent circuit," *IEEE Trans. on Instrumentation and Measurement*, Vol. 43, No. 2, April, 1994.

[D9] A. Dauhajre and R.D. Middlebrook, " Modeling and estimation of leakage phenomena in magnetic circuits," *IEEE PESC*, pp. 213-226.

[D10] H. A. Owen, V. A. Niemela, and T. G. Wilson, " Cross-coupled-secondaries model for multiwinding transformers," *IEEE PESC*, pp. 1269-1276, 1992.

[D11] H. A. Owen, V. A. Niemela, and T. G. Wilson, " Enhanced cross-coupled-secondaries model for multiwinding transformers," *IEEE PESC*, pp. 1269-1276, 1992.

[D12] J. B. Klaassens, H. W. Klesser, M. P. N. Wesenbeek, "Interaction between a series-resonant converter and a transformer," EPE, pp. 2-460-2-473, 1991.

[D13] E. Laveuve, M. Bensoam, and J. P. Keradec, " Wound component parasitic elements: calculation, simulation and experimental validation in high frequency power supply," EPE, pp. 2-480-2-483, 1991.

[D14] G. W. Ludwig, S. El-Hamamsy, "Coupled inductance and reluctance models of magnetic components," IEEE Trans. on Power Electronics, Vol. 6, No. 2, April, 1991.

[D15] User's reference, "ANSOFT, 3D parameter extractor," Feb., 1993.

E. General:

[E1] J. Lammeraner, and M. Stafl, "Eddy current," CRC Press, Cleveland, OH, 1966.

[E2] R. L. Stoll, "The analysis of eddy current," Clarendon, Oxford, 1974.

[E3] H. B. Dwight, "Skin effect in tubular and flat conductors," Trans. AIEE, Vol. 37, pp. 1379-1403, 1918.

[E4] G. W. O. Howe, "The high frequency resistance of wires and coils," J. IEE, Vol. 58, pp. 152-161, 1920.

[E5] P. Silvester, "Modern electromagnetic field," Prentice-Hall, Englewood Cliffs, NJ, 1968.

[E6] E. C. Snelling, A. D. G., "Ferrites for inductors and transformers," ed. P. R. Laboratories. 1983, Surry, England: Redhill.

[E7] Chen D. Y., "Comparison of high frequency magnetic core loss under two different driving conditions: a sinusoidal voltage and a squarewave," IEEE PESC, pp. 237-241, 1978.

[E8] W. E. Babcock, " Asimplified method of determining high frequency characteristics of magnetic core material." Proc. Powercon, Vol. F3-1-17, 1983.

[E9] V. J. Thouttuvelil, T. G. Wilson, and H. A. Owen, "High-frequency measurement techniques for magnetic cores," IEEE PESC, pp. 412-425, 1985.

[E10] Goldberg, A. F., "High field properities of Nickel-Zinc Ferrites at 1- 10 Mhz," IEEE APEC, pp. 356-363, 1988.

[E11] P. M. Gradzki, and Fred C. Lee, "High-frequency core loss characterization based on impedance measurement," HFPC, 1991.

[E12] Steef A. Mulder, "Loss formulas for power ferrites and their use in transformer design," *Philips Components-Corporate Inovation Magnetics Eindhoven*, Netherlands, Feb., 1994.

[E13] Rudy Severns, "HF core loss for non-sinusoidal waveforms," Proc. HFPC, pp.140-148, 1991.

[E14] P. Han, G. Skutt, J. Zhang, anf Fred C. Lee, "Finite element method for ferrite core loss calculation," IEEE APEC, pp. 348-353, 1995.

[E15] J. Zhang, G. Skutt, and Fred C. Lee, "Some practical issues related to core loss measurement using impedance analyzer approach," IEEE APEC, pp. 547-553, 1995.

[E16] G. Skutt, and Fred C. Lee, "Use of visualization tools for examining flux distribution in magnetic structures," IEEE APEC, pp. 567-573, 1995.

[E17] M. D. Takach and P. O. Lauritzen, "Survey of magnetic core materials," IEEE APEC, pp. 560-566, 1995.

Appendix

```
%%%%%%%%%%%%%%%%%%%%%%%%%%%%%%%%%%%%%%%%%%%%%%%%%%%%%%%%%
%                 main program  "ecorecon.m "for  E-core            %
%    The purpose is to design a low-profile ttransformer with a maximum power density    %
%                                                                   %
%%%%%%%%%%%%%%%%%%%%%%%%%%%%%%%%%%%%%%%%%%%%%%%%%%%%%%%%%

%%%%%%%%%%%%%%%%%%%%%%%%%%%%%%%%%%%%%%%%%%%%%%%%%%%%%%%%%
%                     Define the global variable                    %
%%%%%%%%%%%%%%%%%%%%%%%%%%%%%%%%%%%%%%%%%%%%%%%%%%%%%%%%%

global vo po io vi D n dt Ploss
global Np Nsp Mp Ns Nss Ms Hi Crep Cr sigma mu Kwr NN
global Iorms Iirms f a2 a4 Bm a3
global Pc Pdd Pc1 Pc2 M Pdd1
global Rthf Rthd Rthc Rthbi Hbi Hcs Rtha Rthm
global Hp Acore A B Dc mpp mss Wc hs hp Wp Ww Hair lt
global Vc Ht Pcal Ploss Rpdc Rsdc Pp Ps Hw
global tr pter Trm Twind Tcore

%%%%%%%%%%%%%%%%%%%%%%%%%%%%%%%%%%%%%%%%%%%%%%%%%%%%%%%%%
%                           input the design parameters             %
%%%%%%%%%%%%%%%%%%%%%%%%%%%%%%%%%%%%%%%%%%%%%%%%%%%%%%%%%

vo = 6.6 ;     % output voltage (v)
po = 100 ;     % output power (W)
D  = 0.5 ;     % duty cycle
n  =  4  ;     % turns ratio
vi = 48  ;     % input voltage (v)

dt  = 40   ;   % temperature rise from the hot spot of transformer to heat sink
eff = 0.985 ;  % efficiency of transformer

%%%%%%%%%%%%%%%%%%%%%%%%%%%%%%%%%%%%%%%%%%%%%%%%%%%%%%%%%
%                input the winding arrangement information           %
%%%%%%%%%%%%%%%%%%%%%%%%%%%%%%%%%%%%%%%%%%%%%%%%%%%%%%%%%

Np  = 4 ;     %  number of primary turns
Nsp = 1;      %  number of turns per layer of primary winding
Mp  = 1;      %  number of layer parallel in primary winding
Ns  = 1 ;     %  secondary turns
Nss = 1 ;     %  number of turns per layer of secondary winding
Ms  = 4 ;     %  number of layers parallel in secondary winding
mpp = 1 ;     %  primary number of layers from its zero to its peak mmf
mss = 1 ;     %  secondary number of layer from its zero to its peak mmf

Hi  = 0.00508;        %  insulator thickness equal to 2 mil, (cm)
```

```
Crep = 0.1225e-1;   % distance between the trace equal to 15 mil, (cm)
Cr = 1.0e-1;        % distance between the edge of winding and core, (cm)
Hbi = 0.25 ;        % substrate thickness of circuit (cm)
Hcs = 5.08e-3 ;     % distance between the heat sink and substrate 2 mil (cm)
Kwr = 0.6    ;      % window area untilization at vertical direction

%%%%%%%%%%%%%%%%%%%%%%%%%%%%%%%%%%%%%%%%%%%%%%%%%%%%%%%%%%%%%%%%%%%%%%%%%%%%%%%%
%                                    input the characteristics of material                                    %
%%%%%%%%%%%%%%%%%%%%%%%%%%%%%%%%%%%%%%%%%%%%%%%%%%%%%%%%%%%%%%%%%%%%%%%%%%%%%%%%

sigma = 5.8e7  ;     % conductivity of material
mu = 1.257e-6 ;      % permeability of air
Rthd = 8 ;           % thermal resistivity of insulator (cm/W)
Rthc = 0.0026 ;      % thermal resistivity of copper (cm/W)
Rthf = 0.25 ;        % thermal resistivity of ferrite (cm/W)
Rthbi = 0.1 ;        % thermal resistivity of alumina   ceramics (cm/W)
Rthm = 1.34 ;        % thermal resistivity of thermal glue ( Cm/W)
Rtha = 38.76 ;       % thermal resistivity of air (cm/W)

%%%%%%%%%%%%%%%%%%%%%%%%%%%%%%%%%%%%%%%%%%%%%%%%%%%%%%%%%%%%%%%%%%%%%%%%%%%%%%%%
%                                    optimization convergence control variable                                %
%%%%%%%%%%%%%%%%%%%%%%%%%%%%%%%%%%%%%%%%%%%%%%%%%%%%%%%%%%%%%%%%%%%%%%%%%%%%%%%%

 options(1) = 0
 options(2) = 1e-8 ;
 options(3) = 1e-6  ;
 options(4) = 1e-7 ;
% options(13) = 1;
 options(14) = 1000 ;



%%%%%%%%%%%   Calculating the input and output RMS current    %%%%%%%%%%%%%%

io = po/vo ;          % output current (A)
Iorms = io*sqrt(D);   % output rms current
Iirms = Iorms/n;      % input rms current
Ploss = (1-eff)*po;   % power loss of the transformer

NN = Np*Mp/Nsp + Ns*Ms/Nss ; % calculating the total number layers


%%%%%%%%%%%%%   given  frequency range  %%%%%%%%%%%%%%%%%%
%
% f=0   ;
% for j = 1:5   ;
% f = f + 300000; % operating frequency

 f=500000;   %   input one particular frequency that interesting (Hz)
```

```
%%%%%%%%%%%%%%%%%%%%%%%%%%%%%%%%%%%%%%%%%%%%%%%%%%
%              core loss coefficients, which are extract from core loss data  catalog          %
%                                for Magnetic K-material                                       %
%                         Pc=a2*f^a3*B*^a4 W/cm^3, f in kHz, B in mT                           %
%%%%%%%%%%%%%%%%%%%%%%%%%%%%%%%%%%%%%%%%%%%%%%%%%%

a2=6.55e-5;
a3=1.565;
%a4=2.759 ;

%a2 = 8.98e-11 ;       % core loss coefficient at 300 kHz,
 a4 = 3.23    ;        % core loss coefficient

 % a2 = 2.9409e-10;
  a4 = 3.1434          % @ f=500 kHz

 % a2 = 3.6909e-9;
 % a4 = 3.0173         % @ f = 1 MHz

 % a2 = 8.5779e-8
 % a4 = 3.0173          % @ f = 2 MHz

 %%%%%%%%%%%%%%%%%%%%%%%%%%%%%%%%%%%%%%%%%%%%%%%%%%


   Htt(1) = 0.6            %  give the start point of transformer height, (cm)
   Vc =3.0                 %  Making a starting guess of transformer volume (cm^3)

   m1=1 ;                 % initial value of numbet of sections
   sd = 100/sqrt(3.14159*f*sigma*mu); % skin depth calculation
   error = 0.05 ;  % The accuracy of loss


%%%%%%%%%%%%%%%%%%      print input parameters        %%%%%%%%%%%%%%%%%%

   fid = fopen ('doub1.dat', 'w') ;
   fprintf(fid, ' E-core Transformer')
   fprintf(fid, ' power po  = %g\n', po)
   fprintf(fid, ' output voltage Vo  = %g\n', vo)
   fprintf(fid, ' output current io  = %g\n', io)
   fprintf(fid, ' RMS current at primary Iirms  = %g\n', Iirms)
   fprintf(fid, ' RMS current at secondary Iorms  = %g\n', Iorms)
   fprintf(fid, ' operating frequency f  = %g\n', f)
   fprintf(fid, ' input voltae  vi = %g\n', vi)
   fprintf(fid, ' insulator thickness Hi = %g\n', Hi)
   fprintf(fid, ' window utilization at vertical direction Kwr= %g\n', Kwr)
   fprintf(fid, ' efficient of transformer eff = %g\n', eff)
   fprintf(fid, ' turns ratio n = %g\n', n)
   fprintf(fid, ' number of turn parallel Mp = %g\n', Mp)
   fprintf(fid, 'The initial paramaters are\n ')
   fprintf(fid,'\n')
```

```
  fprintf(fid, 'Vc = %g\n',Vc);

%%%%%%%%%%%%%%%%%%%%%%%%%%%%%%%%%%%%%%%%%%%%%%%%%%%%
%                    starting the loop of transformer height                    %
%%%%%%%%%%%%%%%%%%%%%%%%%%%%%%%%%%%%%%%%%%%%%%%%%%%%

  for i = 1:20
    Htt(i+1) = Htt(i) + .1 ;
    Ht = Htt(i)
    Vci = 10000 ;    % any large value
    m = 0 ;
    tr2 = -1 ;         % used to memory the last step calculation error
    for M = m1:1     % number of sectins
       mm = 0 ;
       tr = -1 ;       % temperature rise error tr < -error and tr > error
       DVc = 0.4;   % give the initial volume step (cm^3)

%%%%%%%%%%%%%%%%%%%%%%%%%%%%%%%%%%%%%%%%%%%%%%%%%%%%
%                          Volume step adjustment                          %
%%%%%%%%%%%%%%%%%%%%%%%%%%%%%%%%%%%%%%%%%%%%%%%%%%%%

     while abs(tr) > error
        if tr2*tr >= 0
          if tr >= 1e6
            Vc = Vc + 0.5 ;
          end
          if tr > error
            Vc = Vc +1.3 * DVc ;
            elseif tr>= -1
            Vc = Vc -DVc/2 ;
            else
            Vc = Vc -1.6*DVc;
         end
        else
        if DVc >1e-5
           DVc = DVc/2 ;
         end
        if tr < -error
          Vc = Vc - DVc ;
        else
          Vc = Vc + DVc ;
        end
      end
        tr2 = tr ;

      hwi = Ht-0.4;             % initial value of window height
      hw = [hwi, 2.2, sd/2];  % [ window height, core width, primary thickness, center post width]
      hw = constr ('subdoub', hw,options); % invoke optimization

     if abs(tr) <= error, break, end
        if tr2 == 1e6 & tr < 0 & DVc <=1e-3
```

```
        break , end

          if Vc >= Vci &  Pcal > Ploss, break, end
      end    % end while loop

     if Vc < Vci
        Vci = Vc
        hw2=hw ;
     else
        break
     end

   end    % end of M-loop

  %  M = M - 1
     m1 = M
     Vc = Vci
     hw = hw2
     Pcal = subdoub(hw) ;
     Sf = Vc/Ht  ;   % The footprint of transformer
     sff = hw(2)*(B+2*Wc+pter);
     Vcc = sff*Ht
     A = hw(2);
     Hw = hw(1);

%%%%%%%%%%%%%%%%%%%%%%%%%%%%%%%%%%%%%%%%%%%%%%%%%%%
%                          output optimization results                          %
%%%%%%%%%%%%%%%%%%%%%%%%%%%%%%%%%%%%%%%%%%%%%%%%%%%

     fprintf(fid, ' i = %g\n',i)
     fprintf(fid, ' transformer volume Vc  = %g\n', Vc)
     fprintf(fid, ' transformer box volume Vcc  = %g\n', Vcc)
     fprintf(fid, ' transformer height Ht = %g\n', Ht)
     fprintf(fid, ' transformer footprint  = %g\n', Sf)
     fprintf(fid, ' center poster width Dc  = %g\n', Dc)
     fprintf(fid, ' window height Hw  = %g\n', hw(1))
     fprintf(fid, ' plate thickness Hp = %g\n', Hp)
     fprintf(fid, ' depth of core B  = %g\n', B)
     fprintf(fid, ' width of core A  = %g\n', hw(2))
     fprintf(fid, ' number of sections M  = %g\n', M)
     fprintf(fid, ' window width Wc = %g\n', Wc )
     fprintf(fid, ' primary thickness hp  = %g\n', hp)
     fprintf(fid, ' skin depth sd = %g\n', sd)
     fprintf(fid, ' secondary thickness hs  = %g\n', hs)
     fprintf(fid, ' primary winding width Wp = %g\n', Wp)
     fprintf(fid, ' secondary winding width Ww  = %g\n', Ww)
     fprintf(fid, ' primary DC loss Pp  = %g\n', Pp)
     fprintf(fid, ' secondary DC loss Ps  = %g\n', Ps)
     fprintf(fid, ' primary DC resistance Rpdc  = %g\n', Rpdc)
     fprintf(fid, ' secondary DC loss Rsdc  = %g\n', Rsdc)
     fprintf(fid, ' total ac loss Pdd  = %g\n', Pdd)
```

```
      fprintf(fid, ' winding ac loss Pdd1  = %g\n', Pdd1)
      fprintf(fid, ' mean length per turn lt  = %g\n', lt)
      fprintf(fid, ' center post loss Pc1  = %g\n', Pc1)
      fprintf(fid, ' top or bottom plate loss Pc2 = %g\n', Pc2)
      fprintf(fid, ' total loss Pcal  = %g\n', Pcal)
      fprintf(fid, ' temperature rise Trm  = %g\n', Trm )
      fprintf(fid, ' flux density Bm  = %g\n', Bm )
      fprintf(fid, ' temperature rise Twind  = %g\n', Twind )
      fprintf(fid, ' temperature rise Tcore  = %g\n', Tcore )


        He(i) = Ht  ;  %  for one ferq.
        Vm(i) = Vc  ;  %  for one freq.
        Pddi(i) = Pdd ;
        Pci(i) = Pc  ;
%         He(i,j)=Ht  ;  %  for a range of freqs
%         Vmi(i,j)=Vc  ;  %   for a range of freqs.

 end

% end

figure (1)
grid on
plot (He(1,:), Vm(1,:), He(1,:), Vm(1,:),'b+' )  ;  % for plot of a curve
%  plot (He(1,:), Vmi(1,:),'b+', He(2, :), Vmi(2,:), 'y-');  %  for plot a family curve of Vc~Ht
figure (2)
plot (He(1,:), Pddi(1,:), He(1,:), Pddi(1,:),'b+' )  ;  % for plot of a curve
title ( 'transformer volume versus height  DT = 40 degree')
xlabel ('transformer height [cm]')
ylabel ('transformer volume [cm^3]' )
```

```
%%%%%%%%%%%%%%%%%%%%%%%%%%%%%%%%%%%%%%%%%%%%%%%%%%%%%%%%%%%%%%%%%%%%%%%%%%%%
%                              Subprogram of "ecorecon.m"                                         %
% %%%%%%%%%%%%%%%%%%%%%%%%%%%%%%%%%%%%%%%%%%%%%%%%%%%%%%%%%%%%%%%%%%%%%%%%%%%

 function [Pcal,g]  = subdoub(hw)

global vo po io vi D n dt Ploss
global Np Nsp Mp Ns Nss Ms Hi Crep Cr sigma mu Kwr NN
global Iorms Iirms f a2 a4 Bm a3
global Pc Pdd Pc1 Pc2 M Pdd1
global Rthf Rthd Rthc Rthbi Hbi Hcs Rtha Rthm
global Hp Acore A B Dc mpp mss Wc hs hp Wp Ww Hair lt
global Vc Ht Pcal Ploss Rpdc Rsdc Pp Ps Hw
global tr pter Tcore Twind Trm
% M = 1 ;     % number of sections

   % calculating transformer geometry

       Hw= hw(1);
       A = hw(2);                              % core width
       hp = hw(3);                             % primary thickness
       sf = Vc/Ht ;                            % footprint of core
       Hp = (Ht - Hw)/2;                       % plate thickness
       Dc = 2*Hp        ;                      % width of center post
       Wc = (A-Dc-2*Hp)/2  ;                   % window width
       B = Vc/Ht/A-2*Wc;                       % depth of core

       NNp = Np*Mp/Nsp ;
       NNs = Ns*Ms/Nss ;
       NN = NNp + NNs  ;                       % total number of layer
       td = Hi*(M*NN+1);                       % total thickness of insulation layers


    % secondary winding
       Hc =(Hw-td)*Kwr ;
       Hair = Hw - td - Hc ;
       hs =(Hc/M-NNp*hp)/NNs ;                 % secondary winding thickness

       Ww = (Wc-2*Cr-(Nss-1)*Crep)/Nss ;       % width of secondary winding
       lws = (B+Dc+2*Cr)*2+2*pi*Wc/2 ;         % mean length of secondary

    % primary winding
       Wp = (Wc-2*Cr-(Nsp-1)*Crep)/Nsp ;       % primary winding width

   % Calculating the loss

   %  winding resistance

       Rp1dc = lws/(sigma*1e-2*hp*Wp);
       Rpdc  = Np*Nsp*Rp1dc/Mp/M ;              % primary dc resistance
       Rsdc  = Ns*lws/(sigma*1e-2*hs*Ww)/Ms/M ;  % secondary dc resistance
```

```
% DC winding loss
      Pp = Iirms^2 * Rpdc ;                    % primary loss
      Ps = Iorms^2 * Rsdc ;                    % secondary loss

   %  ac resistance factor

      etas = Nss*Ww/Wc;
      etap = Nsp*Wp/Wc ;
      sd = 100/sqrt(3.14159*f*sigma*mu);       % skin depth (cm)
      xp = hp * sqrt(etap)/sd;                 % conductor thickness over skin depth
      xs = hs * sqrt(etas)/sd;

for k = 1 : NNs
    for i = 1 : mss
     j = mpp*(k-1) + mss*(k-1) + i ;
     N(j) = Nss ;
     I(j) = -Nss*Iorms/(M*Ms*Nss) ;
     eta(j) = etas ;
     hcu(j) = hs  ;
     x(j) = xs;
  end

  for i = 1 : mpp
     j = (mpp+mss)*(k-1)+mss + i  ;
     N(j) = Nsp ;
     I(j) = Nsp*Iirms/(M*Mp*Nsp) ;
     eta (j) = etap ;
     hcu(j) = hp ;
     x(j) = xp ;
  end
 end

lt = lws;
Hz(1) = 0 ;
for k = 1 : NN
  Hz(k+1)=Hz(k) +100* (N(k) * I(k))/Wc  ;
  if abs(Hz(k+1)) <= abs(Hz(k))
    alfa(k) = Hz(k+1)/Hz(k) ;
    Hzm(k) = abs(Hz(k)) ;
   else
    alfa (k) = Hz(k)/Hz(k+1) ;
    Hzm(k) = abs(Hz(k+1)) ;
  end

    G1(k) = x(k)*(sinh(2*x(k))+sin(2*x(k)))/(cosh(2*x(k))-cos(2*x(k)));
    G2(k) = x(k)*(sinh(x(k))*cos(x(k))+cosh(x(k))*sin(x(k)))/(cosh(2*x(k))-cos(2*x(k)))  ;
    G3(k) = (sinh(2*x(k))-sin(2*x(k)))/(x(k)*(cosh(2*x(k))-cos(2*x(k)))) ;
    G4(k) = (sinh(x(k))*cos(x(k))-cosh(x(k))*sin(x(k)))/(x(k)*(cosh(2*x(k))-cos(2*x(k))));

    if k == 1
```

```
    Plk(k) = M*1e-6*Wc*lt*mu*hcu(k)*Hzm(k)^2/4*((1+alfa(k)^2)*G3(k)-4*alfa(k)*G4(k)) ;
    Pd(k) = M*0.01* Wc*lt*Hzm(k)^2*((1+alfa(k)^2)*G1(k)-4*alfa(k)*G2(k))/(eta(k)*sigma*hcu(k)) ;
    else
    Pd(k) = Pd(k-1) + M*0.01*Wc*lt*Hzm(k)^2*((1+alfa(k)^2)*G1(k)-
4*alfa(k)*G2(k))/(eta(k)*sigma*hcu(k)) ;
   Plk(k) = Plk(k-1) + M*1e-6*Wc*lt*mu*hcu(k)*Hzm(k)^2/4*((1+alfa(k)^2)*G3(k)-4*alfa(k)*G4(k))
+1e-6*Wc*lt*Hi*mu/2*(Hz(k+1))^2 ;
    end
end
Pdd1 = Pd(NN) ;

pter = 0.4 ; %   termination length
ster = 0.4 ;

rpt = 100*2*Np/Nsp*pter/(sigma*Nsp*Wp*hp*M*Mp) ;
rst = 2*100*2*Ns*ster/(sigma*Nss*Ww*hs*M*Ms) ;
Ppt = Iirms^2*rpt ;
Pst = Iorms^2*rst ;
Pdd = Pd(NN) + Ppt + Pst ;

    % core loss

      Acore = B*Dc/2;                          % center post area(cm^2)
      Bm =abs(vi*D/(f*Acore*Np*1e-4 )) ;       % flux density (T)
      Pcd = a2*(f/1000)^a3*(Bm/2*10)^a4 ;      % core loss density(W/cm^3)
      Pc1 = Pcd*Acore*Ht;                      % core loss at center post
      Bmp = Bm*Acore/(2*Hp*B) ;
      Pcd2 = a2*(f/1000)^a3*(Bm/2*10)^a4 ;    % core loss at plate
      Pc2 = Pcd2*Hp*Wc*B;
      Pc3 = Pcd2*Hp*Ht*B ;
      Pc = 4*Pc2+Pc1+2*Pc3 ;                  % total core loss
  %     Pc=2*(2*Pc2+Pc1);
      % Objective function
      Pca = Pdd+Pc  ;                         % total loss


%%%%%%%%%%%%%%%%%%%%%%%%%%%%%%%%%%%%%%%%%%%%%%%%%%%%%%%%%%%%%%%%%%%
%                        Temperature rise calculation                        %
%%%%%%%%%%%%%%%%%%%%%%%%%%%%%%%%%%%%%%%%%%%%%%%%%%%%%%%%%%%%%%%%%%%

  Dbi = (Pc+Pdd)*Hcs/(A*B*0.01)*Rthm  ;
  % temperature rise of alumina substrate

%  Dtb = (Pc+Pdd)*Hp/(2*hw(2)*B*0.01)*Rthf  ;
  % temperature rise of bottom plate

  Dtc =Pc1*Ht/(2*Acore*0.01)*Rthf + Pc2*Ht/(Acore*0.01)*Rthf;
  % temperature rise of center post

  Dtt =Pc2/2*Wc/2/(Hp*B)*Rthf ; % temp. rise of top plate
```

```
  Tcore  = Dbi+ Dtc + Dtt ;  % temp. rise of core

  td = Hi*(NN+1);  % total thickness of insulation layers

  Twind = Dbi +
100*(Pc2/2+Pdd/2)*Hp*Rthf/(Wc*B)+100*Pdd/2*(Rthd*td+Rthc*Hc+Rtha*Hair/2)/(2*Wc*B) ;
% temperature rise from hot spot to heatsink
      Trm = Twind ;
  if Tcore > Twind
      Trm = Tcore ;
  end
%       tr = Trm - dt ;


         Pcal = Pca ;
         tr = Pcal - Ploss  ;

%%%%%%%%%%%%%%%%%%%%%%%%%%%  Design Constraints %%%%%%%%%%%%%%%%%%%%
    g(1)=-Hp+0.001;
    g(2)=0.2-Hp ;
    g(3)=-hs+0.00001 ;
    g(4)=-Wp +0.001;
    g(5)=-Ww +0.001;
    g(6)=-B +0.00001;
    g(7)=-Bm +0.00001 ;
    g(8)= -0.3+Bm;
    g(9)=-Hc+0.001;
    g(10)=-hw(1)+0.15 ;
    g(11)=-hw(2)+1e-4 ;
    g(12)=-Wc+0.001;
    g(13)=-hw(3)+1e-4;
    g(14)=Bmp-0.3 ;
    g(15) =Trm-40;
```

Vita

The author was born in Zhejiang, China. She received the B.S. and M.S. degrees in Electrical Engineering from Zhejiang University, in 1985 and 1988, respectively. She was then employed as an instructor in the electrical engineering department at the same university from 1988 to 1991. In 1991, she joined Virginia Power Electronics Center (VPEC) of Virginia Polytechnic Institute and State University as a research assistant, engaged in research in the areas of high-density low-profile dc/dc power converters, computer-aided optimization of low-profile transformers, and the electromagnetic behavior of high-frequency power magnetic devices.